The Dynamic Interplay between Submesoscales and Boundary Layer Turbulence

by
Abigail Bodner
Sc. M., Applied Mathematics, Brown University, 2020
M. Sc., Geophysics, Atmospheric and Planetary Sciences, Tel Aviv University, 2019
B. A., Mathematics & Geophysics, Atmospheric and Planetary Sciences, Tel Aviv University, 2014

A dissertation submitted in partial fulfillment of the
requirements for the Degree of Doctor of Philosophy in
the Department of Earth, Environmental and Planetary Sciences
at Brown University

Providence, Rhode Island
October 2021

This dissertation by Abigail Bodner is accepted in its present form
by the Department of Earth, Environmental and Planetary Sciences
as satisfying the dissertation requirement for the degree of Doctor of Philosophy.

Date ______________ ______________________________
Baylor Fox-Kemper, Advisor

Recommended to the Graduate Council

Date ______________ ______________________________
Christian Huber, Reader

Date ______________ ______________________________
Timothy Herbert, Reader

Date ______________ ______________________________
John Bradley Marston, Reader
(Department of Physics)

Date ______________ ______________________________
Martin Maxey, Reader
(Division of Applied Mathematics)

Date ______________ ______________________________
Stephen Griffies, Reader
(Princeton/GFDL)

Approved by the Graduate Council

Date ______________ ______________________________
Andrew G. Campbell
Dean of the Graduate School

ABIGAIL S BODNER

Department of Earth, Environmental and Planetary Sciences, Brown University
HOMEPAGE: abodner.github.io

EDUCATION

PhD *Expected October 2021*
Earth, Environmental and Planetary Sciences
Brown University
Advisor: Dr. Baylor Fox-Kemper

ScM *2020*
Applied Mathematics
Brown University

MSc (magna cum laude) *2019*
Geophysics, Atmospheric and Planetary Sciences
Tel Aviv University
Advisor: Dr. Nili Harnik

BSc (Double Major) *2014*
- Geophysics, Atmospheric and Planetary Sciences
- Mathematics
Tel Aviv University

HONORS AND AWARDS

Junior Fellow in the Simons Society of Fellows	*AY 2021-2024*
Student Oral Presentation Award at the Atmospheric and Oceanic Fluid Dynamics Meeting of the American Meteorological Society	*June 2019*
Associate of Sigma Xi Scientific Research Honor Society	*2019*
Gulf of Mexico Research Initiative Scholar	*2018*
Departmental First Year Fellowship, Brown University	*AY 2015-2016*
Rana Samuels Ofran MSc Student Excellence Award	*AY 2014-2015*

PUBLICATIONS

Bodner, A. S., Fox-Kemper, B., Van Roekel, L. P., McWilliams, J. C. & Sullivan, P. P. (2019). A perturbation approach to understanding the effects of turbulence on frontogenesis. *Journal of Fluid Mechanics*, 883.

Bodner, A. S. & Fox-Kemper, B. (2020). A Breakdown in Potential Vorticity Estimation Delineates the Submesoscale-to-Turbulence Boundary in Large Eddy Simulations. *Journal of Advances in Modeling Earth Systems*, e2020MS002049.

Bodner, A. S., Fox-Kemper, B., Johnson, L., Van Roekel, L. P., McWilliams, J. C. & Sullivan, P. P. ”Modifying the Mixed Layer Eddies Parameterization to Include Frontogensis and Frontal Arrest by Boundary Layer Turbulence. *In Preparation.*

Bodner, A. S., Harnik, N. & Lachmy, O. Atmospheric Flow Regimes and Vacillation Cycles in the Presence of Topography. *In Preparation.*

INVITED TALKS

Bodner, A. S.: “On the interaction between submesoscales and turbulence: from theory to implementation in global climate models”, Physical Oceanography Dissertations Symposium (PODS) XI, Lihue, Kaua‘i, October 2021 (Scheduled).

Bodner, A. S.: “Stir and mix: studying upper ocean dynamics from theory to application”, Department of Earth and Planetary Sciences, Weizmann Institute of Science, May 2021.

Bodner, A. S.: “Stir and mix: studying upper ocean dynamics from theory to application”, Department of Solar Energy and Environmental Physics (YDSEEP), Ben Gurion University of the Negev, April 2021.

Bodner, A. S.: “Stir and mix: studying upper ocean dynamics from theory to application”, School of Earth Sciences, Tel Aviv University, March 2021.

Bodner, A. S.: “On the interaction between submesoscales and turbulence: from theory to application”, Department of Applied Mathematics and Theoretical Physics Seminar, University of Cambridge February 2021.

Bodner, A. S.: “Stir and mix: studying upper ocean dynamics from theory to application”, Climate, Atmosphere and Oceanography Seminar, The Hebrew University of Jerusalem, January 2021.

Bodner, A. S.: “On the interaction between submesoscales and turbulence: from theory to implementation in global climate models”, Physical Oceanography Seminar, Woods Hole Oceanographic Institution, June 2020.

Bodner, A. S.: “On the interaction between submesoscales and turbulence: from theory to implementation in global climate models”, The Center for Atmosphere Ocean Science, Courant Institute of Mathematical Sciences, New York University, October 2019.

Bodner, A. S.: “Frontal evolution in the presence of submesoscale instabilities and turbulence”, Atmosphere, Ocean, and Climate Dynamics Seminar, Yale University, April 2019.

SELECTED PRESENTATIONS

Bodner, A. S., Fox-Kemper, B., Johnson, L., Van Roekel, L. P., McWilliams, J. C. & Sullivan, P. P.: ”Modifying the Mixed Layer Eddies Parameterization to Include Frontal Width Determined by Boundary Layer Turbulence. Ocean Model Working Group Winter Meeting, February 2021. *Oral.*

Bodner, A. S., Fox-Kemper, B., Van Roekel, L. P., McWilliams, J. C. & Sullivan, P. P.: “Frontal Formation in the Presence of Submesoscale Instabilities and Turbulence”, Atmospheric and Oceanic Fluid Dynamics Meeting, AMS, Portland, ME, June 2019. *Oral.*

Bodner, A. S. & Fox-Kemper, B.: “Hidden Dangers in Potential Vorticity”, Sources and Sinks of Ocean Mesoscale Eddy Energy Workshop (US CLIVAR), Tallahassee, FL, March 2019. *Oral.*

Bodner, A. S., Fox-Kemper, B., Van Roekel, L. P., McWilliams, J. C. & Sullivan, P. P.: “A Novel Approach to Understanding the Effects of Turbulence and Instabilities on Frontogenesis”, Symposium on Geophysical Fluid Dynamics, Sde Boker, Israel, January 2019. *Oral.*

Bodner, A. S., Fox-Kemper, B., Van Roekel, L. P., McWilliams, J. C. & Sullivan, P. P.: “A Novel Approach to Understanding the Effects of Turbulence and Instabilities on Frontogenesis”, CARTHE All Hands Meeting ,Miami, FL, November 2018. *Oral.*

Bodner, A. S., Fox-Kemper, B., Van Roekel, L. P., McWilliams, J. C. & Sullivan, P. P.: “A Perturbation Method to Understanding the Effects of Turbulence and Instabilities on Frontogenesis”, Ocean Sciences Meeting, TOS/ASLO/AGU, Portland, OR, February 2018. *Oral.*

Bodner, A. S., Fox-Kemper, B., Van Roekel, L. P., McWilliams, J. C. & Sullivan, P. P.: “Arrest of Frontogenesis by Submesoscales and Turbulence”, Ocean Sciences Meeting, TOS/ASLO/AGU, New Orleans, LA, February 2016. *Poster.*

Bodner, A. S., Harnik, N. & Lachmy, O.: “Global Circulation Regimes in the Presence of Stationary Planetary Wave Forcing”, Geophysical Fluid Dynamics Seminar, Weizmann Institute, Israel, July 2015. *Oral.*

Bodner, A. S., Harnik, N. & Lachmy, O.: “Global Circulation Regimes in the Presence of Stationary Planetary Wave Forcing”, 20th conference on Atmospheric and Oceanic Fluid Dynamics, Minneapolis, MN, June 2015. *Poster.*

Bodner, A. S., Harnik, N. & Lachmy, O.: “Effects of Stationary Forcing on Global Circulation Regimes”, Symposium on Geophysical Fluid Dynamics, Sde Boker, Israel, January 2015. *Poster.*

ADDITIONAL RESEARCH EXPERIENCE AND TRAINING

Community Earth System Model (CESM) Tutorial *Summer 2019*
Run by the National Center for Atmospheric Research (NCAR) in Boulder, CO.

Kavli Institute for Theoretical Physics Graduate Fellow *Spring 2018*
Program for Planetary Boundary Layers in Atmospheres, Oceans, and Ice on Earth and Moons (University of California Santa Barbara).

Fundamental Aspects of Turbulent Flows in Climate Dynamics *Summer 2017*
Summer school program run by Ecole de Physique des Houches (Les Houches, France).

Research Assistant of Dr. Nili Harnik *AY 2013-2014*
Detecting wave disturbances in the stratosphere influenced by the Circumglobal Teleconnection Pattern (Tel Aviv University).

Senior Year Project in Geophysical Fluid Dynamics *Spring 2014*
Under the guidance of Dr. Eyal Heifetz, worked on a revised solution for a Non-Boussinesq stratified shear flow (Tel Aviv University).

TEACHING EXPERIENCE

Studying the Ocean from the Classroom to the Bay *Summer 2018 & 2019*
Course designer and co-instructor in Summer@Brown pre-college program (Brown University).

Principles in Planetary Climate *Fall 2018*
Teaching assistant under Professor Jung-Eun Lee (Brown University).
Guest lecture: ”Large Scale Dynamics in the Ocean and Atmosphere”.

Teaching Consultant Program, Brown University Sheridan Center. *Fall 2017*

Climate Change: Fact or Fiction? *Summer 2017*
Course designer and instructor in Summer@Brown middle school program (Brown University).

Reflective Teaching Program, Brown University Sheridan Center. *Fall 2016*

Continuum Mechanics - Fluids *Spring 2015*
Teaching assistant under Professor Eyal Heifetz (Tel Aviv University).

Climate Theory *Spring 2015*
Teaching assistant under Professor Nili Harnik (Tel Aviv University).

Laboratory Experiments in Atmospheric Sciences *Fall 2014*
Teaching assistant under Professor Nili Harnik (Tel Aviv University).

Earth Sciences Teacher *2012-2013*
High school senior year research project (Shay Agnon High School, Israel).

Mathematics Teacher *2009-2014*
Middle school gifted children program (Bar-Ilan University).
High school and pre-college students (Raz Etgarim Educational Center, Israel).
At-risk youth (Haklai Boarding school, Israel).

SERVICE

Expert Reviewer for the Intergovernmental Panel on Climate Change (IPCC) Sixth Assessment Report *2019*

Expert Reviewer for the Special Report on the Ocean and Cryosphere in a Changing Climate (SROCC) *2018*

Reviewer for Journal of Physical Oceanography *2017-Present*

Graduate School Community Fellow *2018-2019*

First Year Graduate Student Mentor *2018-2019*

International Student Representative and Event Organizer *2016-2018*

Leadership Alliance - Graduate Student Panel *2018*

Volunteer at the Division of Fluid Dynamics Meeting (APS DFD) *November 2015*

PROFESSIONAL AFFILIATIONS

Affiliate Graduate Student in the Institute at Brown for Environment & Society (IBES)

Consortium for Advanced Research on Transport of Hydrocarbon in the Environment (CARTHE)

Graduate Fellow of the Rhode Island Consortium for Coastal Ecology Assessment Innovation & Modeling (C-AIM).

American Geophysical Union; American Meteorological Society; American Physical Society

SOFTWARE LANGUAGES

Matlab, Python, Fortran, C, Latex.

Acknowledgements

It turns out it also takes a village to finish a PhD. There are many people who have been instrumental in my life during this time. Without them, this experience would have been much more difficult, if not impossible. I am especially thankful to have such supportive family, friends and peers, both near and far, that were always rooting for me to succeed.

To my parents, grandparents, and in-laws, thank you for encouraging me to love science and nature, and for teaching me how important it is to feel empowered and accomplished in life. A special thanks also to my family in Israel for all coming together to help ensure my children had loving, safe and reliable childcare during this year of uncertainty.

To my friends who also happened to be my lab mates, thank you for all the laughter and tears we shared over the years. Thank you for talking science with me, helping with conference prep and frustrating code. A special thanks goes to Jenna Pearson, Brodie Pearson, Sydney Clark, Qing Li, Leah Johnson, Aakash Sane and Chris Horvat. I am looking forward to many more years of collaboration and friendship.

To my thesis committee: Chris Huber, Tim Herbert, Brad Marston, Martin Maxey and Steve Griffies, thank you for all your support, advice, and especially for helping me maneuver a PhD program with two maternity leaves and an additional masters degree.

To my advisor, Baylor Fox-Kemper – what an honor it is to work with someone so brilliant and inspiring but also so empathetic and down to earth. Thank you for having faith in me and my science and for teaching me how to turn a bunch of equations into a story. Your genuine support in every meeting, course, program or conference, are what made this experience so incredible. You are a role model of what an advisor should be. I hope to be able to pass this forward to students of my own one day.

Most importantly to Bar, my husband, best friend and partner in life. You are my everything, and I could not have done any of this without you. The true list is probably longer than this dissertation so I will keep it short. Thank you for always being present for me and our kids. You have always been so accepting and supportive of any travel adventure, stressful deadline and everything in between. I am so grateful for everything.

Finally, to my children, Micah and Amelia, thank you for your love and smiles that always helped remind me what really matters. All my rainbow-colored figures are dedicated to you both.

Contents

List of Tables **xii**

List of Figures **xiii**

1 Introduction **1**

1.1 Motivation 1

1.2 Phenomenology 3

1.2.1 The ocean surface layer 3

1.2.2 Submesoscales 3

Frontogenesis and Frontal arrest 6

1.2.3 Frontal Instabilities and Boundary Layer Turbulence 7

Wind Stress and Shear Turbulence 7

Convection 8

Langmuir Turbulence 8

Mixed Layer Instabilities 9

Potential Vorticity and Symmetric Instability 10

Horizontal Shear Instability 11

1.3 Modeling Multiscale Interactions 12

1.3.1 General Circulation Models 12

1.3.2 Large Eddy Simulations 14

1.4 Outline of Thesis 15

2 A Perturbation Approach to Understanding the Effects of Turbulence on Frontogenesis **16**

2.1 Introduction 16

2.2 Theory and Methods 18

2.2.1 Dimensionless expressions 20

2.2.2 Perturbation analysis 21

Zeroth order: inviscid, adiabatic 24

First order: turbulent fluxes 26

2.2.3 Potential Vorticity . . . 28
2.2.4 Boundary Conditions and First-Order Solution Procedure . . . 30
2.3 Results . . . 30
2.3.1 Surface Quasi-Geostrophy versus Interior Quasi-Geostrophy . . . 37
2.3.2 Point Source Surface Quasi-Geostrophy . . . 39
2.4 Summary and Discussion . . . 42

3 A Breakdown in Potential Vorticity Estimation Delineates the Submesoscale-to-Turbulence Boundary 44
3.1 Introduction . . . 44
3.2 Potential Vorticity and Spectral Analysis . . . 45
3.3 Modeled Potential Vorticity in Multiscale Simulations . . . 48
3.4 Pre-filtering and Reynolds Averaging . . . 53
3.5 Pre-filtered Potential Vorticity . . . 56
3.6 Discussion and Conclusions . . . 59

4 Arrest of Frontogenesis by Submesoscales and Boundary Layer Turbulence 63
4.1 Introduction . . . 63
4.2 Numerical Simulations . . . 65
4.3 Analysis . . . 67
4.3.1 Averaging . . . 67
4.3.2 Determining frontal width . . . 68
4.3.3 Other relevant parameters . . . 69
4.4 Summary of Results . . . 72
4.4.1 Convection/Symmetric Instability Case . . . 74
4.4.2 (Small) Mixed Layer Eddies Case . . . 76
4.4.3 Wind and Stokes Force Case . . . 76
4.4.4 All Forcing Case . . . 77
4.4.5 No Forcing Case . . . 77
4.5 Arrested Filament Frontogenesis . . . 77
4.6 Summary and Discussion . . . 80

5 Modifying the Mixed Layer Eddies Parameterization: Frontal Width Determined by Boundary Layer Turbulence 82
5.1 Introduction . . . 82
5.2 A new scaling for frontal width . . . 84
5.3 Proof of concept . . . 88
5.3.1 Testing in Large Eddy Simulations . . . 88
5.3.2 Estimates from the General Ocean Turbulence Model . . . 89
5.4 Implementation . . . 90

5.5 Summary and Discussion 91

6 Conclusions **96**

6.1 Summary and Implications 96

6.2 Future Work 98

6.2.1 Dominant frontal arrest mechanism 98

6.2.2 Further improvements on the Mixed Layer Eddies Parameterization 98

6.2.3 Effects on Climate 99

6.2.4 Atmospheric boundary layers and frontogenesis 99

A Code and Data **101**

B First Order Solution Numerical Scheme **102**

B.1 Parameters 102

B.2 First Order Solution 102

B.3 Boundary conditions 103

C Analytic Solution for the Delta Function Approximation **104**

List of Tables

2.1 Dimensionless expressions for quantities of interest following ST13 framework in the semi-geostrophic limit, which implies that the along-front velocity is purely geostrophic. 22

4.1 LES parameter configuration for the different simulation cases. 66
4.2 Estimated frontal widths (in meters) for each case, based on the distance from the front maximum determined by 1%, 10%, 50% of the maximum temperature gradient. 69
4.3 Estimate of simulation parameters over arrest region: boundary layer depth h, mixed layer depths defined by temperature and PV criteria $H_{\theta,q}$, along-front characteristic velocity scale U, turbulent Ekman number $Ek \equiv \frac{\overline{u'w'}}{hfU}$, Rossby number $Ro \equiv \frac{U}{fL_f}$, turbulent Richardson number $Ri \equiv N^2h^2/U^2$, turbulent Reynolds number $Re \equiv \frac{U^2}{\overline{u'v'}}$ and turbulent Prandtl number $Pr \equiv \frac{hN^2\overline{u'w'}}{U\overline{w'b'}}$ 75
4.4 As in table 4.2 for the SM cases. The first three columns represents the estimated frontal widths (in meters) on the left and right sides (noted by l, r superscripts), based on the distance from the front maximum determined by 1%, 10%, 50% of the maximum temperature gradient; The last column is the boundary layer depth. . . . 81

5.1 Dimensional parameters. Note that we do not need any of the thermal expansion parameters β or g, because they are represented by w_* and N. We are also assuming that Stokes drift is not a different scaling from u_* (i.e., fixed turbulent Langmuir number for fully-developed waves). The molecular viscosity ν_m and diffusivity κ_m can be suppressed assuming $Re = Uh/\nu_r \gg 1$ can neglect ν_m and $Pe = w_*h/\kappa_m \gg 1$ (e.g. Bodner and Fox-Kemper, 2020). 85
5.2 Dimensionless parameters, as in chapter 4 85
5.3 Estimate of parameterization constants given from strain-induced runs 89

List of Figures

1.1 Sea surface chlorophyll concentration in the Arabian Sea as viewed by the Moderate Resolution Imaging Spectroradiometer (MODIS) from NASA's Aqua satellite on February 22, 2005. White coloring indicates cloud cover. Data is given at an approximate resolution of 1km illustrating the different ocean scales, among those are submesoscale eddies and fronts. Image courtesy of Norman Kuring, MODIS Ocean Color Team. Caption and figure adapted from Mahadevan (2016) 2

1.2 An Argo profile example of temperature, potential density, and salinity to 2000 m from float 3900082 on 29 Jan 2003 at 52.78S, 89.78W. To 400 m, the float's sampling interval is 10 m, after which it increases to 50 m. This profile is from a Canadian Argo float, figure and caption adapted from Holte and Talley (2009). 4

1.3 Ocean surface boundary layer processes that contribute to mixing: wind shear, convection and Langmuir are discussed in section 1.2.3. Sketch is borrowed from (Thorpe, 2007) 5

1.4 Schematic adapted from McWilliams (2016) describing the dynamics involved in the strain-induced frontogenesis process of a front (a) and cold filament (b), illustrating the along-front/filament velocity at the surface and an overturning circulation in the interior. 6

1.5 Schematic of the Stokes drift, which represents the drift of a fluid parcel due to circular motion in the presence of winds and waves at the ocean surface (Thorpe, 2007). . . . 9

1.6 A temperature front (C^o) on day 20 of a typical spindown simulation from Fox-Kemper et al. (2008). H illustrates the mixed layer depth which enables the mixed layer instabilities to develop, and the eddy streamfunction Ψ represents the restratification due to the slumping front. 10

1.7 Schematic of conditions favorable to the development of symmetric instability. Down-front winds (thick arrow) drive an Ekman flow perpendicular to the wind vector and across the front (horizontal arrows), carrying dense water over light water. The associated Ekman buoyancy flux ($EBF > 0$), in conjunction with atmospheric cooling ($B_0 > 0$), reduces the stratification near the surface, destroys PV, and drives the fluid toward a symmetrically unstable state, leading to enhanced turbulence along isopycnals (colored planes). Caption and figure adapted from Bachman et al. (2017b). 11

1.8 Monthly zonal mean mixed layer depth given by the different boundary layer mixing schemes compared in Li et al. (2019). 13

1.9 Illustration of the energy spectrum $E(k)$ and inertial range for 3D turbulence, and how models such as LES mimic dissipation below the grid scale (blue vs red vertical lines), where k is the wavenumber. Adapted from Fox-Kemper et al. (2014). 14

2.1 Frontal formation of the dimensionless zeroth order buoyancy field (left), together with the cross-frontal planes showing the along-front velocity v (middle), and overturning streamfunction ψ (right). The cross-frontal, vertical and time axis correspond to the dimensionless x, z and t axis respectively. 26

2.2 Cross-frontal profiles of the zeroth order along-front velocity v^0 (shading) at two times defined as early frontogenesis ($t = 5$, left) and late frontogenesis ($t = 18$, right). Note the different colorbar axes. Superimposed in black contours is the buoyancy field, with intervals of 0.1 in non-dimensional units. Note the singularity developing during late frontogenesis. x and z are the dimensionless cross-frontal and vertical axes, respectively, in real space. 27

2.3 Contours show buoyancy as in figure 2.2, shading shows the zeroth order frontal tendency T_b^0. 27

2.4 Contours show buoyancy as in figure 2.2, shading shows the zeroth order streamfunction ψ^0. 27

2.5 Total frontal tendency $T_b = T_b^0 + \varepsilon T_b^1$ for each of the forcing cases, over a variety of ε (shades of blue), evaluated at the surface, where the zeroth order frontal tendency maximum (black) becomes infinitely strong. For each forcing case, the maroon line represents the ε for which $T_b = 0$. The green vertical line represents the time where the limit of the perturbation approach is reached for each forcing case: horizontal viscosity ($t = 11.1$), vertical viscosity ($t = 8$), horizontal diffusivity ($t = 8.4$), vertical diffusivity ($t = 9.1$). 31

2.6 Cross-frontal plane of the total frontal tendency $T_b = T_b^0 + \varepsilon T_b^1$ during early frontogenesis ($t = 5$) with the appropriate arrest ε for each forcing case: horizontal viscosity ($\varepsilon = 0.25$), vertical viscosity ($\varepsilon = 0.53$), horizontal diffusivity ($\varepsilon = 0.04$), vertical diffusivity ($\varepsilon = 0.51$). Black ticks indicate the location of the maximum zeroth order frontal tendency corresponding to that measured in figure 2.5 and for the sense of where the front is strongest. 32

2.7 Same as in figure 2.6 for the total along-front velocity $v = v^0 + \varepsilon v^1$. 33

2.8 Same as in figure 2.6 for the total streamfunction $\psi = \psi^0 + \varepsilon\psi^1$. 34

2.9 Cross-frontal planes of the first order along-front velocity v^1 at time t=5 for all forcing cases, calculated from the full system (a)-(d), the IQG system (e)-(h), the SQG system (i)-(l), the SQG system with a point source approximation (m)-(p), and the sum of the SQG and IQG systems(q)-(t). Note that for plotting purposes the IQG system is multiplied by a constant. 40

2.10 Same as in figure 2.9 for the first order streamfunction ψ^1. Note that for plotting purposes also here the IQG system is multiplied by a constant. 41

3.1 Plane view of a snapshot of the near-surface ($z = -3$m) temperature anomaly $\theta - \overline{\theta}$ after the development of submeosocale instabilities. Where $\overline{\theta} = 290.16K$ is the background temperature field. 49

3.2 Circularly integrated spectra of the velocity vector (u, v, w) normalized by the $z = -3$m values of the $E_u(k_{min})$ and buoyancy field b normalized by $E_b(k_{min})$, examined at depths: near surface (left, $z = -3$m), within the mixed layer (middle, $z = -25$m), and below the mixed layer (right, $z = -60$m). Dashed lines denote the $k^{-5/3}$ slope (light grey) and k^{-2} slope (dark gray) for reference. The shaded region is taken as the cutoff scale of 3D turbulence at $400m$ in the decomposition described in section 3.4. 50

3.3 Depth profiles of the dissipation rate ε (left) and Ozmidov scale wavenumber k_{Oz} (right). Black circles mark the three depths shown in figure 3.2. 51

3.4 Circularly integrated spectra of the buoyancy gradient components normalized by $E_{\mathbf{x}\cdot\nabla b}(k_{min})$ (top panels) at $z = -3$m and vorticity components normalized by $E_{\mathbf{x}\cdot\boldsymbol{\omega}}(k_{min})$ at $z = -3$m (bottom panels), at the same depths shown in Fig. 3.2. Here, dashed lines denote the $k^{2/3}$ slope (light grey) and $k^{1/3}$ slope (dark gray) for reference. Shaded region is the same as in Fig. 3.2. 52

3.5 Same as in figure 3.4 for PV in the Stokes drift forced case (light magenta) and No Stokes drift case (dark magenta). Thin lines denote the sharp cutoff pre-filtered PV and dotted lines denote the Gaussian pre-filtered PV for both cases, as discussed in section 3.5. Shaded region is the same as in Fig. 3.2. All spectra are normalized by $E_q(k_{min})$ at $z = -3$m of the No Stokes case. 53

3.6 Plane view of a snapshot of the near-surface ($z = -3m$) PV field without pre-filtering of the velocity and buoyancy fields (left), and after using a sharp cutoff filter (center) and Gaussian filter (right) on the buoyancy and velocity fields separately before calculating the PV as in (3.14). The cutoff scale here is 400m which corresponds to the shaded regions in Fig. 3.2,3.4 and 3.5. 58

3.7 Same as in Fig. 3.5 for the J-flux spectra in the No Stokes drift case. Shown is the total J-flux (top row) and its components: $q\mathbf{u}$ (second row), $\mathbf{F} \times \nabla b$ (third row), and $(\mathbf{f} + \boldsymbol{\omega})\mathcal{D}$ (bottom row). Thick lines denote the unfiltered spectra, thin lines the sharp cutoff pre-filtering and dotted lines the Gaussian pre-filtering as described in section 3.5. All spectra are normalized by $E_{\mathbf{x}\cdot\mathbf{J}}(k_{min})$ at $z = -3$m. 62

4.1 An example of the confluent sub-domain of the strain-induced front for the convection/SI case (left), and a plane view of the pressure field (contours), overlaid by the smoothed pressure lines (black) over which the along-front smoothing is calculated to obtain the mean variables displayed in figures 4.2-4.6 (right). 68

4.2 Cross-frontal mean fields for the convection/SI case: temperature anomaly $\overline{\theta} - \theta_0$ (top left), along-front velocity $\overline{u}$ (top right), cross-front velocity $\overline{v}$ (bottom left) and vertical velocity $\overline{w}$ (bottom right). Black bars and the L_f values below the mean temperature panel correspond to $L^{1\%}_{\nabla\theta}$, $L^{10\%}_{\nabla\theta}$ and $L^{50\%}_{\nabla\theta}$ from table 4.2. 69
4.3 Same as in figure 4.2 for the MLI case. 70
4.4 Same as in figure 4.2 for the mixed layer instability for the Stokes+wind case. 71
4.5 Same as in figure 4.2 for the all forcing case. 72
4.6 Same as in figure 4.2 for the no forcing case. 73
4.7 Cross-frontal mean total TKE for the convection/SI case (left), and its TKE production and dissipation terms (right) averaged over the frontal region. The vertical gray line and the corresponding value of h below illustrate the boundary layer depth estimated by the depth over which 90% of the TKE has occurred. In the right panel, b prod. and shear prod. refer to the buoyancy and shear production terms from the TKE budget, respectively. 73
4.8 Same as in figure 4.7 for the MLI case. 74
4.9 Same as in figure 4.7 for the Stokes and wind case. 74
4.10 Same as in figure 4.7 for the all forcing case. 74
4.11 Same as in figure 4.7 for the no forcing case. 75
4.12 The cross-filament variation of the average vertical vorticity normalized by the Coriolis parameter $\langle\zeta\rangle/f$ (red) and average cross-filament Lagrangian current $\langle u^L\rangle/u_*$ (black) shown in panel (a), the average along-filament current $\langle v\rangle/u_*$ normalized by the friction velocity scale $u_* = 0.01 m/s$ (cyan) in (b). The vorticity and currents are near the water surface $z \sim -5m$. Instantaneous down-welling velocity $w/u_* < 0$ in a horizontal plane at $z = -10.5$ m, (c). Results are for simulation $E + e$ from SM. Figure and caption are adapted from Sullivan and McWilliams (2019). 78
4.13 Upper 5m average of the temperature anomaly in the cross-filament direction for the SM cases associated with convection: C+e (top left), C+n (top right), C (bottom left) and a typical cross-filament profile of the temperature anomaly in the pure convection case (bottom right). The Black bars in the surface temperature plots and L_f, h listed below correspond to sharper values of $L^{1\%}_{\nabla\theta}$, $L^{10\%}_{\nabla\theta}$ and $L^{50\%}_{\nabla\theta}$, and the boundary layer depth, as listed in table 4.4. 79
4.14 Similar to figure 4.13 for the SM wind cases: N (top left), N+n (top right), E (bottom left), E+e (bottom right). 80

5.1 Log-log plot of the measured $L^{1\%}_{\nabla\theta}$ frontal width found in chapter 4 compared with the L_f prediction based on the new scaling (5.21), using the appropriate u_*, w_*, h, f for each case, and constants set to $m_*, = 0.5$, $n_* = 0.066$, $C_L = 0.25$. Gray error bars represent the measured frontal width given by $L^{10\%}_{\nabla\theta}$. 89
5.2 L_f (m) estimated from GOTM in the Bay of Bengal using u_*, w_* and CVmix to determine h. 90

5.3 Global maps of mean mixed layer depth during summer in the Northern Hemisphere (July-September) and Southern Hemisphere (January-March) from: observations given by the de Boyer Montégut et al. (2004) dataset updated to include Argo data up to 2012 (top left), zonal average of all simulations (top right), new Lf vs control in the coupled simulations (middle panels) and forced simulations (bottom panels) 93
5.4 Same as figure 5.3 during winter in the Northern Hemisphere (January-March) and Southern Hemisphere (July-September). 94
5.5 Differences between new L_f and control in the coupled simulations during summer and winter in both hemispheres, as in figure 5.3. Note the different colorbars to emphasize regional variability. 95
5.6 Same as in figure 5.5 for the forced simulations. 95

Chapter 1

Introduction

Parts of this introduction were drawn from work published as: Abigail S. Bodner, Baylor Fox-Kemper, Luke P. Van Roekel, James C. McWilliams, and Peter P. Sullivan. "A perturbation approach to understanding the effects of turbulence on frontogenesis." Journal of Fluid Mechanics, 883, A25. doi:10.1017/jfm.2019.804

1.1 Motivation

On the global scale, the ocean contains over ninety percent of the carbon on Earth (aside from geological reservoirs), and has a large capacity to store and release heat, thus acting as one of the most important regulators to the climate system, and therefore the fate of rising temperatures (Pörtner et al., 2019). Ocean circulation and mixing redistributes heat, salt and carbon over a wide range of spatial and temporal scales: from global processes such as water mass transport, sea level and heat content changes, to small scale processes such as mixing heat, momentum and air-sea interactions (Siedler et al., 2013). Each have unique dynamical, statistical and energetic properties that can be transferred across scales from planetary scale flows, down to turbulence and the dissipative scales (e.g. Capet et al., 2008c; Ferrari and Wunsch, 2009; Molemaker et al., 2010; Callies et al., 2016). Horizontal mixing and transport, as well as over half of the kinetic energy in the ocean, is dominated by mesoscale eddies. They can span as large as hundreds of kilometers in horizontal length and months in time evolution. However, vertical mixing and heat transport are dominated by the submesoscale and 3D turbulence range (e.g Klein et al., 2009).

Submesoscales span the range of $0.1 - 10$km in horizontal scale (illustrated in figure 1.1), $0.01 -$ 1km in vertical scale and hours to days in time evolution, and boundary layer (3D) turbulence is on the order of meters in length and minutes to hours in time (Grant and Belcher, 2009; McWilliams, 2016). These scales are particularly evident in the ocean surface, where the dynamic interplay between submesoscales and boundary layer turbulence modulate the transfer of heat, momentum, carbon and other properties, between the atmosphere and ocean interior (e.g., Bachman et al., 2017b; Renault et al., 2018), and therefore are instrumental in determining the ocean's response

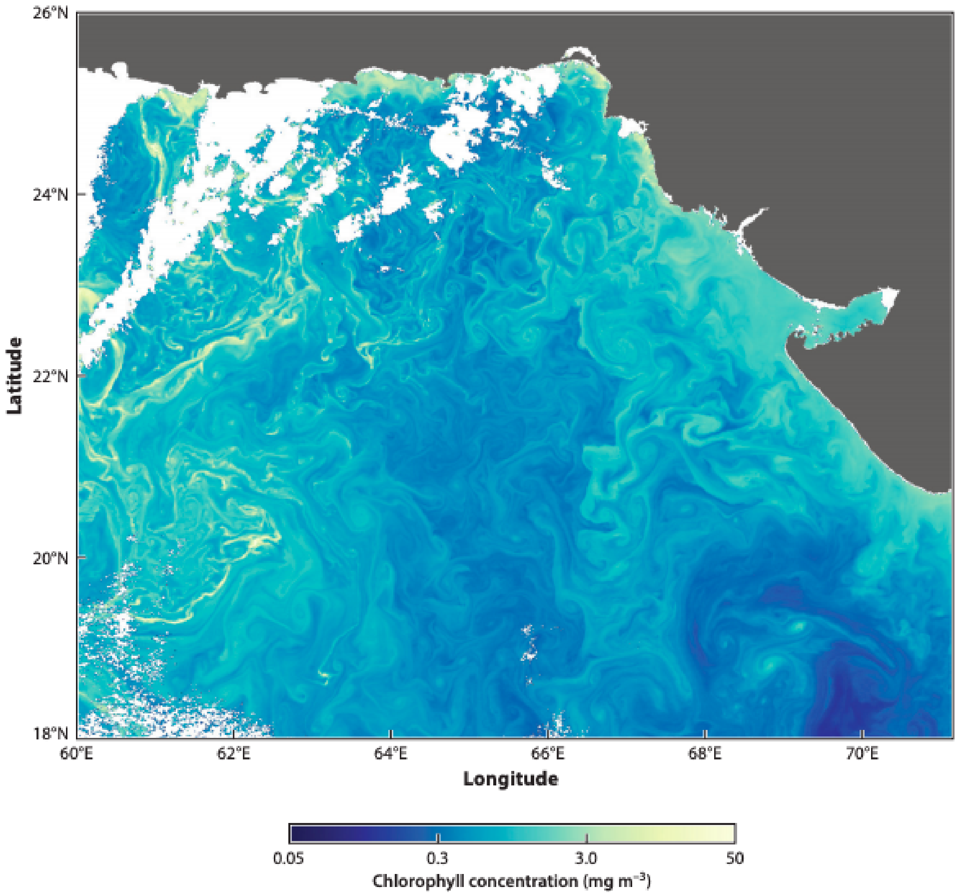

Figure 1.1: Sea surface chlorophyll concentration in the Arabian Sea as viewed by the Moderate Resolution Imaging Spectroradiometer (MODIS) from NASA's Aqua satellite on February 22, 2005. White coloring indicates cloud cover. Data is given at an approximate resolution of 1km illustrating the different ocean scales, among those are submesoscale eddies and fronts. Image courtesy of Norman Kuring, MODIS Ocean Color Team. Caption and figure adapted from Mahadevan (2016)

to a changing climate. However, because of the fast time scale and relatively small spatial scales, it has been challenging to study submesoscales and boundary layer turbulence, as they are small and impermanent, requiring new strategies for ship surveys, satellite detection and climate models (McWilliams, 2016).

Building toward a more complete understanding of these processes, and how they interact, this thesis investigates and quantifies the interaction between submesoscales and boundary layer turbulence through theory, multiscale numerical simulations and general circulation models.

1.2 Phenomenology

1.2.1 The ocean surface layer

The ocean surface is the most turbulent layer in the ocean, driven primarily by winds, waves and buoyancy forcing (e.g Reichl and Hallberg, 2018). The ocean surface layer can broadly be described as the layer in which temperature, salinity and other tracers are vertically well mixed. It is the connecting layer with the atmospheric boundary, where air-sea fluxes take place, and links the deep ocean waters with the free atmosphere through vertical mixing and surface ventilation (Fox-Kemper et al., 2020). Furthermore, vertical mixing processes near the ocean surface are critical in transporting tracers and supplying essential nutrients to marine biology (Taylor and Ferrari, 2011; Smith et al., 2016; Mahadevan, 2016; Olita et al., 2017; Lévy et al., 2018).

It is important to differentiate between the *mixed* layer and the *mixing* layer. The ocean mixing layer, also known as the ocean surface boundary layer, is where turbulence– usually estimated by turbulent kinetic energy or turbulent dissipation– is most active. The boundary layer depth is determined primarily by surface forcing and is sensitive to the diurnal cycle (e.g. heating or cooling), wind direction and stress magnitude, and even passing storms with increased precipitation (Kraus and Turner, 1967; Price, 1981; Price et al., 1986; Belcher et al., 2012; Li et al., 2019).

The mixed layer depth however, may lag or be entirely independent of the instantaneous boundary layer, as it does not solely depend on surface forcing. The observed mixed layer depth results from the combined effects of deepening mixing (entrainment) processes and shoaling restratification processes. Both the mixed layer and boundary layer tend to be deeper during winter, when strong surface forcing leads to more intense mixing (e.g. Holte et al., 2017).

The mixed layer depth is typically estimated by where tracers (e.g. salinity, temperature, density) or certain dynamical properties (e.g. potential vorticity, stratification) exceed a certain threshold relative to their surface values. Ship surveys and Argo profiles estimate the mixed layer depth from observations, yet there is still debate over what algorithm is most reliable (de Boyer Montégut et al., 2004; Holte et al., 2017; Li and Fox-Kemper, 2017). An example is demonstrated in figure 1.2, for which the mixed layer depth is obtained from an Argo profile, following the de Boyer Montégut et al. (2004) criteria of $0.28C$ for the temperature and 0.03 kg m^{-3} for the density, and a surface reference level of $10m$ to eliminate diurnal surface heating effects (Holte et al., 2017).

However, the focus here is not on how to best estimate the mixed layer depth, but rather on the actual processes competing for mixing and deepening vs restratifying and shoaling it. An illustration of the different mixing processes at the ocean surface are shown in figure 1.3, and are described in more depth in section 1.2.3.

1.2.2 Submesoscales

Submesoscale currents can be found in the form of density fronts and filaments, coherent vortices and topographic wakes (e.g. Flament et al., 1985; Fedorov, 1986). Submesoscale fronts and filaments are most commonly generated by mesoscale straining and boundary layer turbulence (McWilliams,

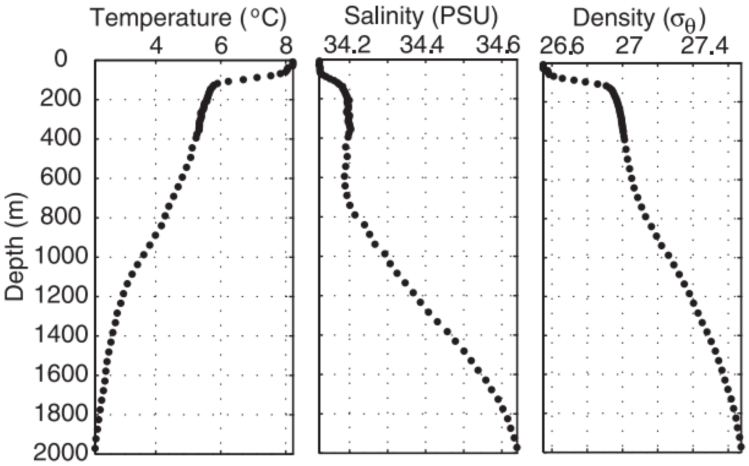

Figure 1.2: An Argo profile example of temperature, potential density, and salinity to 2000 m from float 3900082 on 29 Jan 2003 at 52.78S, 89.78W. To 400 m, the float's sampling interval is 10 m, after which it increases to 50 m. This profile is from a Canadian Argo float, figure and caption adapted from Holte and Talley (2009).

2021), and are thus more evident during winter, when strong surface forcing leads to stronger boundary layer mixing (Rudnick and Ferrari, 1999; Ferrari and Rudnick, 2000; Callies et al., 2015) or in regions with strong mesoscale eddies (Capet et al., 2008a; Sasaki et al., 2014; Brannigan et al., 2015; Buckingham et al., 2016). Furthermore, coastlines and marginal ice zones provide a source of fresh water, generating density fronts and filaments by other sources and that may have land-dependent seasonal variability (Luo et al., 2016; Mensa et al., 2013, 2018).

Due to their small size and rapid behaviour, submesoscale currents have historically been understudied, as it has been difficult to obtain measurements from standard ship surveys and remote sensing satellites (e.g. Weller and Samelson, 1991; Hosegood et al., 2006; Zhang et al., 2019). Other techniques such as targeted ship surveys, high frequency radars of sea level anomalies, surface drifters, drone and aerial footage are often utilized in multi-platform observational campaigns specifically designed for the purpose of studying surface submesoscales (e.g. Gildor et al., 2009; Chavanne and Klein, 2010; Shcherbina et al., 2015; Novelli et al., 2017). However, these studies are performed on regional scales, and a complete understanding of how submesoscales behave on the global scale is still lacking (Ullman and Cornillon, 1999; Dong et al., 2020).

From an energetic perspective, mesoscales tend to merge, transferring kinetic energy from smaller scales to the larger scales (inverse cascade), and so do not provide an easy route to dissipation (Ferrari and Wunsch, 2009). Therefore, submesoscale currents are thought to be a key component in the forward energy cascade in the ocean (Molemaker et al., 2010; D'Asaro et al., 2011; Gula et al., 2016), primarily due to loss of balance, interaction with inertia-gravity waves, and finer turbulent structures that emerge along the currents (Thomas, 2012; Vanneste, 2013; Shakespeare and Taylor, 2014). Submesoscales tend to overlap in scale with inertia-gravity waves, and it is often difficult to

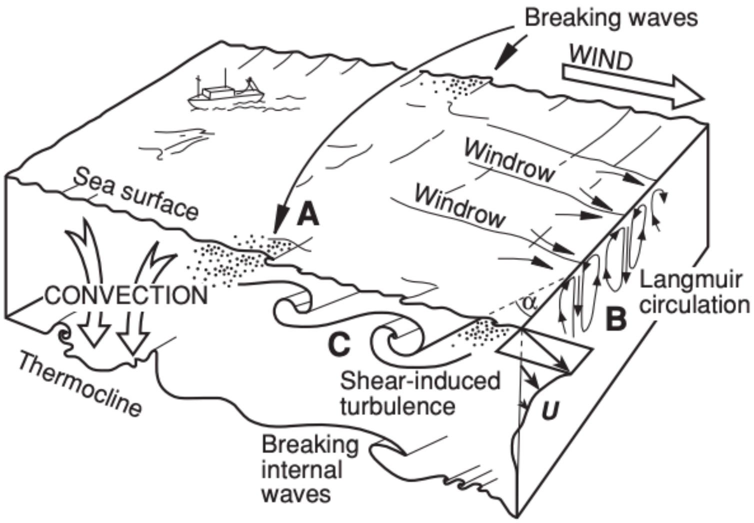

Figure 1.3: Ocean surface boundary layer processes that contribute to mixing: wind shear, convection and Langmuir are discussed in section 1.2.3. Sketch is borrowed from (Thorpe, 2007)

distinguish between them in observational measurements (Cao et al., 2021). However, inertia-gravity waves are characterized by oscillatory propagation, whereas the submesoscale currents discussed here are a unique dynamical class (Shakespeare and Taylor, 2014).

In planetary and mesoscale flows, several approximations are made that greatly simplify the equations of motion. These simplifications allow for analytic solutions that have historically helped the understanding of large scale atmospheric and oceanic flows. To explore the dominant forces that govern the flow, it is useful to quantify the relative scale of different terms in the equations of motion via dimensionless parameters. For example, the Rossby number $Ro = U/fL$, represents the ratio of inertial forces to the Coriolis force i.e. Earth's rotation (U and L are a characteristic horizontal velocity and length scales, f is the Coriolis frequency parameter). The Froude number $Fr = U/NH$ represents the ratio of inertial forces to the gravity force (H is a characteristic vertical length scale, $N = \sqrt{-\frac{g}{\rho}\frac{\partial \rho}{\partial z}}$ is the Brunt-Väisälä buoyancy frequency, g is gravity and ρ is density). Similarly, the Richardson number represents the ratio of buoyancy frequency to vertical shear $Ri = N^2/(\partial_z U)^2$ (Pedlosky et al., 1987). Typically in large scale flows, where rotation and stratification govern the flow, $Ro, Fr \ll 1$ and $Ri \gg 1$, meaning inertial forces are negligible in this limit. In the submesoscale, the Rossby, Froude and Richardson numbers are typically all on the order of $O(1)$ and thus not negligibly small as in the meso- and planetary scales (e.g. Thomas et al., 2008; McWilliams, 2016). Practically, this means that these terms cannot be ignored, and nonlinear terms need to be fully accounted for in the equations of motion. Thus, from a theoretical perspective, many of the clean solutions that exist for mesoscale and planetary scale flows, do not apply for the submesoscale, and creative techniques are required to describe these flows theoretically and numerically.

Frontogenesis and Frontal arrest

Fronts and filaments are an important and ubiquitous submesoscale feature of the ocean surface (illustrated in figures 1.1 and 1.4). They are characterized by elongated sharp horizontal density gradients, and an overturning circulation in the interior, working to restore stratification and thermal wind balance, as mixing and strain alter the front (McWilliams, 2017). A filament is dynamically similar to a two-sided front, with anomalously dense or light water in the middle. Dense filaments are found to be more common in the ocean due to their stronger formation mechanism (McWilliams, 2021).

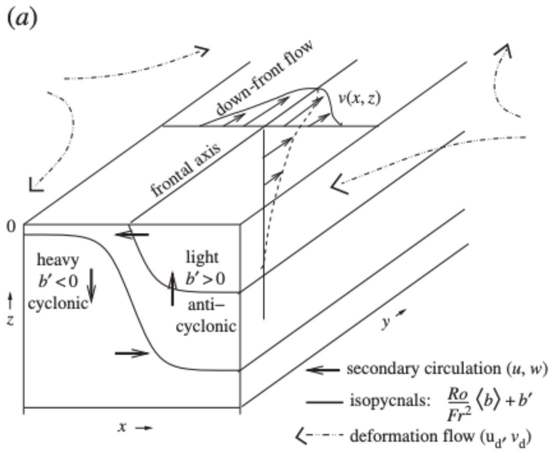

Figure 1.4: Schematic adapted from McWilliams (2016) describing the dynamics involved in the strain-induced frontogenesis process of a front (a) and cold filament (b), illustrating the along-front/filament velocity at the surface and an overturning circulation in the interior.

The process involving the formation and sharpening of fronts is known as frontogenesis, and was originally developed for the atmosphere, where they are critical for the understanding and prediction of weather (e.g. Hoskins, 1982; Davies and Rossa, 1998). In the ocean, the mixed layer is weakly stratified in the vertical, thus horizontal density gradients can become dominant, and strengthen to form sharp fronts. Two primary mechanisms are found to onset frontogenesis: a density gradient in the presence of an external strain field (e.g. mesoscale eddies), and vertical turbulent fluxes (e.g. boundary layer turbulence).

Classic **strain-induced frontogenesis** theory was originally developed by Hoskins and Bretherton (1972) in a semigeostrophic framework, which assumes geostrophic balance in the along-front direction, thus reducing to a 2D inviscid, adiabatic flow (i.e. no turbulence) in the cross-frontal plane. Classic frontogensis theory is able to describe frontal dynamics at leading order, by solving for the along-front current (at the top and bottom of the mixed layer) and a cross-frontal ageostrophic (i.e. not in geostrophic balance) overturning circulation. However, it results in an infinitely narrow front in a finite time, a nonphysical limit that does not comply with observations or numerical simulations. Furthermore, semigeostrophy is found to be inaccurate for 3D flows such as elongated fronts where curvature matters or during late frontogenesis when instabilities develop along the front (Rotunno et al., 1994; Gent et al., 1994).

A different approach combines geostrophic and boundary layer theories, as expected for submesoscale fronts in the ocean surface boundary layer (McWilliams, 2016). Here, Ekman and thermal wind are both assumed to be at first order, thus leading to a three-way balance between vertical shear $s(z) = \frac{\partial \mathbf{u}_H}{\partial z}$, the horizontal buoyancy gradient $\nabla_H b(z)$, and turbulent viscosity ν generated by surface winds $\frac{\partial^2(\nu\ \mathbf{s})}{\partial z^2}$,

$$f\hat{\mathbf{z}} \times \mathbf{s} = -\nabla_H b + \frac{\partial^2(\nu\ \mathbf{s})}{\partial z^2}. \tag{1.1}$$

This process of **turbulence-induced frontogensis** is also known as the Turbulent Thermal Wind (TTW) balance, and was developed by McWilliams et al. (2015). TTW theory is able to describe fronts and filaments at scales much sharper than semigeostrophic theory, and more consistent with the observed ocean submesoscale. However, it is very difficult to observe the strain field and turbulent fluxes in the ocean, and observations of TTW are scarce. Regional ocean models have been useful tools for studying TTW behavior in a near-realistic environment (e.g. Gula et al., 2014; Dauhajre and McWilliams, 2018), and only recently have high resolution numerical simulations been able to simulate the multi-scale TTW range. Sullivan and McWilliams (2018, 2019) are among the first to simulate a dense filament undergoing TTW frontogensis in the presence of realistic surface boundary layer turbulence.

Both approaches predict frontogenesis to proceed until disrupted by turbulent fluxes that arrest the ever strengthening front. These turbulent fluxes can either be the result of frontal instabilities or existing boundary layer turbulence from ocean surface processes such as winds, waves and surface cooling (McWilliams, 2021). This thesis is rooted in understanding under what conditions submesoscale frontal arrest is possible and at what scale.

1.2.3 Frontal Instabilities and Boundary Layer Turbulence

Wind Stress and Shear Turbulence

Wind stress along the ocean surface is the main cause for shear turbulence in the ocean surface boundary layer. This is the dominant process generating turbulence in a stable or neutrally stratified boundary layer, i.e. dominated by momentum fluxes rather than heat or buoyancy flux.

The friction velocity u_* represents the characteristic velocity scale in the boundary layer given from wind stress, and is derived directly from Ekman dynamics (Wyngaard, 2010),

$$u_* = \sqrt{\frac{|\tau_0|}{\rho_0}}, \tag{1.2}$$

where τ_0 is the wind stress and $\rho_0 \sim 1025\text{kg m}^{-3}$ is the reference density at the surface.

It is common in turbulence literature to describe how turbulent the flow is in terms of how high is its Reynolds number $Re = UL/\nu$, where U and L are characteristic velocity and length scales, and ν typically represents molecular viscosity. However, the turbulence discussed here mostly refers to eddy fluxes, not molecular, and can be quantified in terms of an eddy viscosity $\nu = -\overline{\mathbf{u}'w'}/\frac{\partial \overline{\mathbf{u}}}{\partial z}$, and will therefore have a relatively low effective Reynolds number (where $\overline{\mathbf{u}'w'}$ is the mean vertical momentum flux and $\frac{\partial \overline{\mathbf{u}}}{\partial z}$ is the mean horizontal shear).

Convection

During a diurnal cycle, the ocean surface is heated and cooled by latent and sensible heat, as well as short and long-wave radiation. Most significantly, surface cooling combined with penetrating short wave radiation leads to unstably stratified (cold over warm) waters, which will then drive convection. This is essentially the classic convection case driven by Rayleigh Benard (or gravitational) instability (Haine and Marshall, 1998; Fox-Kemper et al., 2020).

It is common for both buoyancy fluxes and wind stress to be present at the ocean surface. The Monin-Obukhov (MO) length scale represents the effects of wind stress and convection within the boundary layer, combined into one characteristic length scale ,

$$L_{MO} = -\frac{u_*^3}{\kappa B_0}, \tag{1.3}$$

where u_* is the friction velocity scale, B_0 is the surface buoyancy flux ($B_0 > 0$ for destabilizing surface buoyancy flux), and $\kappa = 0.4$ is the Von Karman constant. The MO theory specifies whether convective or shear turbulent conditions are favorable in the boundary layer. Specifically, $z/L_{MO} < 0$ indicates convection and $z/L_{MO} > 0$ indicates shear turbulence in stable stratification (Fox-Kemper et al., 2020).

Similar to the friction velocity, the convective velocity w_* represents the characteristic velocity scale in a convective boundary layer. The scaling for w_* is extended from the MO theory for a convective boundary layer, and introduces an additional parameter for the boundary layer depth h (Deardorff et al., 1970; Wyngaard, 2010),

$$w_* = (B_0 h)^{1/3}. \tag{1.4}$$

The MO length scale can also be written in terms of w_*, which introduces a more intuitive interpretation of estimating shear vs convective turbulence in the boundary layer,

$$L_{MO} = -\frac{h}{\kappa}\frac{u_*^3}{w_*^3}. \tag{1.5}$$

The friction and convective velocity scales are principal parameters in representing boundary layer turbulence in climate models, as will be discussed in section 1.3.

Langmuir Turbulence

Waves are perhaps the most noticeable ocean surface phenomena, and are part of how boundary layer theory in the ocean differs from the atmosphere. Although waves are important for air-sea interactions by introducing bubbles and spray through wave breaking, here we focus on the turbulence induced by their non-breaking dynamics (e.g. Sullivan and McWilliams, 2010; Cavaleri et al., 2012). Surface waves introduce an averaged velocity associated with the circular motion of a fluid parcel carried by the waves. This is known as the Stokes drift, and is exhibited to be strongest at the surface and decays with depth (figure 1.5). The interaction between surface winds and the Stokes drift leads to the formation of windrows (displayed in figure 1.3), which are the surface convergence zones of Langmuir circulation cells that generate Langmuir turbulence (Grant and Belcher, 2009). Langmuir turbulence is typically confined to the top several meters, but its effects can penetrate much farther, entraining and deepening the mixed layer base (Li and Fox-Kemper, 2017).

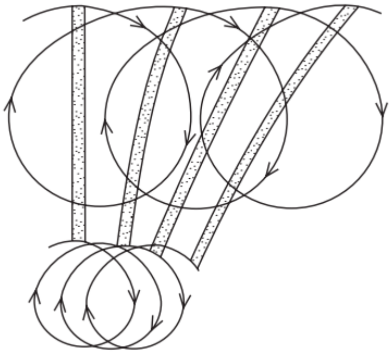

Figure 1.5: Schematic of the Stokes drift, which represents the drift of a fluid parcel due to circular motion in the presence of winds and waves at the ocean surface (Thorpe, 2007).

The Langmuir number $La_t^2 = u_*/u_s$ represents the ratio between the surface Stokes drift velocity u_s and the friction velocity (McWilliams et al., 1997), and has numerous theoretical and computational applications, as will be discussed in section 1.3.

Mixed Layer Instabilities

In addition to the standard ocean surface boundary layer turbulence, there exist a unique class of instabilities that arise from the presence of horizontal density gradients in the mixed layer, such as those introduced by submesoscale fronts.

The vertical isopycnals introduced by the front contain a source of available potential energy (Eady, 1949; Stone, 1970). Illustrated in figure 1.6, baroclinic instability converts available potential energy into kinetic energy in the form of eddies, acting to slump the front, bringing light water over dense, and therefore having an overall restratifying effect (Lapeyre et al., 2006; Fox-Kemper et al., 2008). Baroclinic instability also occurs on the mesoscale, but mixed layer instabilities are constrained by the weak stratification in the mixed layer, and thus confined to the mixed layer depth (Boccaletti et al., 2007).

Restratification can also occur after an initial geostrophic adjustment of the front, i.e. tilting of the front while it attempts to reach a gesotrophically balanced state (Blumen, 1972; Ou, 1984; Tandon and Garrett, 1994), yet mixed layer instabilities lead to stronger restratification, particularly after the mixed layer eddies reach finite amplitude (Boccaletti et al., 2007; Fox-Kemper et al., 2008).

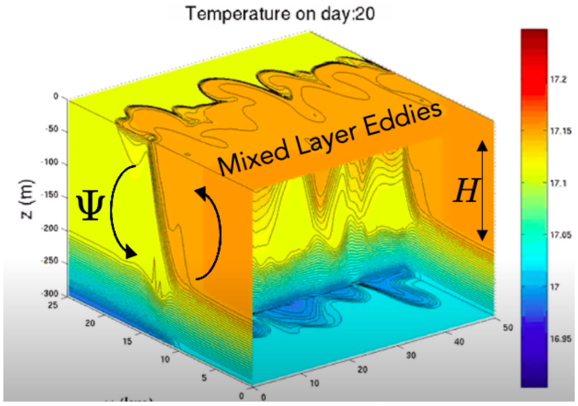

Figure 1.6: A temperature front (C^o) on day 20 of a typical spindown simulation from Fox-Kemper et al. (2008). H illustrates the mixed layer depth which enables the mixed layer instabilities to develop, and the eddy streamfunction Ψ represents the restratification due to the slumping front.

Potential Vorticity and Symmetric Instability

Potential vorticity (PV) is a fundamental dynamical property in atmospheric and oceanic fluid dynamics. The Ertel PV combines the two main drivers of planetary flow: rotation and stratification,

$$q = (\omega + f\hat{k}) \cdot \nabla b, \tag{1.6}$$

where $\omega = \nabla \times \mathbf{u}$ is the relative vorticity, $\mathbf{u}$ is the velocity vector, $f\hat{k}$ is the vertical planetary rotation, $b = -g\rho/\rho_0$ is buoyancy, g being gravity acceleration, and ρ is the density (Charney, 1971; Pedlosky et al., 1987).

In shallow flows such as submesoscale currents in the mixed layer, surface quasi-geostrophy (SQG) has been found to be useful to describe flows beneath the surface, especially as satellite observations and surface measurements are more widely available (e.g. LaCasce and Mahadevan, 2006; Chavanne and Klein, 2016). Surface boundary conditions of the temperature and subsurface velocities are approximated to invert the surface PV, which can be sufficient to prescribe the interior flow field (e.g. Bretherton, 1966; Lapeyre and Klein, 2006).

Several instabilities arise when the PV takes the opposite sign of the Coriolis parameter, $fq < 0$. Most relevant to ocean surface mixing is that of symmetric instability (e.g. Hoskins, 1974; Thomas et al., 2013). The presence of a strong frontal horizontal buoyancy gradient, surface cooling and winds in the along-front direction (down-front winds) will result in negative PV (Thomas, 2005) which are favorable for symmetric instability. Waves can also affect the PV through the alignment of the Stokes and geostrophic shears (Haney et al., 2015). Symmetric instability is sometimes also referred to as slantwise convection, because it occurs when the direction of mixing slants along the front (illustrated in figure 1.7).

Negative PV is also a signature of mode water (also known as eighteen degree water), that represent an important pathway for heat and carbon from the ocean surface to the interior, and even influence gyre-scale circulation (e.g. Wenegrat et al., 2018).

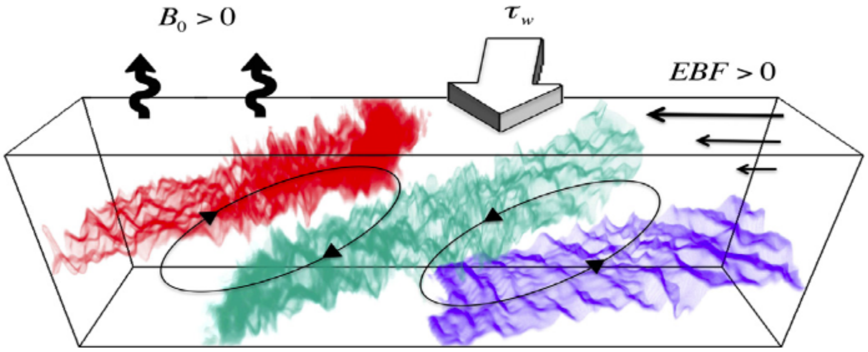

Figure 1.7: Schematic of conditions favorable to the development of symmetric instability. Down-front winds (thick arrow) drive an Ekman flow perpendicular to the wind vector and across the front (horizontal arrows), carrying dense water over light water. The associated Ekman buoyancy flux ($EBF > 0$), in conjunction with atmospheric cooling ($B_0 > 0$), reduces the stratification near the surface, destroys PV, and drives the fluid toward a symmetrically unstable state, leading to enhanced turbulence along isopycnals (colored planes). Caption and figure adapted from Bachman et al. (2017b).

For this reason, there is special interest to track the evolution of PV and study which processes may lead to a negative sign,

$$\frac{\partial q}{\partial t} = -\nabla \cdot [\mathbf{u}q - \omega D + \nabla b \times \mathbf{F}], \tag{1.7}$$

where $\mathbf{F}$ and D are the frictional and diabatic fluxes which arise directly from the momentum and thermodynamic equations respectively, (Haynes and McIntyre, 1987; Marshall and Nurser, 1992)

$$\mathbf{F} = \frac{\partial \mathbf{u}}{\partial t} + \mathbf{u} \cdot \nabla \mathbf{u} + \frac{1}{\rho}\nabla P + f\hat{k} \times \mathbf{u}, \tag{1.8}$$

$$D = \frac{\partial b}{\partial t} + \mathbf{u} \cdot \nabla b. \tag{1.9}$$

These frictional and diabatic terms represent both molecular and turbulent fluxes, and are thus key to connecting submesoscale dynamics with surface boundary layer turbulence. This method has especially been instrumental in describing the effects of friction on frontogenesis, where wind stress– based on its direction– induces an Ekman flow that can either reinforce or degrade stratification in the mixed layer (e.g. Thomas and Rhines, 2002; Thomas and Ferrari, 2008; Crowe and Taylor, 2020).

Horizontal Shear Instability

Similar to Kelvin-Helmholtz instability, horizontal shear instability occurs where there is horizontal shear across the interface between two fluids. The growth rate for horizontal shear instability is characterized by a Richardson number below $Ri < 0.25$ (Stone, 1966). Horizontal shear instability can form along the submesoscale front, due to concentrated shear, and has been shown to be the primary arrest mechanism for frontogenesis in several simulations (Taylor and Ferrari, 2009; Gula et al., 2014; Sullivan and McWilliams, 2018, 2019).

1.3 Modeling Multiscale Interactions

1.3.1 General Circulation Models

General Circulation Models (GCMs) are limited in their ability to resolve the convoluted interactions between the atmosphere, ocean, land and biology, over all relevant time and spatial scales. Hence, they simulate these interactions by including as many processes as computational constraints permit, while processes too small, fast, or complex are approximated through parameterizations. These reduced mathematical expressions capture the leading order physics, yet must remain computationally efficient and commute with other components of the GCM.

Computational fluid dynamics models, which include GCMs, typically solve the equations of motion for the mean field $\overline{\phi}$ (e.g. Vallis, 2017), where $\bar{\cdot}$ represents any resolved variable that is advanced in time, e.g. velocity or tracers such as temperature and salinity. Deviations from the mean are often noted by $\cdot'$, and they can affect the evolution of the mean field through forcing or advection terms. A simplified example of what these equations may look like in a GCM are written as,

$$\frac{\partial \overline{\phi}}{\partial t} + \overline{\mathbf{u}} \cdot \nabla \overline{\phi} = -\nabla \cdot \overline{\mathbf{u}'\phi'}, \tag{1.10}$$

where the term $\overline{\mathbf{u}'\phi'}$ represents the unresolved fluxes of ϕ'.

Submesoscales and boundary layer turbulence tend to be on scales smaller than the grid used in GCMs, even at the highest possible resolution (Dong et al., 2020). Accurate representation of these processes is especially important for climate simulations as they determine the effective mixed layer depth, through which even modest adjustments have a major impact on climate sensitivity (Fox-Kemper et al., 2019; Hall and Fox-Kemper, 2021). To emphasize this point, figure 1.8 demonstrates the wide range of possible mixed layer depths which result from different boundary layer mixing schemes.

As turbulence mainly acts to stir and diffuse the fluid (Thorpe, 2005), two main parameterization methods emerge to represent these effects in GCMs. Stirring tends to be represented by a bolus velocity ($\mathbf{u}^B$) *included as an advection term* in the governing equations that are solved by the GCM (Gent and Mcwilliams, 1990; Griffies, 1998). These velocities are given by a streamfunction ($\mathbf{\Psi}$), representing the submesoscale eddy fluxes produced by the restratifying effect of a slumping front (also illustrated in figure 1.6),

$$\underbrace{\overline{w'b'}}_{\text{Eddy fluxes}} = \mathbf{\Psi} \times \nabla_H \overline{b}, \qquad \underbrace{\mathbf{u}^B}_{\text{Bolus velocity}} = \underbrace{\nabla \times \mathbf{\Psi}}_{\text{Streamfunction}}. \tag{1.11}$$

However, current submesoscale parameterizations have been shown to be too simplistic and unfitting in many circumstances (e.g. Callies and Ferrari, 2018; Calvert et al., 2020), primarily due

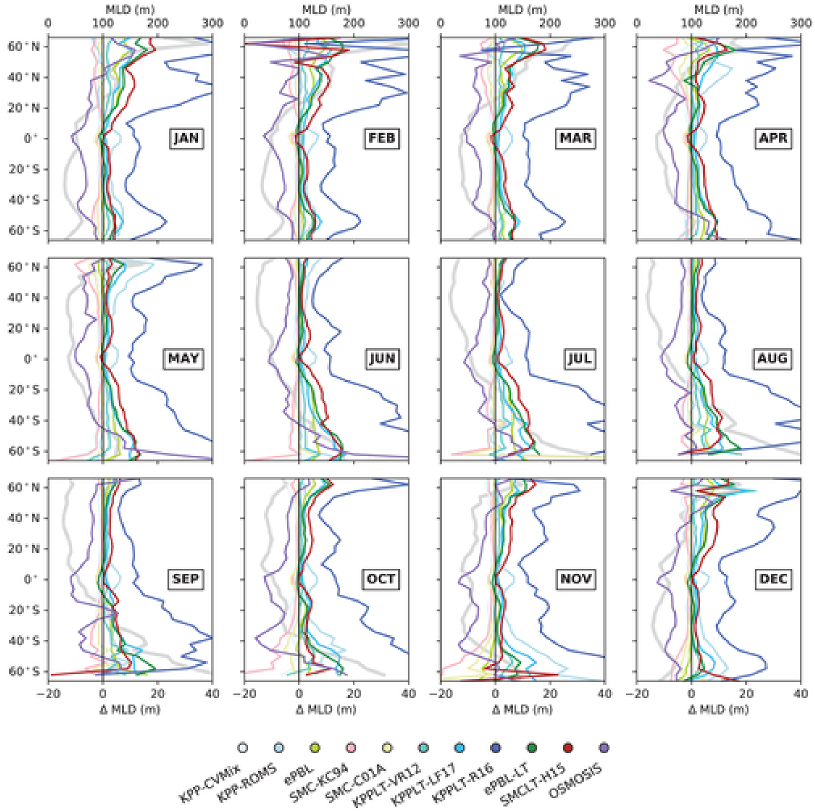

Figure 1.8: Monthly zonal mean mixed layer depth given by the different boundary layer mixing schemes compared in Li et al. (2019).

to their strong dependence on frontal width, for which no scaling law exists to comprehensively evaluate it, or its relationship to the turbulent processes that help set it.

The classic boundary layer turbulence closure involves a 1D (vertical) representation of the down-gradient and non-local fluxes,

$$\overline{w'\phi'} = K\frac{\partial\overline{\phi}}{\partial z} + \Gamma, \tag{1.12}$$

where K is the eddy diffusivity coefficient and Γ represents any non-local effects. These terms are *included as forcing terms* in the governing equations that are solved by the GCM. Since $\overline{b}$ is resolved by the model, the effort lies in estimating K and Γ to best represent the vertical mixing processes in the upper ocean, which often depend on the turbulent velocity scales u_*, w_* and an enhancement factor $\mathcal{E}(La)$ to account for wave effects (e.g. Large et al., 1994; Li et al., 2019).

It is important to remember that parameterizations, by definition, are a simplified representation of a complex process. Many of these parameterizations emerge from natural scaling laws, that are then examined, tested and validated in high resolution numerical simulations, followed by extensive sensitivity and bias evaluations in GCMs. However, it is still impossible to capture the entire spectrum of possibilities, and will always result in some bias (even if minimal) when compared with observations. In contrast, observations of processes in the ocean surface boundary layer are scarce, and many of these theories and concepts emerge from idealized simulations, and some bias may as well be attributed to the compared observations. To conclude this point, GCMs are very useful tools that *simulate* the climate system, yet do not attempt to *resolve* every process within the climate system.

1.3.2 Large Eddy Simulations

In principal, there should be a clear scale separation between resolved and unresolved (parameterized) processes in models such as GCMs. Otherwise, the model will fall into the category of Large Eddy Simulations (LES), where large eddies are resolved and a sub-grid closure is needed to parameterize smaller eddies (Fox-Kemper et al., 2014).

The basic assumption in LES is that energy is injected at the largest scales, and cascades through an inertial range to smaller scales (Smagorinsky, 1963). In a true direct numerical simulation, the energy will eventually dissipate through molecular processes (Kolmogorov, 1941, 1991; Corrsin, 1951). In LES, an artificial scale-dependent dissipation is used to represent the transfer of energy to those smaller scales hidden below the grid scale (e.g. Sullivan et al., 1994; Tennekes and Lumley, 2018) . This is best illustrated by the energy spectra, as shown in figure 1.9, where models such as LES dissipate energy at some scale in the inertial range, and cap all smaller scale effects as subgrid effects.

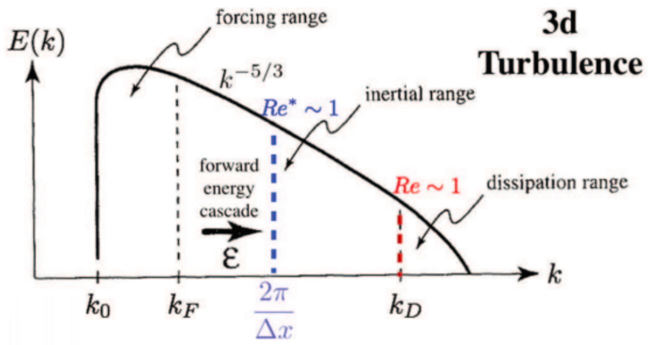

Figure 1.9: Illustration of the energy spectrum $E(k)$ and inertial range for 3D turbulence, and how models such as LES mimic dissipation below the grid scale (blue vs red vertical lines), where k is the wavenumber. Adapted from Fox-Kemper et al. (2014).

LES are popular primarily due to their high resolution and ability to resolve non-hydrostatic processes (i.e. vertical acceleration), which is necessary for processes with large vertical fluxes such as the submesoscale and boundary layer turbulence (McWilliams, 2016; Fox-Kemper et al., 2020), and for resolving their interactions with biogeochemistry (Smith et al., 2016; Taylor, 2016). As observations are limited, LES have been especially useful in advancing the basic understanding of these processes in an idealized setting and under a wide range of conditions (e.g. Grant and Belcher, 2009; Hamlington et al., 2014; Haney et al., 2015; Li and Fox-Kemper, 2017; Sullivan and McWilliams, 2018, 2019).

1.4 Outline of Thesis

This thesis is focused on studying the interaction and behavior of submesoscales and boundary layer turbulence using several theoretical and computational approaches. The main questions to be addressed here include:

- Does the presence of turbulence affect the formation of fronts? How does it change in weak and strong turbulent regimes?
- How can the interaction between submesoscales and boundary layer turbulence be described from a dynamical perspective? Can these interactions be extended to numerical methods?
- Are there any aspects of these interactions that can impact their representation on a global scale? Can we quantify these interactions and improve on existing parameterizations?

Chapter 2 introduces a theoretical framework to study the effects of turbulence on strain-induced frontogenesis. The contribution of turbulence is most significant in the PV equation, through which analytic and numerical results reveal valuable insights of the verity of ways turbulent fluxes can affect the formation of fronts.

This approach was extended in chapter 3 to a more realistic environment, by analyzing a suite of high-resolution turbulence-resolving LES, where submesoscales and boundary layer turbulence interact freely. This analysis exposes severe limitations in existing techniques to predict PV in highly turbulent regimes, and accurate diagnosis methods are presented for interpreting PV dynamics in models such as LES.

Another more targeted set of LES is analyzed in chapter 4, in which a strain-induced front is arrested by a variety of turbulent processes resulting from winds, waves, convection, and mixed layer instabilities. These interactions are quantified by estimating turbulent properties and frontal width. Results are also compared with TTW filament frontogensis LES from Sullivan and McWilliams (2018, 2019).

In chapter 5 a new scaling law is derived for frontal width that combines the theory from chapter 2 with TTW theory, and insights from chapters 3 and 4. The new scaling is utilized to modify the existing submesoscale parameterization, and is implemented in a GCM, where its impact and sensitivity is evaluated.

Finally, chapter 6 summarizes the main conclusions of this thesis and discusses future work.

Chapter 2

A Perturbation Approach to Understanding the Effects of Turbulence on Frontogenesis

This chapter is primarily drawn from work published as: Abigail S. Bodner, Baylor Fox-Kemper, Luke P. Van Roekel, James C. McWilliams, and Peter P. Sullivan. "A perturbation approach to understanding the effects of turbulence on frontogenesis." Journal of Fluid Mechanics, 883, A25. doi:10.1017/jfm.2019.804

2.1 Introduction

The classic–inviscid, adiabatic–theory (Hoskins and Bretherton, 1972; Hoskins, 1982) of frontal formation, also referred to as frontogenesis, predicts that the cross-frontal scale becomes infinitely thin in finite time. This unphysical outcome does not comply with observations, both in the ocean and atmosphere (e.g. Pollard and Regier, 1992; Bond and Fleagle, 1985). Frontogenesis occurs in the ocean mixed layer where stratification may be complex, especially including the mixed layer base and connected upper pycnocline, and where the ocean surface is subject to atmospheric forcing by winds and thermal variations, waves and wave breaking, as well as incoming and outgoing radiative energy at short and long wavelengths. Thus, a variety of mixed layer instabilities or forced turbulent mixing affects fronts, many at a scale consistent with the width of observed fronts (Sullivan and McWilliams, 2018). However, no scaling law or uniform understanding of how arrest happens over a variety of turbulent conditions exists, and present submesoscale parameterizations need such a scaling (Fox-Kemper et al., 2011).

As fronts involve both density and velocity gradients, there are potential roles for both turbulent momentum fluxes (usually simplified here as eddy viscosity) and turbulent heat fluxes (usually simplified here as eddy diffusivity). It is not well understood what kinds of turbulent fluxes may halt frontogenesis and at what scale, and what kinds enhance it and at what rate. For example, vertical mixing has been shown to be important for frontal formation (e.g. Thompson, 2000; Nagai et al., 2006), whereas horizontal mixing is thought to play a role in the arrest process (Sullivan and McWilliams, 2018). Boundary layer mixing, specifically vertical momentum flux, has also been shown to incite frontogenesis through a process called Turbulent Thermal Wind (McWilliams et al., 2015).

Much of the original theory of fronts was developed for the atmosphere, where they are critical for the understanding and prediction of weather. For example, a number of atmospheric studies (Cooper et al., 1992; Nakamura and Held, 1989; Nakamura, 1994; Xu et al., 1998) study frictional PV injection, boundary conditions, and nonlinear evolution in an evolving Eady (1949) wave, but they are simulation-based while the theoretical perturbation approach taken here distinguishes the different viscous and diffusive contributions and boundary condition effects plainly. Rotunno et al. (1994) examine differences between the perfect semi-geostrophic equations and the primitive (effectively, the hydrostatic, Boussinesq) equations, noting that both dissipative terms and non-semi-geostrophic effects contribute. However, our target application is that of fully turbulent, nonhydrostatic, Boussinesq arrest, of the kind studied using Large Eddy Simulations in Suzuki et al. (2016); Sullivan and McWilliams (2018) and subsequent studies, where nonhydrostatic boundary layer turbulence arrests frontogenesis *within* the upper ocean boundary layer. Håkansson (2002) illustrates how sensitive the atmospheric application is to the details of vertical friction and diffusivity. The oceanic application requires a still broader consideration of the kinds of turbulence that are possibly significant. While here the theory is illustrated with simple parameterizations of horizontal and vertical eddy diffusivities. Directly comparable to the past atmospheric studies, the approach presented here is readily extended to address the submesoscale (Fox-Kemper et al., 2011; Bachman et al., 2017b) and Langmuir (Li et al., 2019) turbulence found to dominate oceanic boundary layer turbulence.

In this study, we present an analytic method based on perturbation analysis to account for the effects of modest turbulent fluxes on frontal formation. While constant eddy diffusivity and viscosity are utilized as concrete examples here, the approach is easily generalized to other more realistic turbulence closures or to Large Eddy Simulation diagnostic analysis (an ongoing analysis will be reported soon). A complementary diagnostic decomposition approach has recently been proposed (McWilliams, 2017), emphasizing the attribution of causes of frontogenesis to their effects. Here an asymptotic approach is taken rather than a dynamical decomposition, illuminating different aspects of frontogenesis. In section 2.2 we review classic frontogenesis theory, present our asymptotic method in 2.2.2, and the closed equation set of the modified solution, based on potential vorticity fluxes and boundary conditions, in 2.2.3 and 2.2.4. Results are discussed in section 2.3, together with an analysis concerning localized approximations in 2.3.1 and 2.3.2. Lastly, we conclude in section 2.4, followed by an outline for future work.

2.2 Theory and Methods

The mathematical inviscid, adiabatic framework of strain-induced frontogenesis (Hoskins and Bretherton, 1972; Hoskins, 1982; Shakespeare and Taylor, 2013) describes the formation of fronts when strained by a geostrophically-balanced strain flow, such as mesoscale eddies (or synoptic weather in the atmospheric case). Shakespeare and Taylor (2013) (hereafter ST13) generalized the mathematical framework of Hoskins and Bretherton (1972) (hereafter HB72), to include fronts generated by an unbalanced flow. We follow the formulation presented in ST13 for a rotating fluid in Cartesian coordinates in an incompressible, hydrostatic, Boussinesq flow on an untilted f-plane. In the limit of HB72, the equations reduce to the semi-geostrophic equations suited for describing the early stages of strain-induced frontogenesis. Eddy viscosity and diffusivity are added as new forcing terms, but otherwise this treatment and notation follows ST13.

The velocity and pressure terms are written as:

$$\begin{cases} U = \bar{U} + u(x,z,t) = -\alpha x + u(x,z,t), \\ V = \bar{V} + v(x,z,t) = \alpha y + v(x,z,t), \\ W = 0 + w(x,z,t), \\ P = \bar{P} + p(x,z,t) = \rho_0 \left[-\alpha^2 \frac{(x^2+y^2)}{2} + f\alpha xy \right] + p(x,z,t)), \\ B = 0 + b(x,z,t). \end{cases} \tag{2.1}$$

Where $\bar{U}, \bar{V}, \bar{P}$ are the *background* balanced, horizontal large-scale deformation fields and the associated pressure field respectively. The reference density is ρ_0, f is the Coriolis parameter and u, v, w, p, b are the laminar frontogenetic velocity, pressure, and buoyancy fields. As appropriate for a mixed layer, upper ocean problem, weak background buoyancy stratification is assumed, so the background pressure field can be thought to occur primarily by sea surface height anomalies. The laminar frontogenetic fields are assumed to be nearly independent of the along-front direction y, so only $\bar{V}$ and $\bar{P}$ vary in y. The strain rate α is taken as a constant, an approximation valid when α represents much larger-scale features, such as mesoscale eddies, that do not vary over the confluence region of the submesoscale front in question. Furthermore, the semi-geostrophic approximation requires that $\alpha/f \ll 1$, which can also be described as a small Rossby number approximation. Note that y-invariance presumes that the laminar frontogenetic variables represent *laminar* perturbations to the background flow. All *turbulent* contributions will be assumed to be scale-separated from these laminar flows, and thus treated via parameterization: here eddy viscosity and diffusivity are the explicit parameterization forms carried through the analysis, although generalizations are readily handled with the same methodology. To review, the flow is decomposed as a sum of background (capital letters), laminar frontogenetic (lower case), and turbulent (parameterized so not explicitly part of u, v, w, b, p, and either frontogenetic or frontolytic) pieces.

It is useful to introduce a vector streamfunction, with a geostrophic (vertical) component[1] Φ, and an ageostrophic (along-front) component Ψ. The geostrophic streamfunction component is

---

[1] Sometimes called "velocity potential", but better understood as the vertical component of the streamfunction.

related to the pressure and horizontal geostrophic velocities by dividing into background and laminar frontogenetic contributions $\Phi = \bar{\phi} + \phi(x,z,t)$,

$$\bar{\phi} = \frac{\bar{P}}{\rho_0 f} + \alpha^2 \frac{(x^2+y^2)}{2f} = \alpha xy, \qquad \phi(x,z,t) = \frac{p(x,z,t)}{\rho_0 f}, \tag{2.2}$$

$$\frac{\partial \bar{\phi}}{\partial y} = -\bar{U}, \quad \frac{\partial \bar{\phi}}{\partial x} = \bar{V}, \qquad \frac{\partial \phi}{\partial y} = -u_g = 0, \quad \frac{\partial \phi}{\partial x} = v_g. \tag{2.3}$$

While the ageostrophic, or "overturning circulation", streamfunction component is related to the ageostrophic laminar frontogenetic velocities $\Psi = 0 + \psi(x,z,t)$,

$$\frac{\partial \psi}{\partial z} = u_a, \qquad -\frac{\partial \psi}{\partial x} = w = w_a. \tag{2.4}$$

Please note that to be consistent with ST13, we follow the left-hand-rule definition for the streamfunction, rather than the right-hand-rule as defined in HB72. Furthermore, here the term "secondary" is avoided as a description of the overturning circulation, as it is easily confused with the order of the perturbation analysis. Likewise, the phrase "laminar frontogenetic" is preferred over the more common "perturbation" velocity because it is easily confused with terms involved in the perturbation method. As in HB72, the leading-order along-front laminar frontogenetic velocities are purely geostrophic $[v \equiv v_g]$, and the cross-front laminar frontogenetic velocity is a combination of geostrophic and ageostrophic components $[u = u_g + u_a]$. The background straining velocity is given by $\bar{\phi}$ alone.

Similar to ST13, the governing equations for the 2D laminar frontogenetic response to the background flow can be expanded out from the definitions above, assuming hydrostatic, laminar flow. Here we include the novel addition of an eddy diffusive flux $F(b)$ and viscous flux $F(u), F(v)$. For now, these are written in a form amenable to accommodate most present parameterizations, including spatial variation, nonlocal fluxes, and tensor character (Large et al., 1994; Griffies, 1998; Fox-Kemper et al., 2008; Bachman et al., 2015, 2017b).

$$\frac{Du}{Dt} - fv = \alpha u - \frac{1}{\rho_0}\frac{\partial p}{\partial x} + \nabla \cdot F(u). \tag{2.5a}$$

$$\frac{Dv}{Dt} + fu = -\alpha v + \nabla \cdot F(v). \tag{2.5b}$$

$$0 = b - \frac{1}{\rho_0}\frac{\partial p}{\partial z} \tag{2.5c}$$

$$\frac{Db}{Dt} = \nabla \cdot F(b) \tag{2.5d}$$

$$\frac{\partial u}{\partial x} + \frac{\partial w}{\partial z} = 0 \tag{2.5e}$$

Where b is the buoyancy and from (2.5c) and (2.2) we have the relation:

$$\frac{\partial \phi}{\partial z} = \frac{b}{f}. \tag{2.6}$$

The material derivative is defined as:

$$\frac{D}{Dt} \equiv \frac{\partial}{\partial t} + (u + \bar{U})\frac{\partial}{\partial x} + w\frac{\partial}{\partial z} \tag{2.7}$$

Equation (2.5e) will be automatically satisfied if the streamfunctions ϕ and ψ are chosen as the prognostic variables instead of u, v, w.

For concreteness, we will assume in the following that the viscous and diffusive fluxes can be written as horizontal and vertical fluxes, assumed to be down-gradient with constant viscosities and diffusivities:

$$F(u) = \hat{x}\nu_H\frac{\partial u}{\partial x} + \hat{z}\nu_V\frac{\partial u}{\partial z}, \tag{2.8}$$

$$F(v) = \hat{x}\nu_H\frac{\partial v}{\partial x} + \hat{z}\nu_V\frac{\partial v}{\partial z}, \tag{2.9}$$

$$F(b) = \hat{x}\kappa_H\frac{\partial b}{\partial x} + \hat{z}\kappa_V\frac{\partial b}{\partial z}. \tag{2.10}$$

Consistent with assuming that the laminar fields do not vary in y, we assume that turbulent fluxes are statistically homogeneous in y and thus the $\hat{y}$ component can be ignored. One might be tempted to suggest that molecular viscosity and diffusivity might be used here, but we will soon see that asymptotic ordering demands an upper and a lower limit on Reynolds and Péclet number, so keep in mind that these terms are intended as turbulence parameterizations.

Within the mixed layer, these fluxes are assumed to be a direct result of turbulence, whereas in the very near-surface boundary they can be matched to applied wind shear (τ/ρ_0) and thermodynamic forcing (Q) via frictional and diabatic flux boundary conditions:

$$\frac{\tau_x}{\rho_0} = \hat{z}\nu_V\frac{\partial u}{\partial z} \tag{2.11a}$$

$$\frac{\tau_y}{\rho_0} = \hat{z}\nu_V\frac{\partial v}{\partial z} \tag{2.11b}$$

$$Q = \hat{z}\kappa_V\frac{\partial b}{\partial z} \tag{2.11c}$$

Penetrating solar fluxes can be accounted for, but are neglected here: all thermodynamic forcing is taken to be at the near-surface.

2.2.1 Dimensionless expressions

Following ST13, we use the following scales to make the perturbation field equations dimensionless: the horizontal and vertical buoyancy gradients ($M^2 = \frac{\partial b}{\partial y}$ and $N^2 = \frac{\partial b}{\partial z}$, which is also the buoyancy frequency squared), the horizontal and vertical length scales (L, H), and the strain and Coriolis rate parameters (α, f). The dimensionless expressions for quantities of interest are given in table 1. As in ST13, the vertical dimensionless coordinate ranges from 0 to 1, 0 being the bottom of the mixed layer and 1 the surface. The cross-frontal coordinate is centered around the initial front maximum. We focus on the semi-geostrophic limit for the background and laminar frontogenetic velocities, which implies that the along-front velocity is purely geostrophic, and it is scaled accordingly. The cross-front horizontal velocity scaling is assumed to be consistent with the conversion of potential energy being the primary source for the frontal overturning kinetic energy $bH \sim U^2$ (e.g. Suzuki et al., 2016).

The dimensionless versions of equations (2.5b) and (2.5d) are, after reorganizing:

$$\left[\frac{\partial}{\partial t} + (Ro\; u + \gamma \bar{U})\frac{\partial}{\partial x} + Ro\; w\frac{\partial}{\partial z}\right] v = -\frac{1}{Ro}u - \gamma v + \left(\frac{Ro^2}{Re_H}\right)\frac{\partial^2 v}{\partial x^2} + \left(\frac{Ro^2}{Re_V}\right)\frac{\partial^2 v}{\partial z^2} \tag{2.12a}$$

$$\left[\frac{\partial}{\partial t} + (Ro\; u + \gamma \bar{U})\frac{\partial}{\partial x} + Ro\; w\frac{\partial}{\partial z}\right] b = \left(\frac{Ro^2}{Pe_H}\right)\frac{\partial^2 b}{\partial x^2} + \left(\frac{Ro^2}{Pe_V}\right)\frac{\partial^2 b}{\partial z^2} \tag{2.12b}$$

The dimensionless relations for ϕ, ψ, b and the velocities are:

$$u = \frac{\partial \psi}{\partial z}, \qquad \frac{\partial \phi}{\partial x} = v, \qquad w = -\frac{\partial \psi}{\partial x}, \qquad \frac{\partial \phi}{\partial z} = b. \tag{2.13}$$

Based on these scalings, the error made in assuming v is geostrophic rather than using all of (2.5a) is $\mathcal{O}\left(Ro\right)$, following the approach to the semi-geostrophic equations of Hoskins (1975). This assumption implies that if the turbulent flux terms are to contribute significantly when compared to the neglected ageostrophic terms in (2.5a), at least one of Re_H, Re_v, Pe_H, or Pe_V should be smaller than Ro, which is a small parameter. Thus, at least one dissipative term must arise as an eddy parameterization, rather than through molecular values with Reynolds and Péclet much larger than one. For the purposes of this paper, qualitative inferences of the effects of turbulent fluxes are sought, but in ongoing work diagnosing Large Eddy Simulations, a comparison of the laminar frontogenetic velocities to resolved turbulence is being evaluated directly.

Following (Hoskins, 1982), we take the z derivative of equation (2.12a) and the x derivative of equation (2.12b), and using (2.13), reduce to one equation representing the instantaneous ageostrophic streamfunction governed by the strain field, geostrophic field and turbulent flux terms:

$$\begin{gathered}\frac{\partial^2 \phi}{\partial z^2}\frac{\partial^2 \psi}{\partial x^2} - 2\frac{\partial^2 \phi}{\partial z \partial x}\frac{\partial^2 \psi}{\partial x \partial z} + \left(\frac{\partial^2 \phi}{\partial x^2} + \frac{1}{Ro^2}\right)\frac{\partial^2 \psi}{\partial z^2} = \\ -\frac{2\gamma}{Ro}\frac{\partial^2 \phi}{\partial x \partial z} + \left(\frac{Ro}{Re_H}\right)\frac{\partial^4 \phi}{\partial x^3 \partial z} + \left(\frac{Ro}{Re_V}\right)\frac{\partial^4 \phi}{\partial z^3 \partial x} - \left(\frac{Ro}{Pe_H}\right)\frac{\partial^4 \phi}{\partial x^3 \partial z} - \left(\frac{Ro}{Pe_V}\right)\frac{\partial^4 \phi}{\partial z^3 \partial x}\end{gathered} \tag{2.14}$$

In ST13 and HB72 an analytic solution is obtained by assuming zero or uniform potential vorticity (PV) everywhere in the domain. This class of solutions will be the zeroth-order starting point for the perturbation analysis here.

2.2.2 Perturbation analysis

For a small term ε we use perturbation analysis to account for the effects of turbulence. We construct the zeroth-order solution to contain all the leading order laminar frontogenetic dynamics described in ST13 and HB72. Additionally, the background flow (i.e., $\bar{U}, \bar{V}$) is also part of the zeroth order,

	Symbol	Scale
Buoyancy	b	M^2L
Geostrophic velocity	v	$\frac{HM^2}{f}$
Horizontal velocity	u	$\sqrt{M^2LH}$
Vertical velocity	w	$\sqrt{\frac{M^2H^3}{L}}$
Time	t	$\frac{1}{f}$
Background mean velocity	$\bar{U}$	αL
Rossby number	Ro	$\sqrt{\frac{M^2H}{f^2L}}$
Froude number	Fr	$\sqrt{\frac{M^2L}{N^2H}}$
Deformation ratio	γ	$\frac{\alpha}{f}$
Geostrophic streamfunction component	ϕ	M^2LH/f
Ageostrophic streamfunction component	ψ	$\sqrt{M^2LH^3}$
Horizontal turbulent Reynolds number (for horizontal eddy viscosity)	Re_H	$\frac{vL}{\nu}$
Vertical turbulent Reynolds number (for vertical eddy viscosity)	Re_V	$\frac{vH}{\nu}$
Horizontal turbulent Péclet number (for horizontal eddy diffusivity)	Pe_H	$\frac{vL}{\kappa}$
Vertical turbulent Péclet number (for vertical eddy diffusivity)	Pe_V	$\frac{vH}{\kappa}$

Table 2.1: Dimensionless expressions for quantities of interest following ST13 framework in the semi-geostrophic limit, which implies that the along-front velocity is purely geostrophic.

so for the inviscid, adiabatic, zeroth-order limit a zero PV valid solution exists.

$$\begin{cases} U = \bar{U} + u = \varepsilon^0(\bar{U} + u^0) + \varepsilon^1 u^1 + \mathcal{O}\left(\varepsilon^2\right), \\ V = \bar{V} + v = \varepsilon^0(\bar{V} + v^0) + \varepsilon^1 v^1 + \mathcal{O}\left(\varepsilon^2\right), \\ W = w = \varepsilon^0 w^0 + \varepsilon^1 w^1 + \mathcal{O}\left(\varepsilon^2\right), \\ \Phi = \bar{\phi} + \phi = \varepsilon^0(\bar{\phi} + \phi^0) + \varepsilon^1 \phi^1 + \mathcal{O}\left(\varepsilon^2\right), \\ b = \varepsilon^0 b^0 + \varepsilon^1 b^1 + \mathcal{O}\left(\varepsilon^2\right). \end{cases} \tag{2.15}$$

At the first order, the effects of turbulence (2.8)–(2.10) and the associated surface forcing (2.11a)–(2.11c) on the laminar frontogenetic flow will be isolated and examined.

We will now study individually horizontal and vertical viscosity and diffusivity. For each case the small perturbation parameter ε is defined by:

$$\begin{cases} \varepsilon_{HV} = \frac{Ro}{Re_H} = Ek_H : & \text{Horizontal viscosity (HV)}, \\ \varepsilon_{VV} = \frac{Ro}{Re_V} = Ek_V : & \text{Vertical viscosity (VV)}, \\ \varepsilon_{HD} = \frac{Ro}{Pe_H} = \frac{Ek_H}{Pr_H} : & \text{Horizontal diffusivity (HD)}, \\ \varepsilon_{VD} = \frac{Ro}{Pe_V} = \frac{Ek_V}{Pr_V} : & \text{Vertical diffusivity (VD)}. \end{cases} \tag{2.16}$$

Where $Ek_H = \frac{Ro}{Re_H} = \frac{\nu}{fL^2}$, $Ek_V = \frac{Ro}{Re_V} = \frac{\nu}{fH^2}$ and $Pr_H = \frac{\nu_H}{\kappa_H}$, $\quad Pr_V = \frac{\nu_V}{\kappa_V}$ are the horizontal and vertical Ekman and Prandtl numbers. For small Ekman numbers and $\mathcal{O}\left(1\right)$ Prandtl numbers, these terms are all expected to be small. However, depending on the details of the type of turbulence approximated, it may be expected that they may not be the same size. We proceed asymptotically by assuming they are all small and of equal order, and then after the asymptotic perturbation expansion we can choose to individually neglect them.

Using the eddy viscosity and diffusivity parameterizations (2.8)–(2.10), these small parameters appear before the terms of highest differential order. Hence, there will always be some small "frictional sublayer" scale on which they are not small and they enlarge near the boundaries to satisfy the boundary conditions (2.11a)–(2.11c). A similarity or asymptotic matching solution may thus be more appropriate as an asymptotic approach in order to "magnify" the sublayer region and examine potentially leading order impacts outside the sublayer. However, other parameterizations of turbulence differ in differential order, e.g., a Newtonian drag as used in some eddy-damping boundary layer schemes (e.g., Parsons, 1969; Fox-Kemper and Ferrari, 2009) or Newtonian cooling as sometimes used in air-sea damping schemes (e.g., Dijkstra and Molemaker, 1997), or linear drag as through parameterized Ekman layer pumping (Twigg and Bannon, 1998; Boutle et al., 2015). Thus, the detailed asymptotics within the frictional boundary layer will be specific to the differential form of the parameterization–here eddy viscosity and diffusivity, but not generically those forms. Furthermore, the true ocean boundary has a wavy-frothy-bubbly sublayer for which there exist numerical approaches but not analytic ones. For these reasons, the effects of eddy viscosity and diffusivity in a specific frictional sublayer analysis are not the focus of this study. Rather, it is the intention here that the singular perturbation implied by neglecting these highest-derivative-order terms (i.e.

as $\varepsilon \to 0$) be equivalent to the traditional solution of the classic inviscid, adiabatic frontogenesis theory, and may be used as a guide to later analyze realistic turbulent frontal simulations.

Thus, (2.14) is solved assuming an ansatz of regular perturbation analysis, and that the solution exists outside the frictional sublayer, affected only at first order by the turbulence there. We insert (2.15) above into equation (2.14) found in the previous section and separate by order of ε.

Zeroth order: inviscid, adiabatic

This order is the traditional frontogenesis regime, as studied by HB72 and ST13. Typically, a zero or uniform potential vorticity is assumed to arrive at a simpler solution. We will preserve this assumption for the zeroth order, but it will be revisited in the context of turbulent fluxes and potential vorticity anomalies and injection below. Additionally, to ensure consistency with the limitation of the Hoskins (1975) semi-geostrophic assumption and asymptotic theory, we confine this analysis to $\gamma = \mathcal{O}\left(Ro^2\right)$ and $Ro < \varepsilon < \mathcal{O}\left(Ro^{-2}\right)$. However, as both Ro and ε must be small parameters, a tighter bound actually applies: $Ro < \varepsilon < 1$. The zeroth order equation for the streamfunction, equation (2.14), equivalent to HB72, is:

$$\frac{\partial^2 \phi^0}{\partial z^2}\frac{\partial^2 \psi^0}{\partial x^2} - 2\frac{\partial^2 \phi^0}{\partial z \partial x}\frac{\partial^2 \psi^0}{\partial x \partial z} + \left(\frac{\partial^2 \phi^0}{\partial x^2} + \frac{1}{Ro^2}\right)\frac{\partial^2 \psi^0}{\partial z^2} = -\frac{2\gamma}{Ro^2}\frac{\partial^2 \phi^0}{\partial x \partial z}. \tag{2.17}$$

ST13 introduced a new coordinate system, similar to the geostrophic momentum coordinate in HB72:

$$X = e^{\alpha t}\left(x + \frac{v^0}{f}\right), \quad Z = z, \quad T = t. \tag{2.18}$$

This X coordinate is conserved for any value α and is referred to as the “generalized momentum coordinate”. A similar expression for the vertical coordinate is desirable when the scale of gradient sharpening in the vertical is comparable to the horizontal (e.g. McWilliams et al., 2009). Here we assume frontal sharpening is dominated by the horizontal strain field, and thus strictly use the horizontal form of the generalized momentum coordinate. Note that since ST13 solve the inviscid non-diffusive case, this coordinate system is associated with the zeroth order solution.

The dimensionless form of this coordinate system is:

$$X = e^{\gamma T}\left(x + Ro\, v^0\right), \quad Z = z, \quad T = t. \tag{2.19}$$

In this new coordinate system, which tracks the Lagrangian displacements in x, the dimensionless material derivative reduces to

$$\frac{D}{Dt} = \frac{\partial}{\partial T} + Ro\, w^0 \frac{\partial}{\partial Z}. \tag{2.20}$$

And the dimensionless Jacobian for this transformation is:

$$J = e^{\gamma T}\left(1 - e^{\gamma T} Ro \frac{\partial v^0}{\partial X}\right)^{-1}. \tag{2.21}$$

The solution for all the zeroth order terms, assuming zero PV, are given in ST13. The buoyancy field is defined as:

$$b^0(X, Z, T) = B_0(X) + Fr^{-2} Z + \Delta b^0(X, Z, T) \tag{2.22}$$

Where $B_0(X)$ is the initial imposed buoyancy field as a function of X, chosen to be $B_0(X) = \frac{1}{2}\mathrm{erf}\left(\frac{X}{\sqrt{2}}\right)$. For simplicity, we take the HB72 scenario (for which $v = v_g$) and the corresponding solution from ST13 is the following:

$$u^0 = -e^{\gamma T} Ro\ B_0'(X)\ (Ro\ w + (2Z-1)\gamma) \tag{2.23a}$$

$$w^0 = Ro\ \gamma\ B_0''(X) Z(Z-1) e^{2\gamma T} \left(1 - Ro\ e^{\gamma T} \frac{\partial v^0}{\partial X}\right)^{-1} \tag{2.23b}$$

$$v^0 = e^{\gamma T} Ro\ B_0'(X)\ \left(Z - \frac{1}{2}\right) \tag{2.23c}$$

Later it will be useful when using the zeroth order velocities to convert to coordinate system (2.19) where the velocities are written explicitly and have relatively simple expressions.

The criterion in ST13 for frontal singularity is that the transformation no longer holds, i.e the inverse of the Jacobian vanishes $\left(J^{-1} = e^{-\gamma T} - Ro\ \frac{\partial v^0}{\partial X}\right)$. This happens when $B_0'''(X_f) = 0$. For the HB72 case, the singularity forms at the critical time of $t = 19.8$, and the Eulerian location of this singularity is found to be:

$$x_f = Ro \frac{1}{\sqrt{2\beta}} \left(X_f\ \beta + B_0'(X_f)\right) \tag{2.24}$$

Where $\beta = -B_0''(X) > 0$. Note that we expect x_f to appear in two locations: one at the surface, cold-side corner of the front in the mixed layer (x_{fs}) and the other at the base, warm-side corner of the front (x_{fb}).

Figure 2.1 illustrates the dynamical formation (in real space) of frontogenesis with the buoyancy field, and the emergence of the along-front velocity and cross-frontal overturning streamfunction. We follow ST13 in choosing $Ro = 0.4$, $\gamma = 0.1$ as an example for the HB72 case. As frontogenesis progresses, the imposed strain enhances the buoyancy gradient, which, through thermal wind balance, strengthens the along-front shear (figure 2.2). A useful diagnostic measure for frontal tendency is the Lagrangian evolution of the horizontal buoyancy gradient $T_b^0 = \frac{D}{Dt}\frac{1}{2}\left(\frac{\partial b^0}{\partial x}\right)^2$ (Hoskins, 1982; McWilliams et al., 2015), shown in figure 2.3. Positive frontal tendency coincides with the largest buoyancy gradient, and in late frontogenesis a negative frontal tendency adjacent to the front maximum, contributes to the sharpening the front, eventually leading to singularity. An ageostrophic overturning circulation appears in the cross-frontal plane, attempting to re-stratify the front, further contributing to frontogenesis (figure 2.4). The positive overturning streamfunction in figure 2.4 indicates a counterclockwise overturning, which is in the direction to move buoyant water over dense and stratify the frontal region. However, as the frontal region is somewhat wider than the overturning, the upper left (upper, cold-side) and lower right (lower, warm-side) buoyancy gradients are concentrated more than other regions of the front. Illustrated in the right panels of figures 2.2 and 2.4, as frontogensis progresses, the ageostrophic streamfunction strengthens and narrows, and the along-front velocity gets pinched to two points at the top, cold-side corner and bottom, warm-side corner of the frontal region of the mixed layer, and the buoyancy gradient strengthens and isopycnals come closer together and tilt–especially in these two corners, consistent with the locations of maximum frontal tendency (figure 2.3). The zeroth order solution continues to strengthen

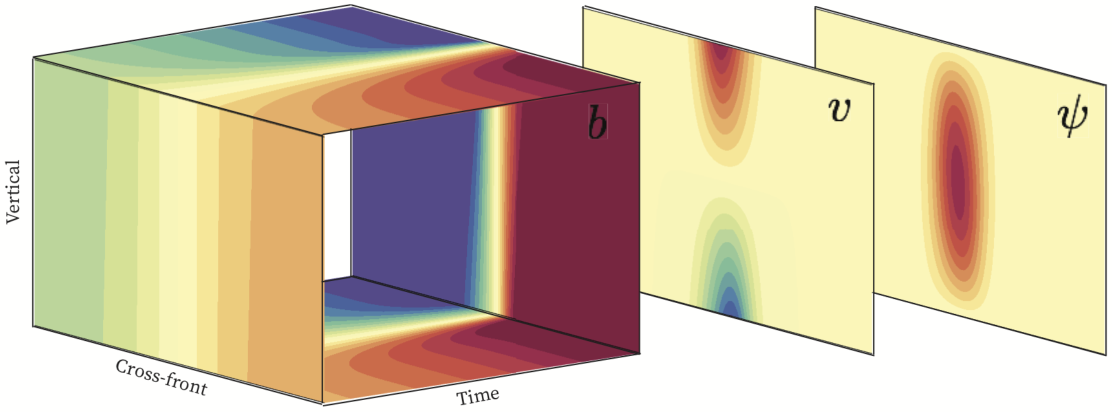

Figure 2.1: Frontal formation of the dimensionless zeroth order buoyancy field (left), together with the cross-frontal planes showing the along-front velocity v (middle), and overturning streamfunction ψ (right). The cross-frontal, vertical and time axis correspond to the dimensionless x, z and t axis respectively.

and narrow, and becomes singular at these two points within a finite time. In the following section, the first order solution effects on this process are shown.

First order: turbulent fluxes

The first order equation for the streamfunction given by equation (2.14) will be slightly different, depending on the type of forcing at hand:

$$\begin{aligned}&\frac{\partial^2\phi^0}{\partial z^2}\frac{\partial^2\psi^1}{\partial x^2}-2\frac{\partial^2\phi^0}{\partial z\partial x}\frac{\partial^2\psi^1}{\partial x\partial z}+\left(\frac{\partial^2\phi^0}{\partial x^2}+\frac{1}{Ro^2}\right)\frac{\partial^2\psi^1}{\partial z^2}=\\&-\frac{\partial^2\phi^1}{\partial x^2}\frac{\partial^2\psi^0}{\partial z^2}+2\frac{\partial^2\phi^1}{\partial z\partial x}\frac{\partial^2\psi^0}{\partial x\partial z}-\frac{\partial^2\phi^1}{\partial z^2}\frac{\partial^2\psi^0}{\partial x^2}-\frac{2\gamma}{Ro}\frac{\partial^2\phi^1}{\partial x\partial z}+\mathcal{F}(\phi^0),\end{aligned} \tag{2.25}$$

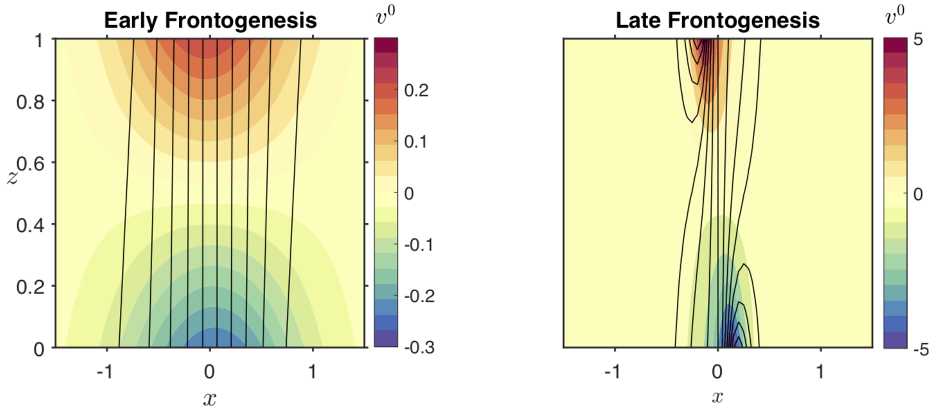

Figure 2.2: Cross-frontal profiles of the zeroth order along-front velocity v^0 (shading) at two times defined as early frontogenesis ($t = 5$, left) and late frontogenesis ($t = 18$, right). Note the different colorbar axes. Superimposed in black contours is the buoyancy field, with intervals of 0.1 in non-dimensional units. Note the singularity developing during late frontogenesis. x and z are the dimensionless cross-frontal and vertical axes, respectively, in real space.

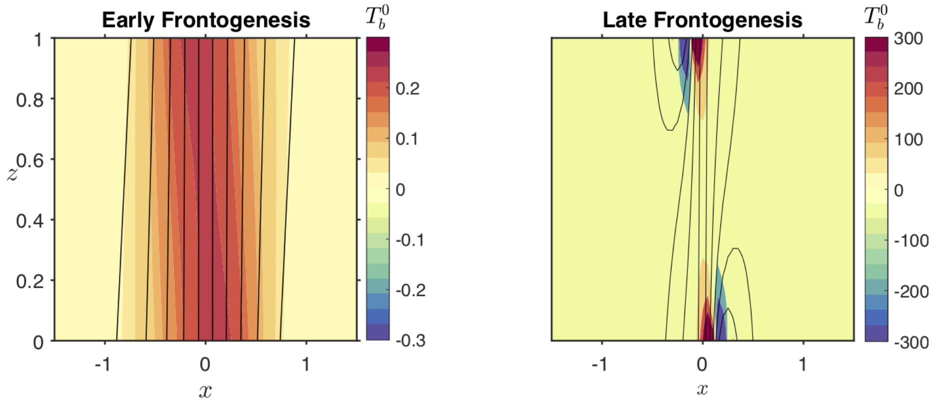

Figure 2.3: Contours show buoyancy as in figure 2.2, shading shows the zeroth order frontal tendency T_b^0.

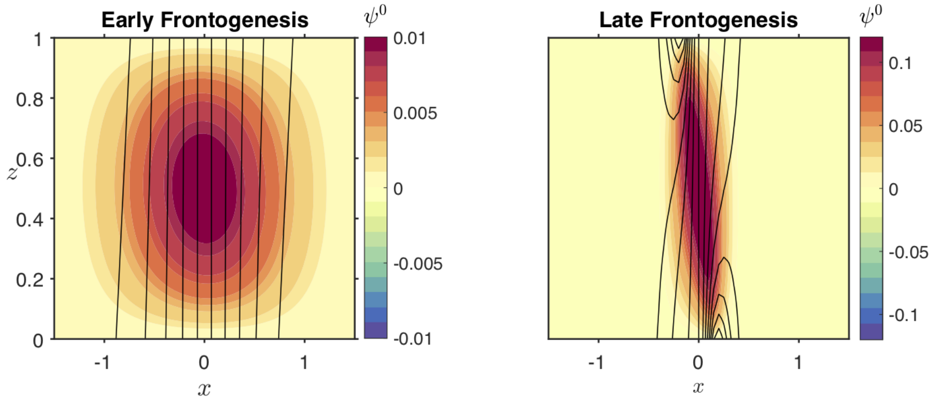

Figure 2.4: Contours show buoyancy as in figure 2.2, shading shows the zeroth order streamfunction ψ^0.

The different turbulent flux parameterizations arise as:

$$\mathcal{F}(\phi^0) = \begin{cases} \frac{\partial^4 \phi^0}{\partial x^3 \partial z} & \text{(HV)} \\ \\ \frac{\partial^4 \phi^0}{\partial z^3 \partial x} & \text{(VV)} \\ \\ -\frac{\partial^4 \phi^0}{\partial x^3 \partial z} & \text{(HD)} \\ \\ -\frac{\partial^4 \phi^0}{\partial z^3 \partial x} & \text{(VD)} \end{cases} \tag{2.26}$$

In our theoretical framework both surface boundary conditions and interior turbulent fluxes enter at the first order and are functions of zeroth order terms. Thus (2.25) is an inhomogeneous (with turbulent flux divergences as forcing), 2nd-order, linear (from perturbation method), partial differential equation (PDE) which is coupled for the unknown overturning and vertical streamfunction perturbations ψ^1, ϕ^1 with non-constant coefficients, which are known functions of the zeroth order solution. In addition to the limitations on ε and Ro, this analysis is also restricted to times of early frontal formation, when $\psi^1 < \mathcal{O}(1/\varepsilon)$ and the PDE (2.25) remains elliptic.

Note that the viscous terms are of opposite sign to the diffusive terms, but horizontal diffusivity and viscosity have the same operator, as do vertical diffusivity and viscosity. Although (2.26) suggests that diffusivity and viscosity may have opposite effects on frontal formation, an additional equation and boundary conditions that differ between viscosity and diffusivity are required in order to obtain the full uncoupled solutions for the first order overturning and geostrophic streamfunction ϕ^1, ψ^1.

2.2.3 Potential Vorticity

Potential vorticity (PV), specifically Ertel PV, is a conserved quantity fundamental to geophysical fluid dynamics, and has historically been immensely useful in understanding oceanic and atmospheric dynamics (e.g. Rhines, 1986; Hoskins, 1991; Gill, 1982; Pedlosky et al., 1987; Salmon, 1998; Kurgansky and Pisnichenko, 2000). PV is defined from the absolute vorticity ($\omega = f\mathbf{k} + \nabla \times \mathbf{u}$) and buoyancy gradient:

$$q = (f\mathbf{k} + \nabla \times \mathbf{u}) \cdot \nabla b \tag{2.27}$$

Where $\mathbf{u} = (\bar{U} + u, \bar{V} + v, w)$ are the background and laminar velocity fields. Note that turbulent velocities are not included in this definition of PV, which is important in the interpretation of the eddy parameterizations. Since the zeroth order PV is assumed to be zero as in traditional frontogenesis theory, any PV in the perturbation system is associated with the first order and is a result of turbulent fluxes and boundary injection. The dimensionless first order PV is:

$$\frac{q^1}{Ro^2} = \frac{\partial v^1}{\partial x}\frac{\partial b^0}{\partial z} - 2\frac{\partial v^0}{\partial z}\frac{\partial b^1}{\partial x} + \left(\frac{1}{Ro^2} + \frac{\partial v^0}{\partial x}\right)\frac{\partial b^1}{\partial z}. \tag{2.28}$$

Or in terms of ϕ^1,

$$\frac{q^1}{Ro^2} = \frac{\partial b^0}{\partial z}\frac{\partial^2 \phi^1}{\partial x^2} - 2\frac{\partial v^0}{\partial z}\frac{\partial^2 \phi^1}{\partial x \partial z} + \left(\frac{1}{Ro^2} + \frac{\partial v^0}{\partial x}\right)\frac{\partial^2 \phi^1}{\partial z^2}. \tag{2.29}$$

The PV equation (2.29), like (2.25), is also an inhomogeneous (the forcing here is the non-zero PV), 2nd-order, linear elliptic PDE for ϕ^1 with non-constant coefficients which are functions of the zeroth order solution. As the zeroth order solution is already known, then if given the strength of q^1, equation (2.29) can be inverted to find ϕ^1. From this, ψ^1 can be found using (2.25). So, if q^1 is known, then (2.29) and (2.25) are two coupled, linear PDEs in the unknowns ϕ^1, ψ^1.

The evolution of PV (which is just q^1 as the zeroth order has zero PV) is determined by frictional and diabatic forcing through the so-called J-equation, and can be written in terms of an advective term, a frictional flux term and diabatic flux term (Haynes and McIntyre, 1987; Marshall and Nurser, 1992; Thomas, 2005; Benthuysen and Thomas, 2012; Wenegrat et al., 2018):

$$\frac{\partial q}{\partial t} = -\mathbf{u}\cdot\nabla q + (\nabla \times \mathbf{D}_u)\cdot\nabla b + \omega\cdot(\nabla D_b) \tag{2.30}$$

Where $\mathbf{D}_u$ and D_b are the frictional and diabatic flux divergences.

Since the zeroth-order PV is uniform, the total PV equation reduces to the evolution of the first order PV.

$$\frac{\partial q^1}{\partial t} = -\mathbf{u}^0\cdot\nabla q^1 + (\nabla \times \mathbf{D}_u^1)\cdot\nabla b^0 + \omega^0\cdot(\nabla D_b^1) \tag{2.31}$$

In the asymptotic framework, the frictional and diabatic fluxes appear only in the first order and are functions only of known zeroth-order factors:

$$\mathbf{D}_u^1 = \nabla\cdot F(v^0) \tag{2.32a}$$

$$D_b^1 = \nabla\cdot F(b^0) \tag{2.32b}$$

Likewise, the advection of the first-order PV is only carried by the known zeroth-order velocity: $(\bar{U} + u^0, \bar{V} + v^0, w^0)$.

The non-dimensional form of this equation is:

$$\frac{\partial q^1}{\partial t} = -\left[(Ro\ u^0 + \gamma\bar{U})\frac{\partial}{\partial x} + Ro\ w^0\frac{\partial}{\partial z}\right]q^1 + \mathcal{D}(v^0, b^0) \tag{2.33}$$

Where the frictional and diabatic flux effects on PV have been collected into

$$\mathcal{D}(v^0, b^0) = \begin{cases} \frac{\partial b^0}{\partial x}\frac{\partial^3 v^0}{\partial x^2 \partial z} - \frac{\partial b^0}{\partial z}\frac{\partial^3 v^0}{\partial x^3} & \text{(HV)} \\ \frac{\partial b^0}{\partial x}\frac{\partial^3 v^0}{\partial z^3} - \frac{\partial b^0}{\partial z}\frac{\partial^3 v^0}{\partial z^2 \partial x} & \text{(VV)} \\ \frac{\partial v^0}{\partial z}\frac{\partial^3 b^0}{\partial x^3} - \frac{\partial v^0}{\partial x}\frac{\partial^3 b^0}{\partial x^2 \partial z} & \text{(HD)} \\ \frac{\partial v^0}{\partial z}\frac{\partial^3 b^0}{\partial z^2 \partial x} - \frac{\partial v^0}{\partial x}\frac{\partial^3 b^0}{\partial z^3} & \text{(VD)} \end{cases} \tag{2.34}$$

2.2.4 Boundary Conditions and First-Order Solution Procedure

To evaluate first-order solutions for each of the frictional forcing cases, equation (2.33) is integrated in time using the zeroth order terms from (2.22) and (2.23a)-(2.23c). During integration, the first-order PV is calculated, advected, and accumulated.

The first order solution is next found, for every forcing case, by solving equations (2.25) and (2.29) using the PV resulting from (2.33). By integrating equations (2.5a) and (2.5d), the vertical boundary conditions are solved at each time. Explicitly, the vertical boundary conditions are calculated by following the evolution of the first order buoyancy and cross-frontal velocity at the top and bottom boundaries, for each forcing case:

$$b^1 = \frac{\partial \phi^1}{\partial z}, \qquad b^1\bigg|_{z=0,1} = \int_0^t \left[-\mathbf{u}^0 \cdot \nabla b^1 - \mathbf{u}^1 \cdot \nabla b^0 + \nabla \cdot F(b^0)\right]\bigg|_{z=0,1} \mathrm{d}t \tag{2.35a}$$

$$u^1 = \frac{\partial \psi^1}{\partial z}, \qquad u^1\bigg|_{z=0,1} = \int_0^t \left[-\mathbf{u}^0 \cdot \nabla u^1 - \mathbf{u}^1 \cdot \nabla u^0 + \gamma u^1 + \nabla \cdot F(u^0)\right]\bigg|_{z=0,1} \mathrm{d}t \tag{2.35b}$$

$$q^1\bigg|_{z=0,1} = \left[Ro^2 \frac{\partial b^0}{\partial z}\frac{\partial^2 \phi^1}{\partial x^2} - 2Ro^2 \frac{\partial v^0}{\partial z}\frac{\partial^2 \phi^1}{\partial x \partial z} + \left(1 + Ro^2 \frac{\partial v^0}{\partial x}\right)\frac{\partial^2 \phi^1}{\partial z^2}\right]\bigg|_{z=0,1} \tag{2.35c}$$

It is important to note that the fluxes producing PV in the preceding equations are surface turbulent fluxes associated with frontal formation. At this time we do not consider external surface forcing, such as wind stress, which has been shown to contribute additional interior PV (Thomas and Ferrari, 2008).

The horizontal boundary conditions assume the laminar frontogenetic fields vanish in the horizontal, far from the front. Explicitly,

$$v^1\bigg|_{x\to\pm\infty} = \frac{\partial \phi^1}{\partial x}\bigg|_{x\to\pm\infty} = 0 \tag{2.36a}$$

$$u^1\bigg|_{x\to\pm\infty} = \frac{\partial \psi^1}{\partial z}\bigg|_{x\to\pm\infty} = 0 \tag{2.36b}$$

$$q^1\bigg|_{x\to\pm\infty} = 0 \tag{2.36c}$$

The initial conditions for all first order terms, which include the PV, ψ^1 and ϕ^1 are zero, assuming turbulence and secondary circulations are negligible at $t = 0$ when the front is weak. More details on the numerical methods used to illustrate the results in the following section can be found in Appendix B.

2.3 Results

To quantify the effects turbulent fluxes may have on frontal formation, the first order frontal tendency is a useful start, evaluated by:

$$T_b^1 = \frac{D}{Dt_0}\left(\frac{\partial b^0}{\partial x}\frac{\partial b^1}{\partial x}\right) + \frac{D}{Dt_1}\frac{1}{2}\left(\frac{\partial b^0}{\partial x}\right)^2, \tag{2.37}$$

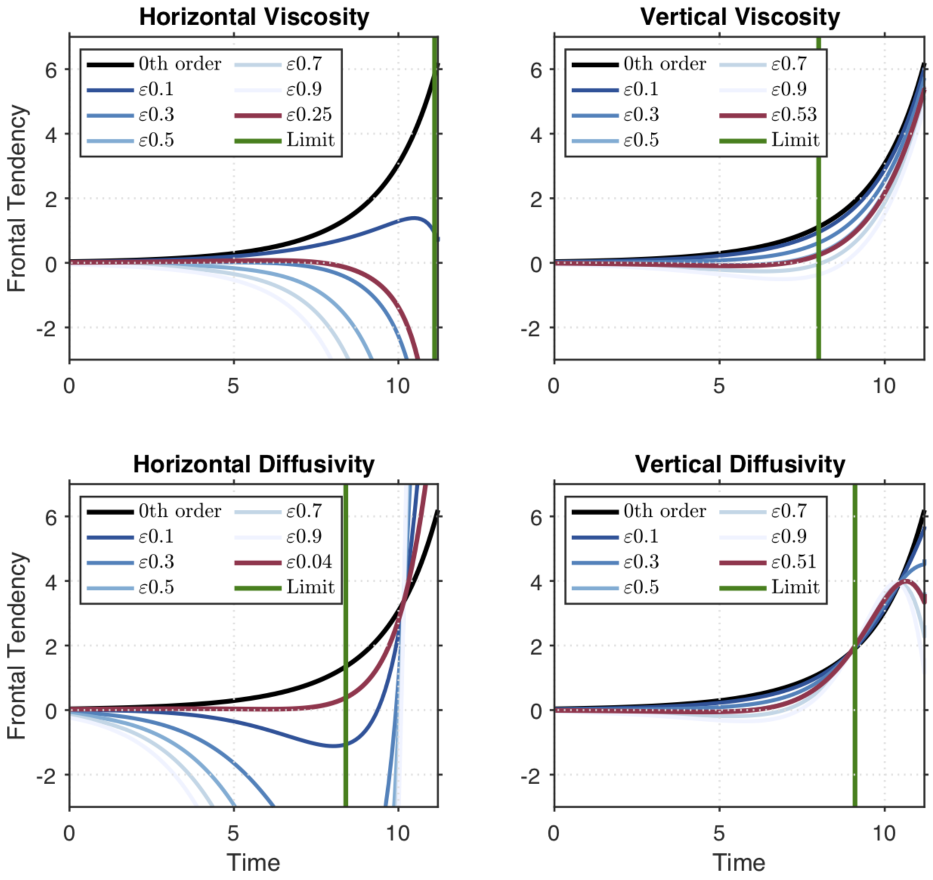

Figure 2.5: Total frontal tendency $T_b = T_b^0 + \varepsilon T_b^1$ for each of the forcing cases, over a variety of ε (shades of blue), evaluated at the surface, where the zeroth order frontal tendency maximum (black) becomes infinitely strong. For each forcing case, the maroon line represents the ε for which $T_b = 0$. The green vertical line represents the time where the limit of the perturbation approach is reached for each forcing case: horizontal viscosity ($t = 11.1$), vertical viscosity ($t = 8$), horizontal diffusivity ($t = 8.4$), vertical diffusivity ($t = 9.1$).

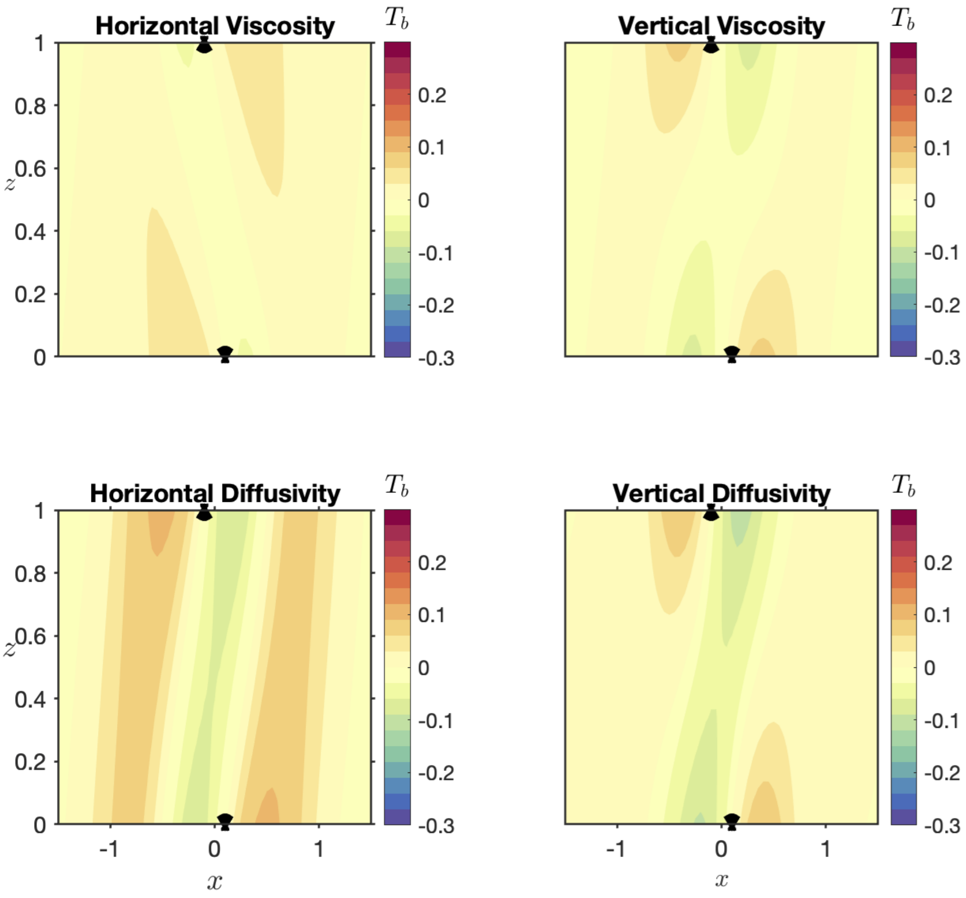

Figure 2.6: Cross-frontal plane of the total frontal tendency $T_b = T_b^0 + \varepsilon T_b^1$ during early frontogenesis ($t = 5$) with the appropriate arrest ε for each forcing case: horizontal viscosity ($\varepsilon = 0.25$), vertical viscosity ($\varepsilon = 0.53$), horizontal diffusivity ($\varepsilon = 0.04$), vertical diffusivity ($\varepsilon = 0.51$). Black ticks indicate the location of the maximum zeroth order frontal tendency corresponding to that measured in figure 2.5 and for the sense of where the front is strongest.

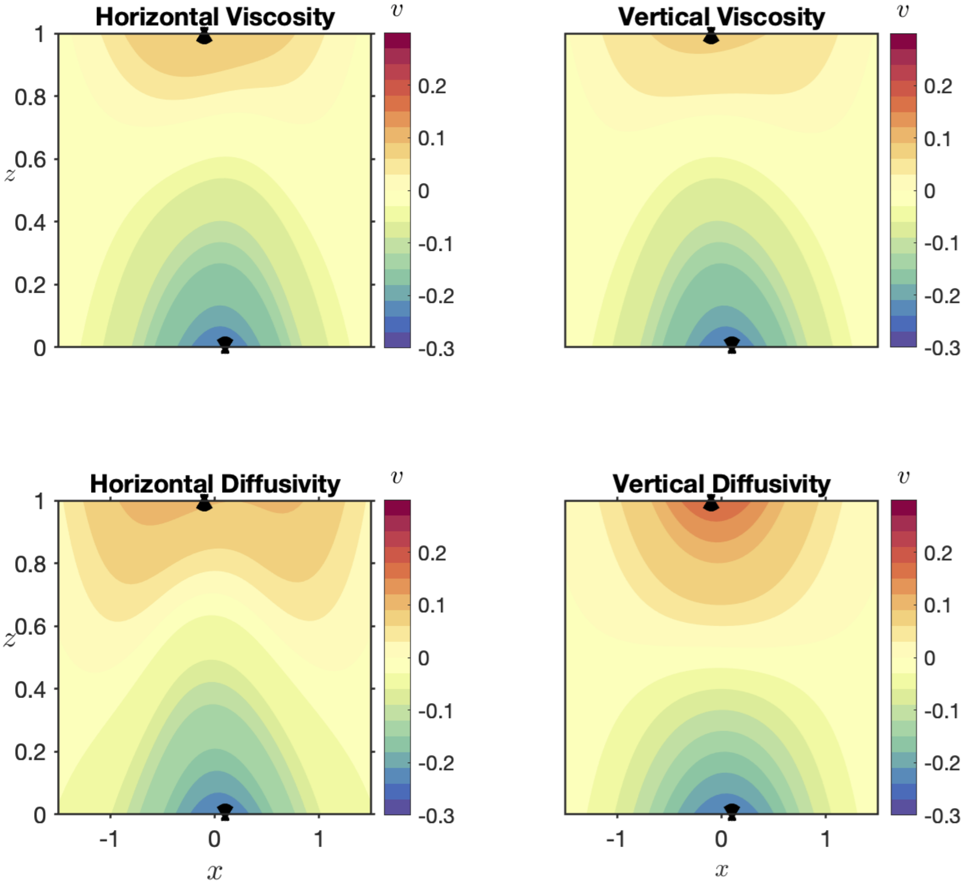

Figure 2.7: Same as in figure 2.6 for the total along-front velocity $v = v^0 + \varepsilon v^1$.

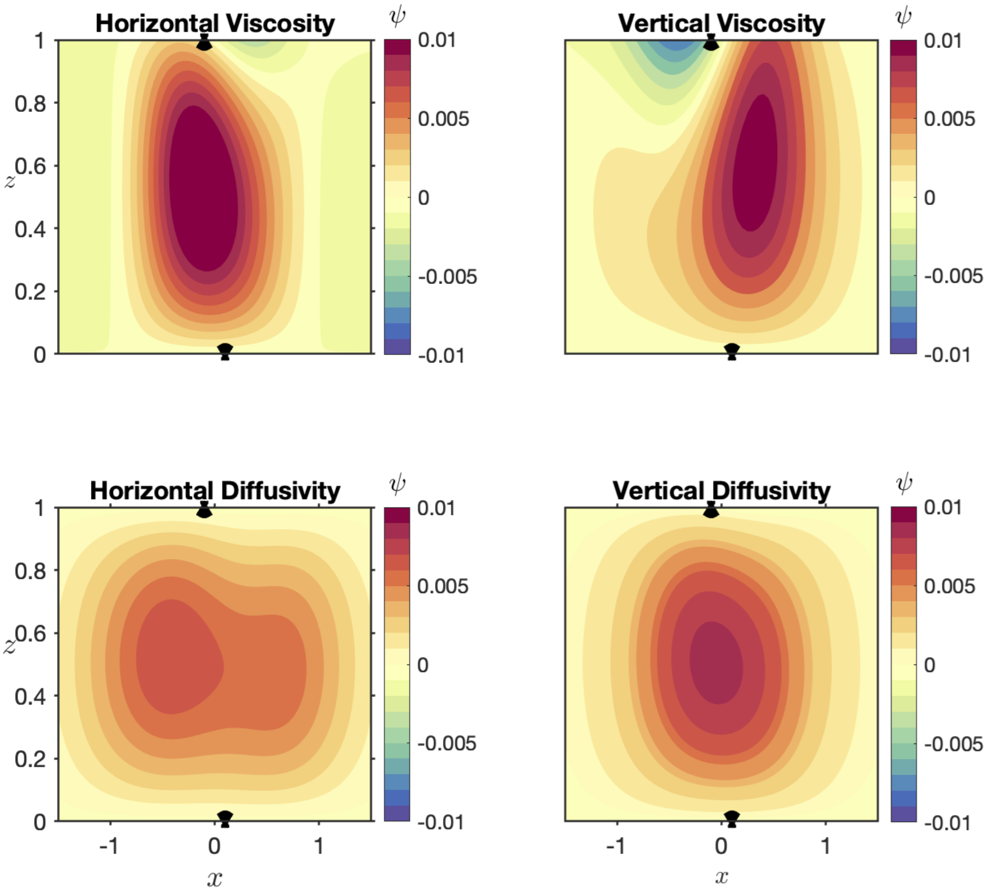

Figure 2.8: Same as in figure 2.6 for the total streamfunction $\psi = \psi^0 + \varepsilon\psi^1$.

where subscripts on the Lagrangian derivative operator indicate the order of the advecting velocities. The total frontal tendency, i.e. $T_b = T_b^0 + \varepsilon T_b^1$, is sensitive to the choice of ε and the turbulent forcing at hand. Presented in figure 2.5 are the total frontal tendencies for each of the forcing cases, over a variety of ε (shades of blue), evaluated at the surface, where the zeroth order frontal tendency maximum (black) becomes infinitely strong. For each forcing case, the maroon line represents the ε for which $T_b = 0$. This is a major result of this study, as it implies that there exists a choice of parameters, for each turbulent forcing case, that is able to temporarily resist the strengthening of the front, i.e. lead to an arrest. It is important to note that ε is different for every forcing case, as well as the length of time for which it is able to sustain an arrest. However, the limitations of the perturbation theory are highlighted by the erratic behaviour of the solution at later times, a reminder that this theory is valid only for early frontal formation while higher-order corrections remain insignificant. In Figure 2.5, a green vertical line is used to indicate when higher order terms begin to rival leading order terms–i.e., an estimate of the breakdown time of the perturbation method.

A closer look reveals that horizontal turbulent forcing cases share similar properties, as do the vertical. Both horizontal viscosity and diffusivity show a linear response in epsilon towards a weakening of the total frontal tendency, i.e. as ε increases, T_b becomes more negative. Additionally, the ε which enables an arrest is relatively small, only $\varepsilon = 0.25$ in the horizontal viscosity case and $\varepsilon = 0.04$ in the horizontal diffusivity case. Vertical viscosity and diffusivity also can reduce the rate at which frontal tendency grows, however larger values of ε are required to reach negative frontal tendency. During late frontogenesis (near time 10), larger values of vertical diffusivity enhance the rate of frontogenesis over the zeroth-order solution, with larger ε leading to faster frontal tendency (although this effect occurs after perturbation theory is estimated to remain formally accurate). To make early time frontal tendency negative, very large values of ε are needed with the vertical operators. Furthermore, larger values of the arrest ε are found in the vertical cases, where $\varepsilon = 0.53$ in the vertical viscosity case and $\varepsilon = 0.51$ in the vertical diffusivity case. Indeed, $Ro = 0.4 < \varepsilon < 1$ is required by the asymptotics, so much larger ε are not accessible consistently. By contrast, very small values of ε optimize arrest (as simulated in the perturbation theory) in the horizontal viscosity ($\varepsilon \approx 0.25$) and especially diffusivity ($\varepsilon \approx 0.04$) cases. The perturbation assumption of $Ro \sim \varepsilon$ does not apply for such small ε values, and these specific values are unlikely to be accurate (Barcilon, 1998; Bender and Orszag, 2013). However, even a small amount of horizontal diffusivity surely affects frontogenesis strongly. In practice, even small amounts of horizontal numerical viscosity and diffusivity will have a large impact on frontogenesis, consistent with other findings (see discussion in McWilliams et al., 2009). Because numerical stability requires (horizontal) diffusivity and viscosity to scale with (horizontal) resolution, much higher horizontal resolution is required to properly capture frontogenesis numerically than one would naively expect based on assumed balances such as $Ro \sim \varepsilon$. Thus, recent oceanic large eddy simulations of frontogenesis (e.g., Suzuki et al., 2016; Sullivan and McWilliams, 2018) are likely addressing a novel regime where horizontal fluxes may contribute unlike in coarser hydrostatic models. Likewise, the results here that vertical turbulent fluxes approach leading order to contribute to arrest–or even become frontogenetic as in the vertical diffusivity near time 10, is likewise consistent with recent numerical analyses of the frontogenetic Turbulent Thermal Wind effects.

To better understand the underlying dynamics of the possible arrest mechanism for each forcing case, we next examine the cross-frontal planes of the total frontal tendency ($T_b = T_b^0 + \varepsilon T_b^1$, figure 2.6), along-front velocity ($v = v^0 + \varepsilon v^1$, figure 2.7) and streamfunction ($\psi = \psi^0 + \varepsilon \psi^1$, figure 2.8). All figures are displayed at non-dimensional time $t = 5$, and with the appropriate arrest ε for each forcing case found in figure 2.5. Black ticks indicate the location of maximum zeroth order frontal tendency corresponding to that measured in figure 2.5, and for the sense of where the front is strongest. All forcing cases exhibit zero total frontal tendency at the location of the zeroth order maximum (figure 2.6), which is expected by choosing the arrest ε for each case. A demonstration of the arrest is also apparent, for each forcing case, in the spreading and weakening of the along-front velocity at the surface (figure 2.7).

However, in the zeroth-order solution illustrated in figures 2.2-2.4, the overturning streamfunction tended to focus the buoyancy gradients in two corner points, consistent with the locations of maximum frontal tendency, and where eventually frontal singularities first develop. In the perturbation solutions combined to first order in figures 2.6-2.8, the behaviour at these points is different depending on which turbulent forcing case is examined.

1. Horizontal viscosity: the frontal tendency (figure 2.6) exhibits weak negative and positive signals adjacent to the zeroth order frontal maximum, of opposite orientation to figure 2.3 during late frontogenesis. Furthermore, a negative streamfunction (figure 2.8) appears near the surface, right of the region of maximum zeroth order frontal tendency, directing fluid and gradients away from the front maximum. This supports the findings in figure 2.5, that the contribution of horizontal viscosity at the first order tends to weaken the front.

2. Vertical viscosity: although weaker in magnitude, the frontal tendency (figure 2.6) in this case is of similar orientation to the front maximum as in figure 2.3 during late frontogenesis. Here, a negative streamfunction (figure 2.8) appears near the surface as well, but in opposite configuration with respect to the front maximum when compared to the horizontal viscosity case, thus directing fluid and gradients to concentrate toward the region of maximum zeroth order frontal tendency. Although, at time $t = 5$ the total frontal tendency is near zero, the flow indicates that vertical viscosity at the first order tends to enhance frontogenesis, consistent with results from previous studies.

3. Horizontal diffusivity: the along-front velocity is relatively wide spread in figure 2.7 as compared with the other cases, even for a relatively small value of ε. The streamfunction (figure 2.8) similarly is widespread, however the streamfunction reverses sign for increased ε, directly opposing the zeroth order streamfunction (not shown). Interestingly, the frontal tendency in this case (figure 2.5) does not resemble that of the horizontal viscosity case. Rather, it is of the same configuration as vertical viscosity and diffusivity, which may explain the acceleration

found in figure 2.5 approaching the perturbation limit at time $t = 8.4$. However, horizontal diffusivity in figure 2.5 displays a weakening even for very small values of ε and thus, we conclude that horizontal diffusivity, similar to horizontal viscosity, has mostly frontolytic characteristics.

4. Vertical diffusivity: similar to the vertical viscosity case, the frontal tendency here (figure 2.6) exhibits the same configuration as in figure 2.3. However, the streamfunction (figure 2.8) displays a weak wider shape in the interior, yet is more concentrated near the surface. The streamfunction shape does not reveal much intuition regarding the effects of vertical viscosity on the flow field. For smaller ε, the streamfunction magnitude is stronger, and for larger ε more concentrated at the surface (not shown). Figure 2.5 shows that as the perturbation limit is approached at time $t = 9.1$, the total frontal tendency *for all values of* ε accelerate and focus at the zeroth order value. The time this occurs is likely sensitive to parameters such as Ro and γ. We conclude that vertical diffusivity, similar to vertical viscosity, is frontogenetic based on the frontal tendency, yet not easily understood from the streamfunction flow field.

To summarize, the first-order solution is distinguished from the zeroth-order solution in two ways, by the computed interior PV and through the altered boundary conditions that arise at first order. The first order solutions examined in this section are surprisingly complex in comparison to the simple reversal of signs in (2.34)–the solutions are not just mirror images because the surface boundary conditions for momentum and buoyancy are not simply related even though the field equations are. It is now natural to ask whether the solution is fully dependent on both or whether either the interior PV or the surface conditions dominates over the other.

2.3.1 Surface Quasi-Geostrophy versus Interior Quasi-Geostrophy

In the mixed layer, surface quasi-geostrophic (SQG) dynamics (Lapeyre and Klein, 2006; Lapeyre et al., 2006) sometimes dominate over interior quasi-geostrophic (IQG) dynamics forced by anomalies in ocean interior PV (Klein et al., 2011), also called Charney (1971) QG dynamics (Bretherton, 1966; Capet et al., 2008b; Stamper et al., 2018). IQG has been shown in some simulations to enhance frontogenesis over SQG-only upper ocean cases (Capet et al., 2016) can nonetheless exhibit mesoscale strain-induced frontogenesis to some degree which is enhanced by submesoscales (Callies et al., 2016). The relative contributions of the SQG system are more easily detected by remote sensing (e.g., LaCasce and Mahadevan, 2006; Chavanne and Klein, 2016; LaCasce and Wang, 2015).

In an SQG system, surface buoyancy anomalies are used to generate an active boundary condition, while the interior PV is taken to be uniform and inert (Blumen, 1978). The full flow field is obtained by using the PV invertibility principle (Hoskins et al., 1985), with the active buoyancy field providing the boundary conditions for the inversion. In the IQG system, the boundary conditions are simplified by neglecting buoyancy anomalies and flow dynamics are assumed to be driven solely by interior quasi-geostrophic PV anomalies (QGPV). Two interesting byproducts of the perturbation analysis framework are that the first order Ertel PV, as ordinarily used in traditional frontogenesis literature, is locally equivalent to QGPV at that order, and that the impact of the first-order solution can be uniquely and completely decomposed into SQG effects and IQG effects (figures 2.9 and 2.10). Turbulent closures affect surface buoyancy quite differently from interior PV, so: are the effects on frontal formation by interior PV comparable to surface turbulent fluxes?

The PV in (2.29), together with the buoyancy boundary condition on ϕ in (2.35a) and (2.36a), can thus be constructed from a combination of the interior QGPV, which in isolation drives the IQG system, and added delta functions based on surface buoyancy to replace the buoyancy boundary condition (Bretherton, 1966), which in isolation drive the SQG system (more details in Appendix B). The surface delta boundary conditions are explicitly calculated by following the evolution of the first order buoyancy and cross-frontal velocity at the surface, for each forcing case:

$$b^1 = \frac{\partial \phi^1}{\partial z}, \qquad b^1 = \int_0^t \left[-\mathbf{u}^0 \cdot \nabla b^1 - \mathbf{u}^1 \cdot \nabla b^0 + \nabla \cdot F(b^0)\right] \delta(z-0)\ \mathrm{d}t \tag{2.38a}$$

$$u^1 = \frac{\partial \psi^1}{\partial z}, \qquad u^1 = \int_0^t \left[-\mathbf{u}^0 \cdot \nabla u^1 - \mathbf{u}^1 \cdot \nabla u^0 + \gamma u^1 + \nabla \cdot F(u^0)\right] \delta(z-0)\ \mathrm{d}t \tag{2.38b}$$

A delta function for the bottom boundary condition is used as well, although this has little effect on the end result. These are essentially identical to the full first order boundary conditions (2.35a)-(2.35b).

Figures 2.9 and 2.10 show the cross-frontal planes of the first order along-front velocity v^1 and streamfunction ψ^1 at time t=5 for all forcing cases, calculated from the full system (a)-(d), the IQG system (e)-(h), the SQG system (i)-(l), and their sum (q)-(t). Subfigures (m)-(p) will be discussed in the following subsection.

To obtain the along-front velocity, we solve a linear PDE in ϕ^1, and thus expect the sum of the SQG and IQG systems to be similar to that of the full system. For all forcing cases, the full and SQG systems in figure 2.9 are characterized by negative velocity, centered at the surface and decreasing with depth. On the other hand, the IQG system shows a significantly weaker velocity, with a dipole shape (or double dipole in the vertical cases). Hence, for the along-front velocity, representing the geostrophic field, the SQG system appears to capture most elements of the complete solution.

Unlike the equation for ϕ^1, the streamfunction ψ^1 has a forcing term that cannot be easily attributed to SQG or IQG dynamics, as it is governed by zeroth order terms. For illustration purposes, we divide this forcing term into surface and interior domains (more details in Appendix B), and solve for the SQG and IQG systems separately. The first order streamfunction exhibits different behaviour for each forcing case in figure 2.10. The full solution for the horizontal and vertical viscosity cases is focused near the surface, whereas in the horizontal and vertical diffusivity cases the streamfunction is centered in the interior. Furthermore, unlike figure 2.9, the IQG system is comparable in magnitude in the horizontal cases, yet weaker in the vertical cases. The sum of the SQG and IQG systems is very similar to the complete system in all cases, however only in the horizontal viscosity case does the IQG system contribute significantly in the interior.

Thus, given surface turbulent fluxes, the first order correction of the along-front velocity and geostrophic potential can be found to a good approximation merely from surface conditions, using SQG theory in this classic strain-induced frontogenesis case. The overturning streamfunction and ageostrophic field reveal a more complex dependency on interior fluxes, which by affecting interior PV, may be important for a complete solution below the surface. This implies that parameterizations that affect the surface buoyancy will have a larger impact on frontal structure than those that affect interior PV or the rate of PV injection.

2.3.2 Point Source Surface Quasi-Geostrophy

In the SQG framework, we followed Bretherton (1966), and used delta functions in z to replace the surface buoyancy boundary conditions. The success of this approach in capturing much of the full frontogenesis impacts on along-front velocity highlights the importance of surface buoyancy gradients. We now examine a further simplification of buoyancy that is severely focused in the horizontal direction as well to see how much of the effect is retained. During frontogenesis, the buoyancy has a sharp, and sharpening, gradient over the frontal domain. As the buoyancy singularity is approached, the cross-frontal buoyancy gradient $\frac{\partial b^1}{\partial x}$ may be approximated by a delta function in the cross-frontal direction, corresponding to the location of maximum frontal tendency, and buoyancy gradients elsewhere being neglected. Using this assumption, a simplified boundary condition for the geostrophic potential ϕ^1 is a Heaviside function in x and a delta function in z:

$$\phi^1(z=0) = \begin{cases} \phi^1_{max}\delta(z-0) & x > x_{fb} \\ \phi^1_{min}\delta(z-0) & x < x_{fb} \end{cases} \tag{2.39a}$$

$$\phi^1(z=1) = \begin{cases} \phi^1_{max}\delta(z-1) & x > x_{fs} \\ \phi^1_{min}\delta(z-1) & x < x_{fs} \end{cases} \tag{2.39b}$$

The cross-frontal points where the buoyancy gradient is localized are denoted by x_{fs}, x_{fb} which represent the location of the front nose at the surface (fs) and bottom (fb) of the mixed layer respectively.

The motivation for considering such simplifications is Green's functions theory, as a full flow field solution exists for ϕ^1 and ψ^1 even if only a point source buoyancy gradient is prescribed (e.g. Harnik and Heifetz, 2007). An example analytic procedure for finding the first-order solution to (2.25), using delta function approximations and Green's function theory, is given in Appendix C.

Figures 2.9 and 2.10 (m)-(p) show results for the SQG systems with *point source* surface conditions. In all forcing cases, the along-front velocity and streamfunction are very similar to the full SQG system solutions in (i)-(l), especially near the surface.

In conclusion, the SQG geostrophic potential, which contributes most of the along-front velocity, can be reconstructed by *surface conditions highly localized near the front maximum.* From a parameterization or numerics development perspective, it is the method of regularizing–or keeping finite–the buoyancy gradient very near the maximum gradient surface expression of the front that will dominate the fidelity of a strain-induced frontal simulation, rather than turbulent fluxes elsewhere or the broad-scale injection of PV.

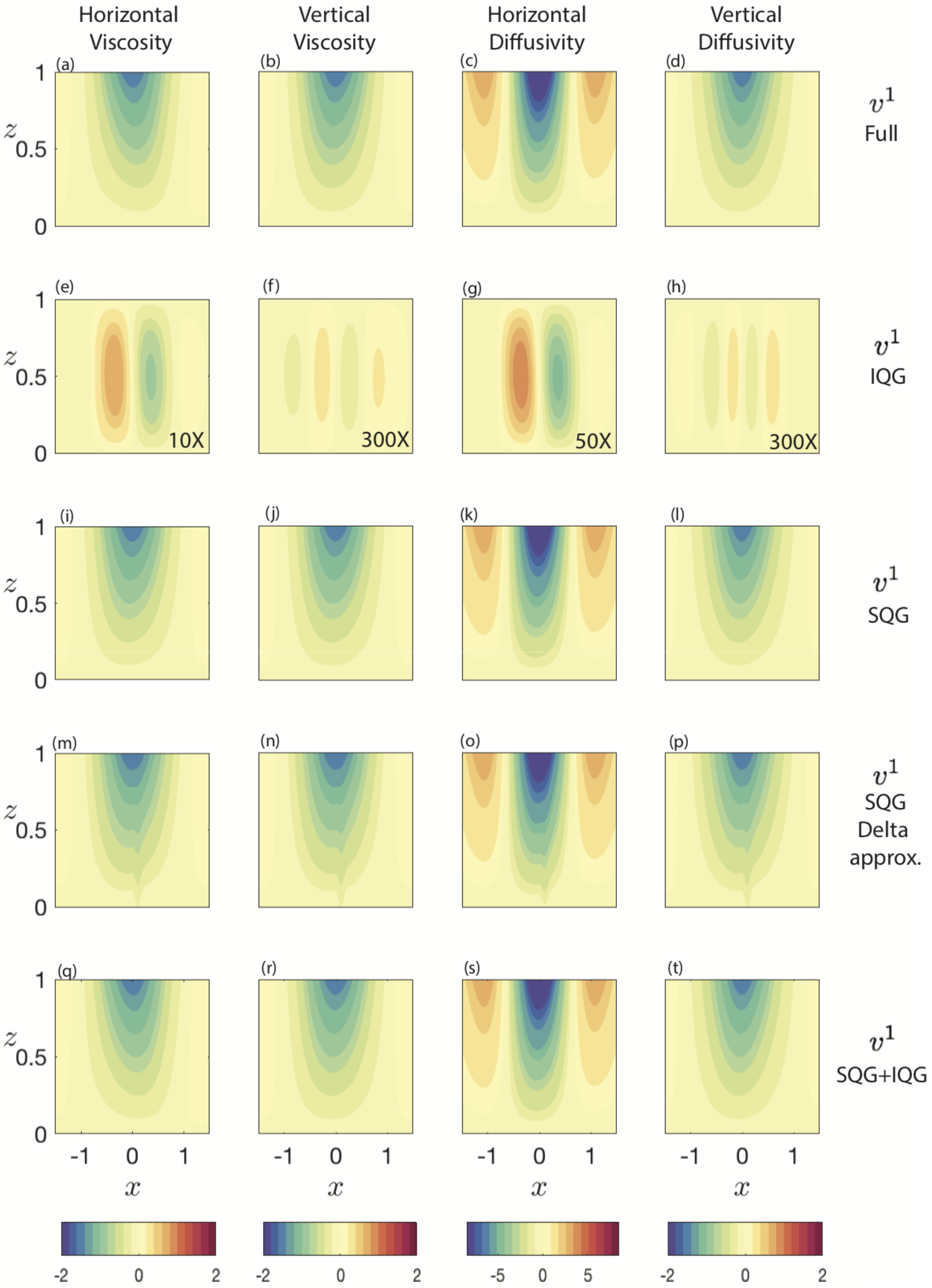

Figure 2.9: Cross-frontal planes of the first order along-front velocity v^1 at time t=5 for all forcing cases, calculated from the full system (a)-(d), the IQG system (e)-(h), the SQG system (i)-(l), the SQG system with a point source approximation (m)-(p), and the sum of the SQG and IQG systems(q)-(t). Note that for plotting purposes the IQG system is multiplied by a constant.

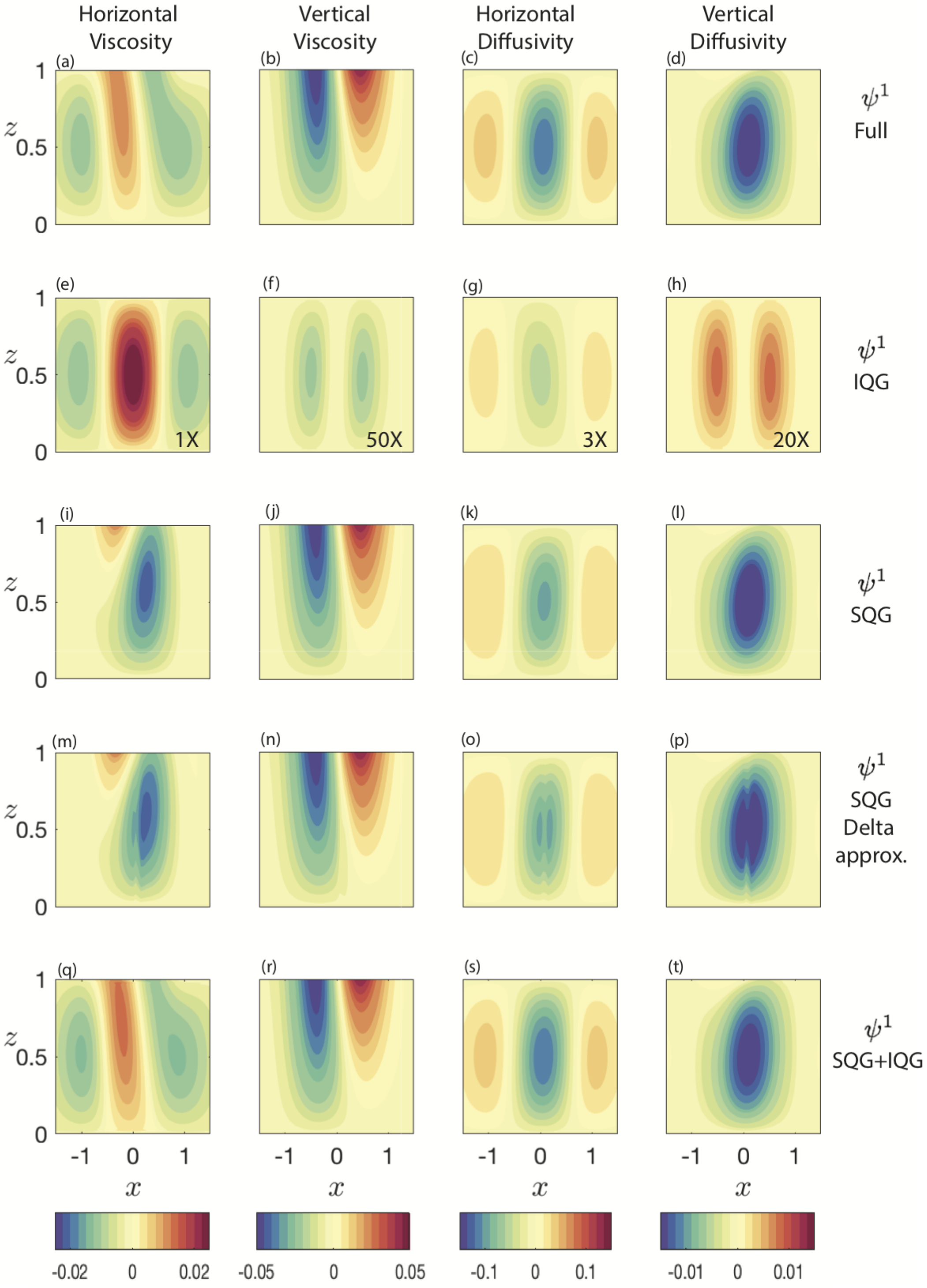

Figure 2.10: Same as in figure 2.9 for the first order streamfunction ψ^1. Note that for plotting purposes also here the IQG system is multiplied by a constant.

2.4 Summary and Discussion

In this study, an asymptotic approach estimates the leading order correction of turbulent fluxes to classic theory for strain-induced frontogenesis. The system described by classic theory may capture the leading order dynamics, but it is shown here that turbulent fluxes are likely a key secondary component missing in aligning theory with observations and model simulations, especially in the ocean where submesoscale fronts typically coexist with boundary layer turbulence, but also in lower-level atmospheric fronts. Here the effects of turbulent surface and interior fluxes of buoyancy and PV were isolated and examined.

The uncoupled first-order solutions for the along-front geostrophic velocity and ageostrophic overturning streamfunction are obtained by inverting the modified semi-geostrophic frontogenesis equation together with the first non vanishing-order PV equation. By differentiating between horizontal and vertical eddy viscosity and diffusivity which, in reality, might be associated with parameterizations of mixed layer instabilities, boundary layer turbulence or numerical artifacts as simulated fronts approach singularity, an early understanding of the different impacts of these dissipative operators on fronts is gained. It is found that horizontal viscosity and diffusivity readily act to weaken the front, and thus are key to understanding frontal arrest, consistent with the arresting role of horizontal shear instabilities found by Sullivan and McWilliams (2018). Vertical viscosity and diffusivity, by contrast, act only to slow strengthening of the front at first, and later vertical diffusivity accelerates frontogenesis resembling Turbulent Thermal Wind theory (McWilliams et al., 2015; McWilliams, 2017; Crowe and Taylor, 2018).

As the full first-order solution depends on both turbulent boundary conditions and injected interior PV, a decomposition of the results into surface quasi-geostrophic (SQG) and interior quasi-geostrophic (IQG) subsystems isolates the contributions to the full solution. In most forcing cases, it is found that SQG dynamics are able to capture most of the along-front velocity and overturning streamfunction features, whereas IQG dynamics have a small contribution. The point source forcing indicates that only a small surface region near the front is needed. In the case of horizontal viscosity, the ageostrophic overturning circulation is only fully reconstructed by including both the SQG and IQG systems. Due to the nature of frontal dynamics, features tend to be localized where the front is strongest. By considering only a point source buoyancy gradient boundary condition, a good approximation to the full SQG response for both the along-front geostrophic velocity and overturning ageostrophic streamfunction was obtained. In a recent paper, Wenegrat et al. (2018) show that boundary layer turbulence can generate a source of PV at the surface, similar in magnitude to PV fluxes from wind and surface buoyancy fluxes (Thomas, 2005). It is presently unclear whether our conclusions for the SQG and IQG systems hold true in the presence of strong surface forcing such as downfront wind forcing, or realistic boundary layer turbulence. However, the same perturbation methods can be used while including wind forcing in (2.13), and many of the LES being analyzed include winds.

Furthermore, the asymptotic method presented in this study is derived from the semi-geostrophic equations presented in HB72, implying that the Rossby number is smaller than 1. However, in the submesoscale regime, both inertial and rotational forces are important and so the Rossby number is $Ro \sim 1$ (e.g. McWilliams, 2016). Additionally, semi-geostrophic theory has been shown to be inconsistent with $Ro \sim 1$ (Barkan et al., 2019) and curved fronts (Gent et al., 1994). The expansion parameter ε is taken to be constant, however the realistic form is highly uncertain as it represents parameterized effects of turbulent fluxes in the submesoscale regime. The modified theory presented here merely acts as a framework to study the effects of turbulent fluxes during early frontal formation, while the semi-geostrophic assumptions and asymptotic approximation still hold.

It is intended that this framework be utilized in concert with submesoscale simulations with more realistic turbulence parameterizations or resolved turbulence to highlight important regions or aspects of such simulations. At present, Large Eddy Simulations (Moeng, 1984; McWilliams et al., 1997) are able to resolve the submesoscale dynamics and boundary layer turbulence that motivates this theory. An examination of simulations similar to those studied in Hamlington et al. (2014); Smith et al. (2016); Suzuki et al. (2016) but including strain-inducing eddies are ongoing. In all runs, a confluent region produces strong frontogenesis, but the cross-frontal scale halts at a finite width. The eventual target is finding quantitative predictions for frontal width, strength, and persistence in the presence of realistic turbulent fluxes.

Acknowledgements

This research was made possible in part by a grant from The Gulf of Mexico Research Initiative and in part by NSF EPSCoR RI-CAIM (NSF 1655221). No data were used in producing this manuscript. Much of this work was developed during the Kavli Institute for Theoretical Physics, as part of the Planetary Boundary Layers in Atmospheres, Oceans, and Ice on Earth and Moons program, supported by the National Science Foundation under Grant No. NSF PHY17-48958. We would especially like to thank Gregory Chini and Shafer Smith for their insights concerning asymptotics and boundary layers turbulence. Furthermore, we would like to thank Nobuhiro Suzuki, Aakash Sane, Qing Li, Joseph Skitka, Brodie Pearson and Jenna Pearson for fruitful conversations throughout this study.

Chapter 3

A Breakdown in Potential Vorticity Estimation Delineates the Submesoscale-to-Turbulence Boundary

This chapter is primarily drawn from work published as: Abigail S. Bodner and Baylor Fox-Kemper. "A Breakdown in Potential Vorticity Estimation Delineates the Submesoscale-to-Turbulence Boundary in Large Eddy Simulations." Journal of Advances in Modeling Earth Systems 12.10 (2020): e2020MS002049.

3.1 Introduction

Potential Vorticity (PV), the fundamental correlation between vorticity and stratification, is a key active variable of quasigeostrophic theory, and one of the most widely used properties in large-scale oceanic and atmospheric dynamics (Pedlosky, 2013). PV is conserved via material advection for adiabatic and inviscid flows (or nearly so for atmospheric and oceanic flows), is invertible in quasigeostrophic flows to govern the subinertial flow, is the critical parameter governing stability in symmetric instability (Hoskins, 1974), and even when not materially conserved the evolution of PV is tractable via *frictional and diabatic* fluxes (Haynes and McIntyre, 1987; Marshall and Nurser, 1992; Thomas, 2005). The central question to be addressed here is: *Does 3D turbulence, when partly resolved in a Large Eddy Simulation, count as material advection of PV or a frictional and diabatic process?*

Different flow scales exhibit different properties. Large and slow flows tend to be governed by strong stratification and planetary rotation, however as smaller, faster scales are approached – from mesoscale to submesoscale to 3D turbulence – inertial forces come to dominate as the flow passes through isotropic turbulent properties before finally reaching the Kolmogorov (1941, 1991) and Batchelor (1959) scales, where molecular motions are sufficiently dominant as to restrain the production of variance through (continuum) turbulence. As model capacities are increasing, multiscale simulations now have the ability to partially resolve 3D turbulence together with larger scale flows. Since PV is strongly dependent on stratification and rotation, the question arises as to its robustness in an isotropic turbulent regime–where all mean vector quantities tend to zero because no particular directions or vectors are allowed in isotropic statistics–and mean buoyancy gradients (i.e., stratification) and mean vorticity (i.e., rotation) are zero or at best ephemeral and only partially resolved in Large Eddy Simulations (LES).

In this study we demonstrate that PV holds different scale-dependent statistics as a 3D turbulent regime is approached, than those expected from larger mesoscale and submesoscale dynamics, and this statistical transition may effectively delineate the small-scale boundary of the submesoscale: the smallest scale of classic geophysical fluid dynamics where influences of rotation and stratification are strong. Hamlington et al. (2014) define the small-scale end of the submesoscale as the scale where nonhydrostatic effects become dominant, which is a definition based on the asymptotic behavior of reduced equations consistent with the change in PV statistics, but the latter delineation is easily detected as a statistical and dynamical marker of this scale.

Section 3.2 introduces the theory and behavior of PV in the 3D turbulence regime using spectral analysis, and the implications of these results are presented in section 3.3 using multiscale simulations which span the submesoscale and 3D turbulence regime. The consequences of Reynolds averaging are discussed in section 3.4, and this analysis is implemented in section 3.5 to obtain an accurate PV–along with its governing equations consistent with the needs of large-scale PV analysis–by prefiltering the velocity and buoyancy fields. Discussion and conclusions are presented in section 3.6.

3.2 Potential Vorticity and Spectral Analysis

Ertel Potential Vorticity, q, in nonhydrostatic, Boussinesq approximation fluids, is usefully defined by the product of the buoyancy gradient and total vorticity (Pedlosky, 2013):

$$q = (\mathbf{f} + \boldsymbol{\omega}) \cdot \nabla b. \tag{3.1}$$

The relative velocity vector is $\mathbf{u}$, $\boldsymbol{\omega} = \nabla \times \mathbf{u}$ is the relative vorticity and $\mathbf{f}$ is the planetary vorticity, b is the buoyancy anomaly. The buoyancy is related to the potential temperature field θ by $b = -g\alpha\theta$ under a constant salinity linear equation of state in oceanic flows or an anelastic approximation in atmospheric conditions, g being gravity acceleration and α the thermal expansion coefficient. This simplified form is that of the model studied here, although a more complete discussion of PV–including methods for treating nonlinear equations of state, background stratification gradients, and non-aligned rotation and gravity vectors–can be found in Fox-Kemper (2018).

The key utility of PV comes from two aspects: its material conservation and the invertibility of PV and buoyancy to find the balanced velocity fields (McWilliams, 2006). At the mesoscale, subinertial unbalanced motions are weak, so geostrophic turbulence (Rhines, 1979) is governed entirely by the advection of PV and buoyancy by the turbulent flows, which in turn then provide the turbulent flows from the PV and buoyancy distributions through invertibility. Large-scale PV dynamics are key to understanding the general circulation and stratification (Haynes and McIntyre, 1987; Marshall and Nurser, 1992). At the submeoscales the Rossby number is larger, so unbalanced motions such as internal waves are strong enough to have unbalanced velocities that rival the balanced velocity field and may nonlinearly interact (Bakas and Farrell, 2009), so submesoscale turbulence is a complicated combination of wavelike and geophysical turbulence (McWilliams, 2016). Yet, many submesoscale features such as fronts, filaments, and eddies have strongly constrained motions where PV dynamics remain relevant (Thomas and Lee, 2005; Thomas, 2005; Thomas and Ferrari, 2008; Thomas, 2008; Wenegrat and McPhaden, 2016; Siegelman, 2020). Obviously, even as models resolve smaller and smaller phenomena in larger and larger domains, retaining a dynamical equivalent of submesoscale, mesoscale, and large-scale PV is critical to linking these theoretical analyses to interpretation of the latest model.

A second important theoretical result regarding PV is that its material conservation in inviscid, adiabatic flow extends to the full Navier-Stokes equations if diffusion and viscous transfers are correctly interpreted (Pedlosky, 2013; Haynes and McIntyre, 1987; Bachman et al., 2017a). Of course, in realistic geophysical contexts stratification and rotation effects are leading order on the length and time scale of tens of kilometers and days and are negligibly small at scales approaching the (Kolmogorov, 1941, 1991) and (Batchelor, 1959) time and length scales. Thus, these scales are typified by order one Reynolds and Péclét numbers, but huge Rossby and Froude numbers, thus most of the motions at these dissipative scales is unbalanced and not predictable by PV inversion.

The variance of PV can be studied by examining the power spectral density of its components across scales (following Frisch, 1995, among others). Namely, key quantities to examine are the isotropized (i.e., integrated over all angles spanning a horizontal plane and including the polar coordinate metric factor) power spectral density of kinetic energy E, potential energy B, enstrophy Z and potential enstrophy Q, which upon integration over wavenumber magnitude are proportional to the horizontal area-integrated-and-squared velocity, buoyancy, buoyancy gradient, vorticity, potential vorticity, and tracer concentration respectively. It should be noted that here horizontal power spectra and scales are emphasized, as most of the flows under consideration are tranversely isotropic–i.e., strongly anisotropic in the vertical versus horizontal directions but approximately isotropic in the horizontal over all scales, due to the vertical alignment of gravity and planetary rotation (for simplicity the simulations are on a non-tilted f-plane). Only at the smallest resolved scales does a 3D isotropic spectrum become useful. The spectral density of a passive tracer C with concentration c will also be discussed later. For brevity, the power spectral density will just be referred to as the spectrum below, and their relation to area-integrated variance can be written out explicitly as:

$$\int_0^\infty E(\kappa)\mathrm{d}\kappa \propto \int \mathbf{u}\cdot\mathbf{u}\ \mathrm{d}x\mathrm{d}y, \tag{3.2a}$$

$$\int_0^\infty B(\kappa)\ \mathrm{d}\kappa \propto \int b^2\mathrm{d}x\mathrm{d}y, \tag{3.2b}$$

$$\int_0^\infty G(\kappa)\ \mathrm{d}\kappa = \int_0^\infty \kappa^2 B(\kappa)\ \mathrm{d}\kappa \propto \int |\nabla b|^2\mathrm{d}x\mathrm{d}y, \tag{3.2c}$$

$$\int_0^\infty Z(\kappa)\mathrm{d}\kappa = \int_0^\infty \kappa^2 E(\kappa)\mathrm{d}\kappa \propto \int (\nabla\times\mathbf{u})\cdot(\nabla\times\mathbf{u})\ \mathrm{d}x\mathrm{d}y, \tag{3.2d}$$

$$\int_0^\infty Q(\kappa)\ \mathrm{d}\kappa \propto \int q^2\mathrm{d}x\mathrm{d}y, \tag{3.2e}$$

$$\int_0^\infty C(\kappa)\mathrm{d}\kappa \propto \int c^2\mathrm{d}x\mathrm{d}y. \tag{3.2f}$$

Note that a Cartesian $x-y$ domain and Fourier transform are assumed, again anticipating the model discretization to be analyzed. A proportionality is assumed between the integral of each power spectrum and the physical space area integral, because there are a variety of conventions as to how to choose the units of the power spectrum and thus the coefficient of proportionality may vary by convention. This proportionality holds under all conventions, however. In this manuscript, following Hamlington et al. (2014), after consistent normalization by the right hand side of equations (3.2a)-(3.2f), all comparable power spectra are rescaled by a convenient factor (often the value of the spectrum evaluated at the lowest wavenumber), which eliminates any ambiguity in definitions of the coefficients of the power spectra. This normalizing factor will be made explicit in each figure.

At the smallest scales between the Nyquist wavenumber (1/2 the sampling rate or $\pi/\Delta x$ in angular units) and $1/\sqrt{(}2)$ times it, the grid-scale acts as a filter introducing horizontal anisotropy affecting the diagnosed isotropized spectrum. However, it will be seen in the LES that the spectral effects of the subgrid scheme used in the model (Sullivan et al., 1994) extend to even larger scales. Likewise, at the largest scales, the square domain size affects the potential isotropy of the lowest wavenumbers and the wavenumber resolution of spectra in different directions.

By differentiation, the enstrophy (vorticity) spectrum is related to the kinetic energy (velocity) spectrum by $Z(\kappa) = \kappa^2 E(\kappa)$ (Kraichnan, 1967), and the buoyancy gradient spectrum is related to the buoyancy spectrum by $\kappa^2 B(\kappa)$ (Fox-Kemper et al., 2011). Note that the terminology here is somewhat inconsistent as enstrophy and energy are squared quantities while buoyancy gradient and buoyancy are not. For consistency, one could refer to the set (3.2a)-(3.2f) as the velocity, buoyancy, buoyancy gradient, vorticity, potential vorticity, and tracer spectra, or the kinetic energy, enstrophy, buoyancy variance, and buoyancy gradient variance, potential enstrophy, and tracer concentration variance spectra. Here we will use preferentially use the former set which is more concise on most occasions here, but in all cases the list (3.2a)-(3.2f) indicate the correct formulation.

In the mesoscales, the interior or Charney (1971) quasi-geostrophic regime where potential vorticity dynamics are best understood and are expected to govern spectra, the potential vorticity, buoyancy, and velocity spectra all scale as κ^{-3}, which means that the buoyancy gradient and vorticity spectra scale as κ^{-1}. The QG turbulence velocity spectra in this regime closely resemble those of 2D turbulence (Kraichnan, 1967), but of course 2D turbulence does not have stratification or PV (e.g. Fox-Kemper and Menemenlis, 2008; Bachman et al., 2017a). Surface quasi-geostrophy has a more complex spectral dependence and interpretation (Callies and Ferrari, 2013; Bodner et al., 2020).

In near-surface submesoscale simulations and observations, buoyancy and velocity spectra all scale as κ^{-2} (Capet et al., 2008c; Callies and Ferrari, 2013; Chereskin et al., 2019) . Thus, the buoyancy gradient and vorticity spectra are white, scaling as κ^{0} (Fox-Kemper et al., 2011).

However, in isotropic 3D turbulence with weak temperature gradients or passive scalar gradients, the Kolmogorov (1941)-Corrsin (1951) scalings for buoyancy and velocity spectra all scale as $\kappa^{-5/3}$. The Ozmidov (1965) scale is generally taken as the scale at which energy density is high enough that buoyancy stratification can be considered weak in this sense. Many oceanographers prefer the Thorpe (1977) scale in identification of near-surface overturning and mixing (Dillon, 1982), but here the focus on cascade theories makes the Ozmidov scale much more natural. Thus, the buoyancy gradient and vorticity spectra are taken to scale as $\kappa^{1/3}$ on scales finer than the Ozmidov scale. Since PV is the co-variance of the vorticity and buoyancy gradient, these scaling properties also extend to the PV field, where we expect a slope ranging between $\kappa^{1/3}$ (effectively assuming that buoyancy behaves as a passive scalar stirred by dominantly unbalanced motions) and $\kappa^{2/3}$ (when the buoyancy gradient and vorticity are perfectly correlated–e.g., motion dominated by PV inversion). These observations are not new, and have been discussed in several other studies (see e.g., Herring et al., 1994; Kunze, 2019, and references therein). However, here the emphasis is the significance of a positive slope which is terminated at the grid-scale of a Large Eddy Simulation, which implies that the smallest scales contain the largest variance per unit wavenumber and are likely to dominate the integrated vorticity, buoyancy gradient, and especially PV variance. This somewhat familiar property of PV has important implications to the study of turbulent fluxes in LES, as will be explained below.

3.3 Modeled Potential Vorticity in Multiscale Simulations

Hamlington et al. (2014) and Suzuki et al. (2016) describe simulations that are either interpreted as extremely high resolution submesoscale simulations or extremely large domain nonhydrostatic Large Eddy Simulations (LES) of boundary layer turbulence, where rotation and stratification become dominant at the largest scales (see also: Taylor and Ferrari, 2011; Skyllingstad and Samelson, 2012; Whitt and Taylor, 2017; Matheou et al., 2017; Callies and Ferrari, 2018; Pham and Sarkar, 2018; Sullivan and McWilliams, 2018). Hamlington et al. (2014) and Suzuki et al. (2016) describe LES of the spindown of a temperature front in the presence of submesoscale eddies, winds, and waves and these simulations are analyzed here. The surface wave-averaged Boussinesq equations with and without Stokes drift wave forcing are solved to simulate the interactions between submesoscale

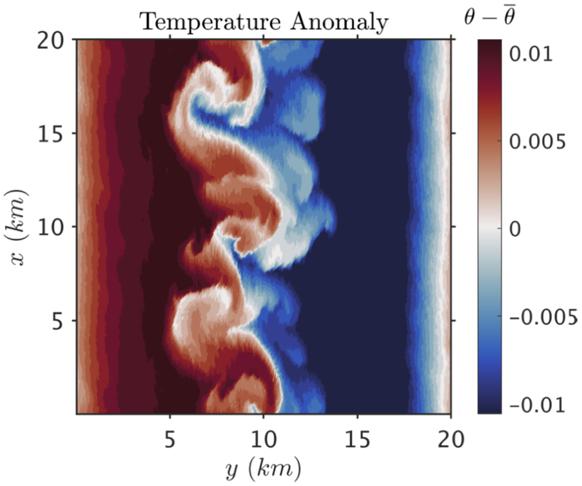

Figure 3.1: Plane view of a snapshot of the near-surface ($z = -3$m) temperature anomaly $\theta - \overline{\theta}$ after the development of submeosocale instabilities. Where $\overline{\theta} = 290.16K$ is the background temperature field.

processes and boundary layer turbulence, including Langmuir turbulence. Figure 3.1 illustrates a snapshot of the temperature field anomaly $\theta - \overline{\theta}$ near the surface ($z = -3m$) after the development of submeosocale instabilities, where $\overline{\theta} = 290.16K$ is the background temperature field.

Importantly for this study, these simulations span over three decades of horizontal resolution, allowing roughly a decade of classic submesoscale turbulence – exhibiting a quasi-balanced regime scaling of $E(\kappa)$, $B(\kappa) \propto \kappa^{-2}$ – and a near-decade of boundary layer turbulence – exhibiting a Kolmogorov-Corrsin like scaling of $E(\kappa)$, $B(\kappa) \propto \kappa^{-5/3}$ (circularly integrated spectra shown in Fig. 3.2). In these simulations, the mixed layer is found to be $50m$ in some regions, and shallower in others. Here we choose to examine the spectral properties at three different depths: near surface ($z = -3m$), within the mixed layer ($z = -25m$), and below the mixed layer ($z = -60m$).

The Ozmidov (1965) wavenumber,

$$k_{Oz} = (N^3/\varepsilon)^{1/2} \tag{3.3}$$

and ε are shown in figure 3.3 for the No-Stokes drift simulations, where ε is the dissipation rate and N is the Brunt-Väisälä frequency. These simulations use the Sullivan et al. (1994) subgrid scheme with an explicit dependence on the estimated dissipation rate ε, thus ε can be calculated from the prognostic subgrid turbulent kinetic energy which is then used to calculate k_{Oz}. The black circles in Fig. 3.3 mark the depths of the spectra displayed in Fig. 3.2. As depth increases, the Ozmidov length scale decreases, indicating that the transition to 3D turbulence is found at smaller scales, as expected below the mixed layer, declining fast below $z = -50m$. The Ozmidov wavenumber, thus estimated, proves to be a good approximation of when the u, v, w components of the velocity

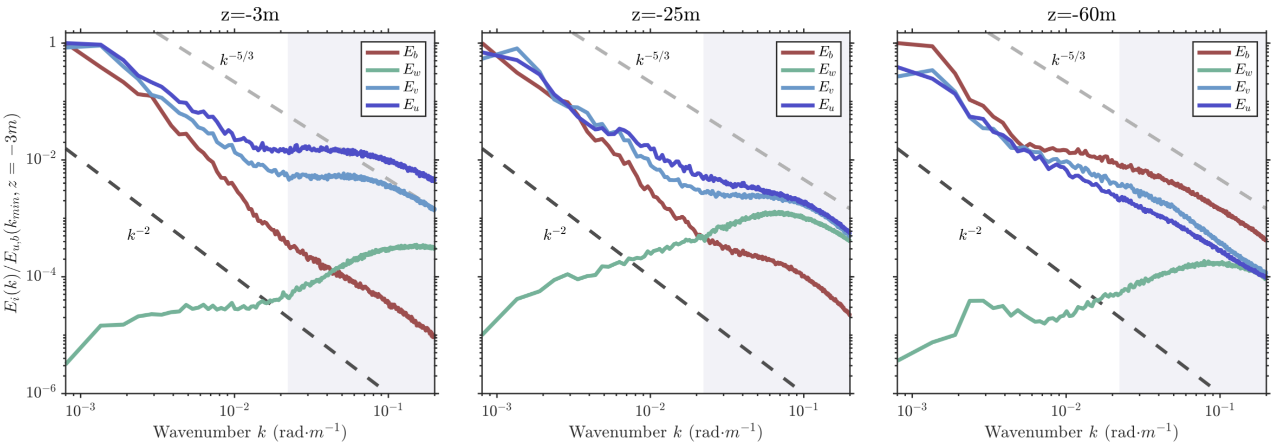

Figure 3.2: Circularly integrated spectra of the velocity vector (u, v, w) normalized by the $z = -3$m values of the $E_u(k_{min})$ and buoyancy field b normalized by $E_b(k_{min})$, examined at depths: near surface (left, $z = -3$m), within the mixed layer (middle, $z = -25$m), and below the mixed layer (right, $z = -60$m). Dashed lines denote the $k^{-5/3}$ slope (light grey) and k^{-2} slope (dark gray) for reference. The shaded region is taken as the cutoff scale of 3D turbulence at $400m$ in the decomposition described in section 3.4.

spectra attain a similar magnitude and behavior, a necessary criterion for isotropy. Note that at $z = -60$m the Ozmidov length scale is at roughly $8m$, closely approaching the grid scale of $4.5m$, and the interpretation of the 3D turbulence regime, especially with regard to gradients, is likely to be inaccurate. Also note that at the near-surface $z = -3$m location, near-surface suppression of the vertical velocity magnitude is apparent even below the Ozmidov scale, which is perhaps a deficiency of the LES (Ducros et al., 1998) or a sign of the similarity scaling enforced by the Sullivan et al. (1994) scheme. In any LES, isotropization is unlikely to be fully realized, and the resolution of this particular model is marginal as an LES to accomodate the large domain (Van Roekel et al., 2012), nonetheless it is anticipated that the PV dynamics that occur in this model will be mostly generic due to the theoretical considerations from the previous section.

A critical modeling viewpoint is that in LES, or more generally modeling of flows without a scale separation between parameterized unresolved phenomena and the grid scale, is meaningful only when the resolved flow variables are dominated by the larger eddies or larger, resolved scales of the power spectrum, or are at least uniformly distributed across spectral space–i.e., a white power spectrum. If the smaller-scale end of the variable in question dominates, then an “ultraviolet catastrophe” occurs wherein the most important variability in that variable is contributed from the flow that occurs on scales smaller than the resolution, and any deficiencies of the subgrid scheme contaminate the basin-integrated variance of this variable at leading order (3.2a)-(3.2f).

The components of the vorticity and buoyancy gradient spectra are shown in Fig. 3.4. These components are not yet isotropic, nor are they all oriented at a positive slope. The aforementioned limited resolution beyond the Ozmidov scale is one reason for this, as is the fact that a deliberate effort in subgrid modeling is required to have good spectral properties in these quantities near the

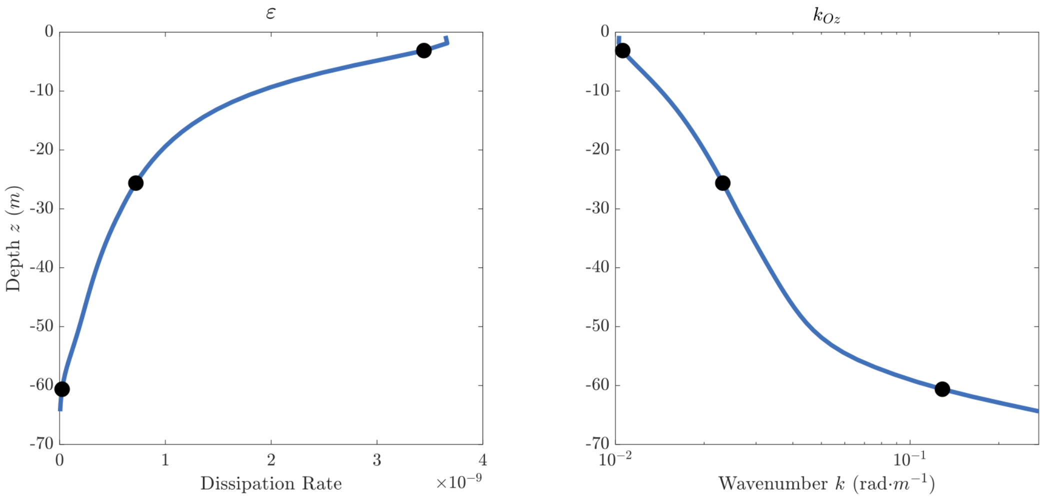

Figure 3.3: Depth profiles of the dissipation rate ε (left) and Ozmidov scale wavenumber k_{Oz} (right). Black circles mark the three depths shown in figure 3.2.

grid-scale (Johnson and Meneveau, 2018). Harcourt et al. (2002) suggest some remedies involving improved LES filtering that may also improve the spectral behavior of velocity gradients near the gridscale that were not utilized in these simulations. However, even with these deficiencies, the PV spectrum still reveals the issue at the center of this study.

The spectrum of PV, i.e. the product of spectral quantities in Fig. 3.4, is shown in Fig. 3.5. At all depths, at least one of the PV components in Fig. 3.4 display a positive slope nearing the smallest scales, as expected to occur when sufficiently below the Ozmidov scale. At the larger scales the near surface spectra displays a relatively flat slope, as expected for the submesoscale range (Capet et al., 2008b). These spectral properties (flat at large scales, positive near the highest wavenumber) extend to the total PV spectra shown in Fig. 3.5. Note that the PV is a convolution between the vorticity and buoyancy gradient when computed in wavenumber space, which highlights the correlation between these fields and may well vary across scales, so this result is not trivial.

The limited extent of the positive slope in this marginal resolution LES is theoretically predicted to extend up to the Kolmogorov microscale at least for the vorticity and buoyancy gradients independently if not for the PV (Johnson and Meneveau, 2018; Corrsin, 1951), which is $\kappa_K = \left(\frac{\nu^3}{\epsilon}\right)^{1/4} \approx$ 4mm for this simulation. At that scale, turbulent production of vorticity variance is matched by molecular viscous dissipation. By comparing this scale to the approximately 4m horizontal resolution of this model, if the spectrum of PV continues to scale near $k^{1/3}$, then the spectrum of PV will be 20 times higher at κ_K than it is at the grid-scale here. If the correlation between vorticity and buoyancy gradients persists (leading to a spectrum proportional to $k^{2/3}$) then the spectrum will be 460 times larger at κ_K than at this models' grid-scale. Fig. 3.5 includes also the spectra of the Stokes drift forced runs where small-scale vertical transport and mixing, due to the induced Langmuir turbulence, is 4 times greater (Hamlington et al., 2014). For these runs much of the variance is located at smaller scales and within the mixed layer even surpasses that of the

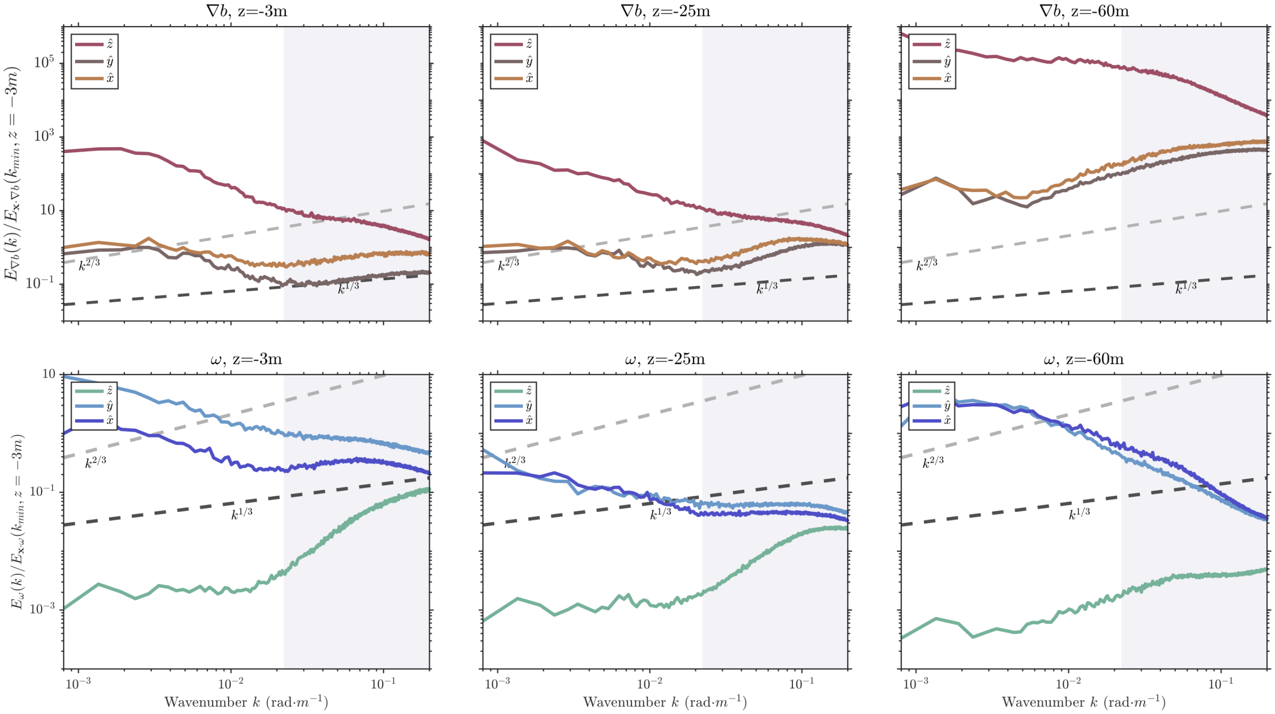

Figure 3.4: Circularly integrated spectra of the buoyancy gradient components normalized by $E_{\mathbf{x}\cdot\nabla b}(k_{min})$ (top panels) at $z = -3$m and vorticity components normalized by $E_{\mathbf{x}\cdot\boldsymbol{\omega}}(k_{min})$ at $z = -3$m (bottom panels), at the same depths shown in Fig. 3.2. Here, dashed lines denote the $k^{2/3}$ slope (light grey) and $k^{1/3}$ slope (dark gray) for reference. Shaded region is the same as in Fig. 3.2.

larger scale. We would expect similar results if finer resolution Stokes-free runs had been available, resolving further into the 3D turbulence regime.

As discussed above, in interior QG simulations, the buoyancy gradient and vorticity spectra scale as κ^{-1}, and for near-surface submesoscale, the spectra are white, scaling as κ^{0}. However in boundary layer LES simulations, the Kolmogorov-Corrsin scalings of the buoyancy gradient and vorticity spectra scale as $\kappa^{1/3}$: an ultraviolet catastrophe in both fields. LES is inconsistent if unresolved turbulence dominates over turbulence at the grid-scale, i.e., when unresolved statistics dominate those of resolved Large Eddies that dominate many statistics of the turbulence. In this case, the PV over all resolved scales cannot be meaningfully examined, because the PV variance is dominated by unresolved scales, and even the resolved PV variance is dominated by scales that are contaminated by spurious subgrid scheme effects. Johnson and Meneveau (2018) argue that this effect can be ameliorated for the velocity gradients, e.g., near grid-scale vorticity statistics can be improved through reworking LES subgrid schemes, but so far no such scheme has been developed to affect both buoyancy and momentum equations in such a way as to produce the correct near grid-scale behavior of PV.

However, LES are valuable because they do a good job of predicting large-scale momentum and

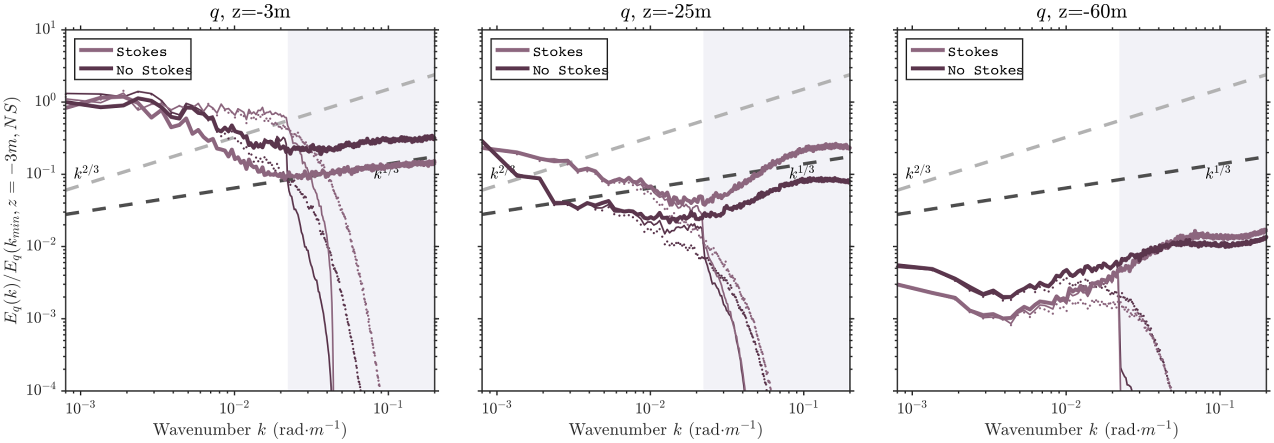

Figure 3.5: Same as in figure 3.4 for PV in the Stokes drift forced case (light magenta) and No Stokes drift case (dark magenta). Thin lines denote the sharp cutoff pre-filtered PV and dotted lines denote the Gaussian pre-filtered PV for both cases, as discussed in section 3.5. Shaded region is the same as in Fig. 3.2. All spectra are normalized by $E_q(k_{min})$ at $z = -3$m of the No Stokes case.

buoyancy variability–i.e., that of the "large eddies". As PV is a derived quantity–with a dynamical equation formed by differentiation and combination of the buoyancy and momentum equations–if the buoyancy and momentum are pre-lowpass-filtered *before* calculating the PV field and its budget, then that system can be meaningfully related to the submesoscale and mesoscale PV budgets. Furthermore, by locating the filter scale as to average and smooth over all variability with Kolmogorov-Corrsin scalings, evaluating the pre-filtered velocity and pre-filtered buoyancy will exclude all of the variability in this regime and the problematic PV variability. Thus, pre-filtering of the velocity and buoyancy up to the largest scale of the boundary layer turbulence is required for PV dynamics in LES to be meaningful.

3.4 Pre-filtering and Reynolds Averaging

In discrete spectral space a Reynolds average or smoothing filter can be constructed from using summation over resolved scales from the largest wavenumber based on the basin dimension to a cutoff wavenumber K (Frisch, 1995; Buzzicotti et al., 2018). In complex topography or heterogeneous flows, spectral transforms are not convenient, so a variety of other filtering approaches can be taken (with important caveats, Aluie et al., 2018; Bachman et al., 2017a; Hudgins et al., 1993). Defining an average based on this cutoff,

$$\mathcal{E}_K \equiv \frac{1}{2}\mathbf{u}_K^< \cdot \mathbf{u}_K^< = \frac{1}{2}\sum_{\kappa \le K} \left|\hat{u}_K^<\right|^2, \tag{3.4a}$$

$$\mathcal{B}_K \equiv \frac{1}{2}\left|b_K^<\right|^2 = \frac{1}{2}\sum_{\kappa \le K} \left|\hat{b}_K^<\right|^2, \tag{3.4b}$$

$$\mathcal{Q}_K \equiv \frac{1}{2}\left|q_K^<\right|^2 = \frac{1}{2}\sum_{\kappa \le K} \left|\hat{q}_K^<\right|^2, \tag{3.4c}$$

$$\mathcal{C}_K \equiv \frac{1}{2}\left|c_K^<\right|^2 = \frac{1}{2}\sum_{\kappa \le K} \left|\hat{c}_K^<\right|^2, \tag{3.4d}$$

where $\hat{\cdot}$ denotes the discrete (horizontal) Fourier transform, and $\kappa = \sqrt{k^2 + l^2}$ is the wavenumber magnitude. The essential aspect of this work is noting that because PV is the product of the vorticity and buoyancy gradient, and thus inherently nonlinear, the calculation of PV does not commute with averaging, and thus the spectra of PV are nontrivially related to the spectra of vorticity variance and buoyancy gradient variance.

By differentiation, the enstrophy spectrum is related to the energy spectrum, and the buoyancy gradient spectrum is related to the buoyancy spectrum.

$$\mathcal{Z}_K \equiv \frac{1}{2}\left(\nabla \times \mathbf{u}_K^<\right) \cdot \left(\nabla \times \mathbf{u}_K^<\right) = \frac{1}{2}\sum_{k \le K} \kappa^2 \left|\hat{u}_K^<\right|^2. \tag{3.5a}$$

$$\frac{1}{2}\left|\nabla b_K^<\right|^2 = \frac{1}{2}\sum_{\kappa \le K} \kappa^2 \left|\hat{b}_K^<\right|^2. \tag{3.5b}$$

This result will not be sensitive to the details of the filtering scheme in the mesoscale regime, where even the enstrophy and buoyancy gradient spectra are expected to be dominated by large scales; in the submesoscale and 3D turbulence regimes the choice of spectral filter will affect the result (Buzzicotti et al., 2018).

Note that the buoyancy gradient, vorticity, and velocity do not have a mean value in isotropic 3D turbulence, as by definition an isotropic flow implies that there is no statistically meaningful directionality of any mean field:

$$\overline{\nabla b} = 0,\ \overline{\nabla \times \mathbf{u}} = 0,\ \text{and}\ \overline{\mathbf{u}} = 0,\ \text{but}\ \overline{\nabla \times \mathbf{u} \cdot \nabla b} \neq 0. \tag{3.6}$$

Thus, mean values of these fields will vanish, allowing LES to predict their larger scales without undue contamination by isotropic small-scale turbulence. However, due to the nonlinearilty of PV, their contribution to the PV does not vanish and may dominate the small- and even large-scale PV variance.

It is important to note that for the small-scale contributions to dominate the variance of a field, its small-scale spectrum must be both blue and *deep*–i.e., spanning a sufficient range of scales–so as to have sufficient variance per unit wavenumber at small scales to dominate the overall contribution to integrals such as (3.2c)-(3.2e). The present theory of rotating, stratified turbulence in seawater anticipates no meaningful deviations from the cascade behavior at scales slightly smaller than the Ozmidov scale where isotropization occurs (in flows where $N > f$) and those near the Kolmogorov scale where viscosity becomes dominant (for fluids where viscosity is larger than diffusivity), so if the spectrum is blue just beyond the Ozmidov scale then it is expected to remain so until the molecular viscosity takes over near the Kolmogorov scale (Kunze, 2019).

Note that to be consistent with Reynolds averaging, here the simulations are processed using a sharp cutoff with no dealiasing (Orszag, 1971) rather than a smoother roll-off, to preserve (i) the idempotent property that defines a Reynolds average, $\overline{\overline{\cdot}} = \overline{\cdot}$ and $\overline{\cdot'} = 0$ where overbar indicates an average and primes denote the perturbation from the average, and (ii) the property that temporal and spatial derivatives commute with the cutoff filter. An example of a smooth Gaussian filter will be presented in the following section for comparison.

However, to retain the generality of the equations, we will avoid assuming that the averaging or filtering operation is a Reynolds average or that the spatial derivatives commute with the filter. This involves using the total turbulent stress divergence form $\overline{\nabla \cdot \mathbf{uu}} - \nabla \cdot \overline{\mathbf{u}}\,\overline{\mathbf{u}}$ rather than the Reynolds stress divergence $\nabla \cdot \overline{\mathbf{R}} \equiv \nabla \cdot \overline{\mathbf{u}'\mathbf{u}'}$. If the filter commutes with differentiation but is not idempotent, then the total turbulent stress tensor that results includes the Leonard stress ($\overline{\mathbf{L}} \equiv \overline{\overline{\mathbf{u}}\,\overline{\mathbf{u}}} - \overline{\mathbf{u}}\,\overline{\mathbf{u}}$) of resolved-but-turbulent motions, the cross stress ($\mathbf{C} \equiv \overline{\mathbf{u}'\,\overline{\mathbf{u}}} + \overline{\overline{\mathbf{u}}\mathbf{u}'}$), and the Reynolds stress contributions (Leonard, 1975). In practice, only the Leonard stress will be explicit, as much of the cross and Reynolds stresses will be parameterized in LES. The same approach is taken with the buoyancy fluxes.

The filter will be assumed to commute with time derivatives, but the commutation of the filter with spatial derivatives will not be assumed, which is difficult to achieve in practice–a sharp spectral cutoff does so, as does an ensemble average. Instead, only one additional constraint on the filter will be required, which is

$$\nabla \times \overline{\nabla P} = 0. \tag{3.7}$$

Where P is the pressure. It will also be assumed that

$$\nabla \cdot \overline{\mathbf{u}} = 0, \tag{3.8}$$

which makes the pre-filtered PV materially conserved in absence of dissipation as well as conserved in flux form. Note that (3.7) and (3.8) are much less restrictive than assuming that all derivatives commute with the filter.

With these definitions in mind, the consideration of the pre-filtered PV equation begins with the buoyancy and momentum equations.

3.5 Pre-filtered Potential Vorticity

The Boussinesq governing equations for the momentum and buoyancy are

$$\frac{\partial \mathbf{u}}{\partial t} + \nabla\cdot(\mathbf{u}\mathbf{u}) + \mathbf{f}\times\mathbf{u} = \frac{D\mathbf{u}}{Dt} + \mathbf{f}\times\mathbf{u} = -\frac{1}{\rho_0}\nabla P + b\mathbf{k} + \mathbf{F}, \tag{3.9a}$$

$$\frac{\partial b}{\partial t} + \nabla\cdot(\mathbf{u}b) = \frac{Db}{Dt} = \mathcal{D}. \tag{3.9b}$$

$\mathbf{F}$ and $\mathcal{D}$ are the frictional and diabatic terms respectively, which in an LES-like model are the parameterized unresolved turbulent fluxes (e.g. Moeng, 1984; Deardorff, 1980) and in DNS are molecular viscosity and diffusivity. $\mathbf{f}$ is the Coriolis parameter vector, which is not required to be vertical or constant in space, although it will be both in the simulations analyzed and assumed to be slowly varying enough that it is unaffected by averaging. Consistent with the Boussinesq approximation, it is also assumed that $\nabla\cdot\mathbf{u} = 0$.

Forming the vorticity equation and the gradient of the buoyancy equation from (3.9a)-(3.9b), the PV equation is formed first by multiplying these times the appropriate factors.

$$\begin{aligned}\nabla b\cdot\frac{D(\nabla\times\mathbf{u}+\mathbf{f})}{Dt} &= \nabla b\cdot\left((\nabla\times\mathbf{u}+\mathbf{f})\cdot\nabla\mathbf{u} + \nabla\times(b\mathbf{k}) + \nabla\times\mathbf{F}\right),\\ &= \nabla b\cdot\left[(\nabla\times\mathbf{u}+\mathbf{f})\cdot\nabla\mathbf{u}\right] + \nabla b\cdot\{\nabla\times\mathbf{F}\}.\end{aligned} \tag{3.10a}$$

$$\begin{aligned}(\nabla\times\mathbf{u}+\mathbf{f})\cdot\frac{D(\nabla b)}{Dt} &= -\nabla b\cdot\left[(\nabla\times\mathbf{u}+\mathbf{f})\cdot\nabla\mathbf{u}\right] + \{\nabla\times\mathbf{u}+\mathbf{f}\}\cdot\nabla\left(\frac{Db}{Dt}\right),\\ &= -\nabla b\cdot\left[(\nabla\times\mathbf{u}+\mathbf{f})\cdot\nabla\mathbf{u}\right] + \{\nabla\times\mathbf{u}+\mathbf{f}\}\cdot\nabla\mathcal{D},\end{aligned} \tag{3.10b}$$

and summing to form the product rule, which cancels out the vortex stretching term in square brackets, leaving behind the forcing terms in curly brackets,

$$\frac{Dq}{Dt} = \nabla b\cdot\frac{D(\nabla\times\mathbf{u}+\mathbf{f})}{Dt} + (\nabla\times\mathbf{u}+\mathbf{f})\cdot\frac{D(\nabla b)}{Dt} = \{\nabla\times\mathbf{F}\}\cdot\nabla b + \{\boldsymbol{\omega}+\mathbf{f}\}\cdot\nabla\mathcal{D}. \tag{3.11}$$

It will also be assumed that $\nabla\times\mathbf{k} = 0$, which is true in flat domains where $\mathbf{k}$ (the direction of gravity) is spatially constant and on a sphere where $\mathbf{k}$ is radially oriented, to make $\nabla b\cdot\nabla\times(b\mathbf{k}) = \nabla b\cdot(b\nabla\times\mathbf{k}) = 0$.

To summarize, the resulting Boussinesq PV equation is

$$\frac{\partial q}{\partial t} + \nabla\cdot(\mathbf{u}q) = \frac{Dq}{Dt} = (\nabla\times\mathbf{F})\cdot\nabla b + (\boldsymbol{\omega}+\mathbf{f})\cdot(\nabla\mathcal{D}) \tag{3.12}$$

Which can also be written as

$$\frac{\partial q}{\partial t} = -\nabla\cdot\mathbf{J} \tag{3.13}$$

Where $\mathbf{J} = \mathbf{u}q - \mathbf{F}\times\nabla b - (\mathbf{f}+\boldsymbol{\omega})\mathcal{D}$ are the “J-fluxes” of PV. In both forms of the PV equation, the PV evolves according to both the frictional and diabatic effects, $\mathbf{F}$, $\mathcal{D}$, and the advective fluxes,

$\mathbf{u}q$, but only in (3.13) is it apparent that all of these effects can be written in flux form (Haynes and McIntyre, 1987; Marshall and Nurser, 1992).

However, in the 3D turbulence regime, the curl of the momentum equation and the gradient of the buoyancy equation are dominanted by the gridscale noise, so the resulting PV equation is contaminated. By contrast, the pre-filtered PV is constructed from the pre-filtered velocity and buoyancy fields, to avoid the ultra-violet catastrophes.

$$\tilde{q} \equiv (\nabla \times \overline{\mathbf{u}} + \mathbf{f}) \cdot \nabla \overline{b} \tag{3.14}$$

Note that $\tilde{q} \neq \overline{q}$, as the velocity and buoyancy are filtered *before* forming $\tilde{q}$, whereas $\overline{q}$ is filtered after the PV is formed from the unfiltered fields. As PV is a nonlinear combination of buoyancy and momentum, these operations do not commute. Also as PV is nonlinear, care to avoid aliasing unresolved buoyancy gradient or vorticity wavenumbers into the resolved range when calculating the pre-filtered PV is needed, dealiasing of quadratic nonlinearities is guaranteed if the filter eliminates 1/3 or more of the resolved wavenumbers (Orszag, 1971). However, the pre-filtering advocated from a physical perspective goes far beyond this numerical constraint: in the simulations analyzed the optimal filter wavenumber is near the 15^{th} out of 2049. As with kinetic energy of filtered fields (Aluie et al., 2018), an exact budget for the pre-filtered PV can be constructed and analyzed.

Fig. 3.6 shows a plane view of the near-surface PV before and after pre-filtering of the velocity and buoyancy fields using a sharp cutoff filter and a standard Gaussian filter with the same cutoff scale at 400m. Highlighted by the shaded region in Figure 3.5, the cutoff scale is $400m$, chosen here to correspond with the loss of hydrostatic balance found in Hamlington et al. (2014) which also corresponds to the scale of change in slope in gradients in Figure 3.4 and change in slope of PV near the surface and within the mixed layer (Fig. 3.5). The unfiltered PV is contaminated by small scale variance that distracts from the larger scale features which appear after the pre-filtering is applied (thick vs thin and dotted lines in Fig.3.5). The advantages of choosing a sharp cutoff are discussed in the previous section, yet one disadvantage is the ringing effect as evident in Fig. 3.6 which is otherwise smoothed by the Gaussian filter. In the Stokes drift forced case, where small scale mixing is very intense near the surface, the PV is contaminated heavily at all scales. The pre-filtered PV in Fig. 3.5 exhibits a flat slope throughout most of the submesoscale. This particular property of Stokes forced mixing will be examined more carefully in a future study. Furthermore, the transports of the unfiltered PV cannot be obtained cleanly from the model, as will be shown next.

The filtered versions of the momentum and buoyancy equations (3.9a) and (3.9b) are

$$\frac{\partial \overline{\mathbf{u}}}{\partial t} + \nabla \cdot (\overline{\mathbf{u}}\,\overline{\mathbf{u}}) + \mathbf{f} \times \overline{\mathbf{u}} = -\frac{1}{\rho_0}\overline{\nabla P} + \bar{b}\mathbf{k} + \overline{\mathbf{F}} - \overline{\nabla \cdot (\mathbf{u}\mathbf{u})} + \nabla \cdot (\overline{\mathbf{u}}\,\overline{\mathbf{u}}) = -\frac{1}{\rho_0}\overline{\nabla P} + \bar{b}\mathbf{k} + \overline{\mathbf{F}^{+}}, \tag{3.15a}$$

$$\frac{\partial \bar{b}}{\partial t} + \nabla \cdot (\overline{\mathbf{u}}\bar{b}) = \overline{\mathcal{D}} - \overline{\nabla \cdot (\mathbf{u}b)} + \nabla \cdot \left(\overline{\mathbf{u}}\bar{b}\right) = \overline{\mathcal{D}^{+}}, \tag{3.15b}$$

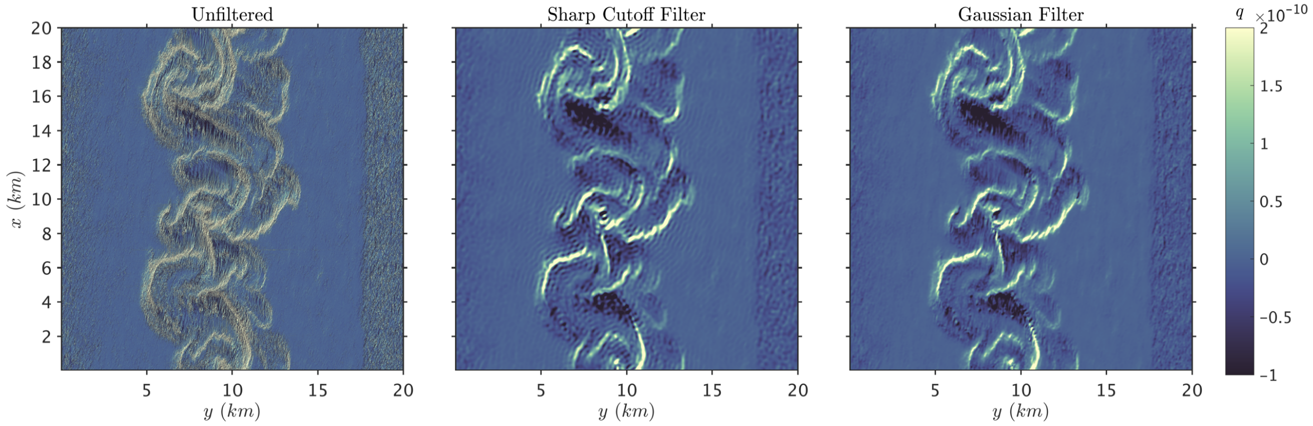

Figure 3.6: Plane view of a snapshot of the near-surface ($z = -3m$) PV field without pre-filtering of the velocity and buoyancy fields (left), and after using a sharp cutoff filter (center) and Gaussian filter (right) on the buoyancy and velocity fields separately before calculating the PV as in (3.14). The cutoff scale here is 400m which corresponds to the shaded regions in Fig. 3.2,3.4 and 3.5.

where the superscript plus symbol indicates the frictional and diabatic effects *including the total turbulent stress and total turbulent buoyancy flux and any potential non-commutation of filter and spatial derivatives*. It is assumed that temporal and spatial derivatives commute with the filtering operation, which also guarantees that $\nabla\cdot\overline{\mathbf{u}} = 0$. Following the same procedure as that to form (3.12), but using (3.15a)-(3.15b) in place of (3.9a)-(3.9b), the pre-filtered PV equivalent of (3.12) is

$$\frac{\partial \tilde{q}}{\partial t} + \nabla\cdot(\overline{\mathbf{u}}\tilde{q}) = \frac{\overline{D}\tilde{q}}{Dt} = \left(\nabla\times\overline{\mathbf{F}^{+}}\right)\cdot\nabla\overline{b} + (\overline{\boldsymbol{\varpi}}+\mathbf{f})\cdot\nabla\overline{\mathcal{D}^{+}}, \tag{3.16}$$

where $\frac{\overline{D}}{Dt}$ includes advection by $\overline{u}$ only. Equation (3.16) can also be written in flux form,

$$\frac{\partial \tilde{q}}{\partial t} = -\nabla\cdot\left[\overline{\mathbf{u}}\tilde{q} - \overline{\mathbf{F}^{+}}\times\nabla\overline{b} - (\mathbf{f}+\boldsymbol{\omega})\overline{\mathcal{D}^{+}}\right]. \tag{3.17}$$

Note that no commutation of spatial derivatives and averages is assumed in this derivation (only $\nabla\cdot\overline{\mathbf{u}} = 0$), and the pre-filtered PV equation (3.16) has the expected form of a PV conservation equation, with the "frictional" and "diffusive" operators (that actually also contain turbulent transports):

$$\overline{\mathbf{F}^{+}} = \overline{\mathbf{F}} - \overline{\nabla\cdot(\mathbf{u}\mathbf{u})} + \nabla\cdot(\overline{\mathbf{u}}\,\overline{\mathbf{u}})\,, \tag{3.18a}$$

$$\overline{\mathcal{D}^{+}} = \overline{\mathcal{D}} - \overline{\nabla\cdot(\mathbf{u}b)} + \nabla\cdot(\overline{\mathbf{u}}\overline{b}) \tag{3.18b}$$

As (3.16) and (3.17) have the expected form, *the pre-filtered PV behaves as expected for all geophysical applications.* These are the operators that need to be assessed in LES to understand PV injection at the surface, not just the molecular or subgrid friction and diffusion. It is worthy to note that if the filtering operator is standard Reynolds averaging, equations (3.18a)-(3.18b) arrive at a similar expression as in Keyser and Rotunno (1990), following the original work by Staley (1960) and Shapiro

(1976, 1978). However, our emphasis here is on the particular application in the Kolmogorov regime using LES, which is not addressed by the previous authors.

The J-fluxes as written in (3.17) remain meaningful if the dissipative operators in (3.18a)-(3.18b) are used, and even though $\mathbf{F}$, $\mathcal{D}$, $\nabla \cdot (\mathbf{uu})$, and $\nabla \cdot (\mathbf{u}b)$ may be noisy, they are of exactly the form solved for by the modeled momentum and buoyancy equations at full resolution, including any oddities of discretization, dealiasing, etc. Under the pre-filtered PV approach, these noisy terms are never converted into J-fluxes before filtering, which leads to large aliasing contaminating even the large-scale J-fluxes (Fig. 3.7). To remove aliasing that will arise in calculating the advective J-fluxes (including the implied cubic nonlinearity in PV and energy budgets), the filter wavenumber should be half of the cutoff wavenumber (which is π over the gridscale) or below, equivalent to a smoothing operator over $4\Delta x$ or greater. This rule is stricter than filtering at the wavenumber that is 2/3 of the cutoff wavenumber allowed under quadratic nonlinearity, equivalent to smoothing over $3\Delta x$ or greater for quadratic nonlinearity (Orszag, 1971). By contrast, if one tries to calculate the advective J-fluxes that result from simply averaging (3.12), i.e., $\overline{\nabla \cdot \mathbf{u}q}$ and $\overline{\nabla \cdot \mathbf{u}\left([\nabla \times \mathbf{u} + \mathbf{f}] \cdot \mathbf{b}\right)}$, the calculation involves differentiating a triple-correlation that the model never predicts directly, is noisy, and depends on scales outside of those resolved in an LES–i.e., aliasing–to a degree not managed by normal dealiasing filters because it is a cubic instead of a quadratic nonlinearity, requiring filtering of not just 1/3 of resolved wavenumbers, but 1/2 (Orszag, 1971). Fig. 3.7 shows that even the large-scale J-fluxes are contaminated by aliasing between the small-scale and unresolved modes. Likewise, the frictional J-fluxes involve products of buoyancy gradients, vorticity, with noisy frictional terms which are not consistent with the discrete model prognostic equations.

3.6 Discussion and Conclusions

To meaningfully study PV in LES, via material conservation or via J-fluxes, a pre-filtered PV as in (3.14) with a physically-selected filter scale $\geq 4\Delta x$ is the most meaningful quantity, as it avoids spurious effects, aliasing, and noise. Momentum and buoyancy fluxes on scales below the submesoscale, including those of 3D turbulence, should be treated alongside parameterizations of momentum and buoyancy fluxes and bundled into the frictional and diabatic terms: $\overline{\mathbf{F}^{+}}, \overline{\mathcal{D}^{+}}$ as written in (3.18a)-(3.18b). By this method, correct interpretations of the PV evolution equations, (3.12)-(3.13), Kelvin's circulation theorem, the impermeability theorem (Haynes and McIntyre, 1987; Marshall and Nurser, 1992), and PV invertibility on the scales where it is the dominant constraint will be recovered.

In interior QG simulations, the PV, buoyancy, and velocity spectra all scale as κ^{-3}, which means that the buoyancy gradient and vorticity spectra still scale as κ^{-1}, and so are well-behaved even without filtering. Note that if the 3D turbulence scale is not resolved (e.g., in a hydrostatic general circulation model), the turbulent parameterizations $\mathbf{F}$ and $\mathcal{D}$ already contain the correct terms without additional pre-filtering. Thus, the distinction between the full PV and pre-filtered PV is not important in interior QG.

In near-surface submesoscale simulations, buoyancy and (horizontal) velocity spectra all scale as κ^{-2}. Thus, the buoyancy gradient and velocity gradient spectra are white, scaling as κ^0. However, the vertical vorticity spectrum is likely to resemble the interior QG scaling even as the surface velocity divergence spectrum does not (Callies and Ferrari, 2013; Rocha et al., 2016; Chereskin et al., 2019), which means that PV may be slightly red and thus meaningfully calculated without pre-filtering, although pre-filtering may still be desired to reduce aliasing in calculating advective terms. The parameterizations of boundary layer turbulence in such models are included in the dissipative terms.

In Direct Numerical Simulations the molecular viscous and Kolmogorov and Batchelor scales are thoroughly resolved (with at least 4 gridpoints). In this case pre-filtering across the dissipative scales will not affect the result (e.g. Herring et al., 1994), and cubic nonlinearity de-aliasing will suffice.

In boundary layer LES simulations, the Kolmogorov-Corrsin scalings for buoyancy and velocity spectra all scale as $\kappa^{-5/3}$, and the turbulence is isotropic. Thus, the buoyancy gradient and vorticity spectra scale as $\kappa^{1/3}$: an ultraviolet catastrophe in both fields. Furthermore, LES is inconsistent with the assumption that no important turbulence effects occur at scales near to or finer than the grid-scale. In this case, the full PV over all resolved scales cannot be meaningfully examined, because its variance is dominated by unresolved scales and its advective J-fluxes are dominated by triple correlations that depend on unresolved scales (Leonard, 1975; Clark et al., 1979). Even though backscatter parameterizations may improve velocity gradient statistics (Johnson and Meneveau, 2018), they have not been designed to correctly inject PV variance (if this is indeed possible). However, averaging or filtering the PV affects interpretation (Keyser and Rotunno, 1990). Thus, for the case of the Hamlington et al. (2014) and Suzuki et al. (2016) and related LES-including-submesoscale simulations, a course for how to manage the interpretation of potential vorticity analysis covering the transition from the submesoscale to the boundary layer scalings emerges. Pre-filtering of velocity and buoyancy up to the $O(H)$ scale, i.e., the largest scale of the boundary layer turbulence, is required before calculation of the PV, and here a meaningful construction of the resulting PV dynamics is given in (3.16)-(3.17). Although alternative expressions of PV may be useful for diagnostic purposes (e.g. Morel et al., 2019), pre-filtering is still necessary to avoid contamination from the smallest scales in either diagnostic method. In other circumstances, it may be more convenient to estimate this scale by the Ozmidov scale, by where the unfiltered PV spectrum inflection point lies, by the scale where nonhydrostatic effects (i.e., acceleration terms in the vertical momentum equation) become pronouced, by where the aspect ratio of motions in 3D is order one, or by where the u, v, w spectra all converge and then proceed on smaller scales with a $k^{-5/3}$ slope. Particular classes of less well-understood turbulence, such as that emanating alongside coherent structures (Taylor and Ferrari, 2009) or forced toward anisotropy by convection (Rincon, 2006), stratification (Kunze, 2019), or Stokes forces as in Langmuir turbulence (Hamlington et al., 2014; Suzuki and Fox-Kemper, 2016), merit a variety of these checks be made during the selection of a filter scale or procedure. Indeed, in Hamlington et al. (2014), the agreement among estimates of the isotropization scale differs between the simulation including Stokes forces and one without it (e.g., Fig. 3.5).

While the Boussinesq equations with buoyancy have been used here in the tradition of oceanic boundary layer LES (e.g. McWilliams et al., 1997), there is no reason why atmospheric boundary layer LES (e.g. Matheou et al., 2017) or cloud-resolving LES (e.g. Yamaguchi et al., 2017) would not also suffer the same issues with identifying the relevant PV dynamics or energy budgets. Other issues have been identified with PV intended to be used for atmospheric turbulence simulations (Herring et al., 1994), but here the focus is the method for producing the pre-filtered PV, why it is the right choice, and its evolution equations.

Acknowledgments

This research was made possible in part by a grant from The Gulf of Mexico Research Initiative and in part by NSF OCE 1350795, NSF OIA 1655221, and ONR N00014-17-1-2963. Data are publicly available through the Gulf of Mexico Research Initiative Information & Data Cooperative (GRIIDC) at https://data.gulfresearchinitiative.org (dois: 10.7266/N7BZ64FX, 10.7266/N7R49P5J, and 10.7266/n7-sgym-n883). Much of this work was developed during the Kavli Institute for Theoretical Physics, as part of the Planetary Boundary Layers in Atmospheres, Oceans, and Ice on Earth and Moons program, supported by the National Science Foundation under Grant No. NSF PHY 1748958. Furthermore, we would especially like to thank Brodie Pearson, JAMES editor Stephen Griffies, signed reviewer Jacob Wenegrat, and two anonymous reviewers for their insightful comments that have greatly improved this paper.

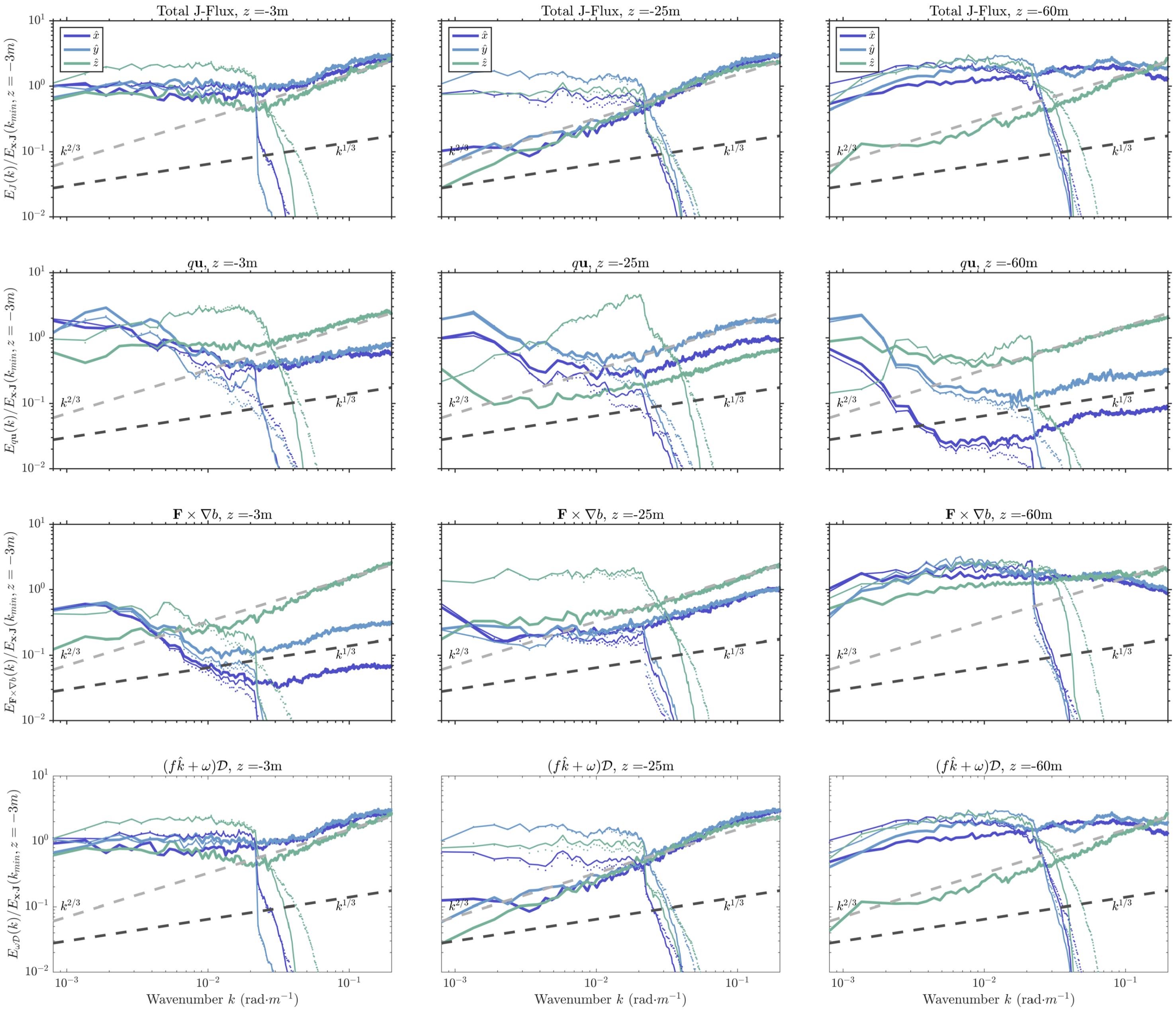

Figure 3.7: Same as in Fig. 3.5 for the J-flux spectra in the No Stokes drift case. Shown is the total J-flux (top row) and its components: $q\mathbf{u}$ (second row), $\mathbf{F}\times\nabla b$ (third row), and $(\mathbf{f}+\boldsymbol{\omega})\mathcal{D}$ (bottom row). Thick lines denote the unfiltered spectra, thin lines the sharp cutoff pre-filtering and dotted lines the Gaussian pre-filtering as described in section 3.5. All spectra are normalized by $E_{\mathbf{x}\cdot\mathbf{J}}(k_{min})$ at $z=-3$m.

Chapter 4

Arrest of Frontogenesis by Submesoscales and Boundary Layer Turbulence

This chapter is in preparation for submission as supporting material for the publication: Abigail S. Bodner, Baylor Fox-Kemper, Leah Johnson, Luke P. Van Roekel, James C. McWilliams, Peter P. Sullivan, & Paul S. Hall. "Modifying the Mixed Layer Eddies Parameterization to Include Frontogensis and Frontal Arrest by Boundary Layer Turbulence." (chapter 5).

4.1 Introduction

Frontogenesis occurs near the ocean surface, where forcing and stratification are complex. Winds, waves, and thermodynamic forcing contribute to boundary layer stratification and turbulence (Price et al., 1986). While the idealized model of Hoskins and Bretherton (1972) describes accurately many aspects of frontogenesis, it predicts frontal singularity in finite time. This is an unphysical outcome, so processes that arrest the front must appear in nature.

There are various instabilities that populate the upper ocean, due to the effects of winds, waves and stratification, that may affect the evolution of fronts: gravitational instability or pure convection (Haine and Marshall, 1998); symmetric instability (SI), which mixes along isopycnals in the presence of down-front winds and negative potential vorticity (PV) (Hoskins, 1974; Thomas et al., 2013; Bachman et al., 2017b); mixed layer baroclinic instability, which acts to restratify the mixed layer by slumping buoyancy gradients from horizontal to vertical (Boccaletti et al., 2007; McWilliams et al., 2009; McWilliams and Molemaker, 2011); Langmuir turbulence, which creates convergence zones at the ocean surface and contributes to upper ocean mixing (McWilliams et al., 1997; Hamlington et al., 2014; Suzuki et al., 2016); horizontal shear instability due to the sharpening front itself (Sullivan and McWilliams, 2018, 2019); and other mixing, wave breaking, and topographic effects (Garrett and Loder, 1981; Thompson, 2000; Teixeira and Belcher, 2002; Nagai et al., 2006; Sullivan et al., 2007; Gula et al., 2016). Some of these phenomena require horizontal gradients such as a front to exist (e.g., symmetric instability or baroclinic instability), while others are related more generally to surface forcing (e.g., boundary layer turbulence). Each of these instabilities may be recognized by characteristic energy sources, scale, and dependence on favorable stratification or shear conditions. In the ocean, observations are unable to simultaneously and conclusively isolate this set of constraints, so novel theoretical and modeling approaches are useful to study these processes and how they interact in a more idealized setting.

Submesoscale and boundary layer turbulence can be differentiated by their energetic properties (e.g. Hosegood et al., 2006; Haney et al., 2015), nonhydrostatic effects (Hamlington et al., 2014) and even dynamical properties such as PV (Bodner and Fox-Kemper, 2020). Large Eddy Simulations (LES) are useful numerical tools. In particular, they can resolve 3D turbulent processes such as nonhydrostatic effects which are fundamental for submesoscale currents and boundary layer turbulence. As computational capabilities have increased in recent years, several other studies have modeled the multiscale interactions between submesoscales and boundary layer turbulence.

Skyllingstad and Samelson (2012) studied the interaction between mixed layer baroclinic eddies (MLE) and small-scale turbulence using a nonhydrostatic LES of a warm filament in the presence of Langmuir turbulence, focusing primarily on the transfer of energy between MLE and boundary layer turbulence. Hamlington et al. (2014) studies the weak interaction limit between boundary layer turbulence and submesoscale eddies, and the associated instabilities that arise from this interaction. They compare cases of shear turbulence driven by wind stress, with Langmuir turbulence driven by wind and wave effects. Haney et al. (2015) focus more specifically on how wave effects can alter the PV field and promote certain instabilities along a submesoscale front. Suzuki et al. (2016) identifies a strain-induced front in a subdomain from the Hamlington et al. (2014) LES, and investigates what energizes and torques the submesoscale front in the presence of waves. Crowe and Taylor (2020) study the evolution of an idealized turbulent-induced (turbulent thermal wind, TTW) submesoscale front under varying wind stress and buoyancy flux conditions.

In chapter 1 (and in Bodner et al. (2020)), the effects of turbulence on frontogenesis were explored in a theoretical framework, using a perturbation method applied to the semigeostrophic equations. These assumptions imply the solution is valid for scales larger than ocean submesoscales and in a weak turbulence regime. PV dynamics were found to be central to this theory, primarily by connecting frontal dynamics with turbulence through the frictional and diabatic fluxes. However, this theory breaks down in a more realistic environment, such as the LES discussed in chapter 3 (and Bodner and Fox-Kemper (2020)), where boundary layer turbulence can no longer be assumed to be a small correction to submesoscale frontal dynamics. Nonetheless, the tendency of the different turbulent processes and their effects on frontogenesis are found to be consistent with other studies of frontal evolution, such as McWilliams (2017) and Sullivan and McWilliams (2018, 2019), where it is found that vertical turbulent fluxes help lead to frontogensis, and horizontal processes can arrest or contribute to its decay. Note that vertical and horizontal instabilities will lead to isotropic 3D turbulence, which will serve both roles eventually. Although many studies investigate the interaction between submesoscales and boundary layer turbulence, few focus on the mechanism of frontogenetic arrest, what are the turbulent properties of frontal arrest and what direct effect these may have on frontal width.

In this chapter, a suite of high resolution LES are presented and analyzed, where they capture the multiscale character of strain-induced frontogenesis, as it interacts with different instability and mixing mechanisms such as: wind forcing and waves, mixed layer instabilities, convection and symmetric instability. In all runs, after instabilities have saturated, the cross-frontal scale halts at a constant width and does not become infinitesimally thin, as theory would predict.

A description of the simulations forced by different turbulent processes is given in section 4.2, analysis methods for averaging, determining frontal width and boundary layer depth are described in section 4.3. Results are shown in section 4.4 and compared with those from Sullivan and McWilliams (2018, 2019) in section 4.5. Summary and discussion are given in section 4.6

4.2 Numerical Simulations

The simulations used in this study were designed to generate strain-induced fronts in a way that could approach equilibrium (frontogenetic arrest), influenced by small scale processes such as mixed layer instabilities (MLI), convection (equivalent to symmetric instability in the presence of a front), wind stress and waves (Stokes drift), all these forcings combined and none at all.

They are based on the National Center for Atmospheric Research (NCAR) LES (Moeng, 1984), and solve the wave-averaged Boussinesq (WAB), or Craik–Leibovich, equations (McWilliams et al., 1997; Sullivan et al., 2007), which reduce to the standard momentum and thermodynamic equations without waves, i.e. when the Stokes velocity is equal to zero.

The domain size is 20km in the horizontal and 200m in the vertical, with $1024 \times 1024 \times 256$ grid points in each direction respectively. All cases constituted of an initial frontal buoyancy gradient, set to equal the Coriolis parameter squared $\Delta b/\Delta X = f^2$, where $f = 7.2722 \times 10^{-5} s^{-1}$ and a strain field achieved by four imposed mesoscale (barotropic) eddies with a strain rate of 2×10^{-6}, where b is buoyancy, X is the cross-frontal length scale and f is the Coriolis parameter. The depth of the frontal zone was set to 75m, the background stratification is $N^2 = 10^{-6} s^{-2}$ and background mean temperature is set to $\theta_0 = 293.15 K^o$.

The NCAR LES is a pseudo spectral code in the horizontal, which means the horizontal derivative terms are computed in spectral space and the vertical derivatives by finite difference. The imposed mesoscale eddies were set spectral space by restoring the velocity and temperature to the first wavenumber (and the mean), which maintained the straining field. Additionally, physical space restoring was imposed on the temperature around the boundary such as a sponge layer (even though they are periodic). This was found to be necessary to preserve the sharpness of the front until equilibrium. There was also physical space restoring of temperature and momentum near the bottom

Case	Bu	u_S	τ	$\overline{w'b'}_0$	S_0
	–	$[m/s]$	$[m^{-1}s^{-2}kg]$	$[m^2s^{-3}kg]$	$[m^2s^{-3}kg]$
Convection	1	–	–	4.76×10^{-6}	-4.28×10^{-5}
Small MLI	$2.88 \times 10{-}3$	–	–	–	–
Stokes and Wind	1	0.02	1	–	–
No Forcing	1	–	–	–	–
All Forcing	$2.88 \times 10{-}3$	0.02	1	4.76×10^{-6}	-4.28×10^{-5}

Table 4.1: LES parameter configuration for the different simulation cases.

to prevent wave reflection from the hard boundary and pollution of the simulation.

The Burger number $Bu = (L_d/L)^2$ represents the ratio between the mixed layer deformation radius L_d and the maximum possible frontal width L, which is the distance between the two mesoscale eddies. The Burger number parameter is used as a proxy for the generation of MLE, which is based on the fastest growing mode from the linear instability theory developed by Boccaletti et al. (2007). This essentially prescribes how how many linear eddies can fit within the front in the initial state. MLI are a unique class of baroclinic instability that develop across the front in a weekly stratified mixed layer. In the absence of a prescribed mixed layer, baroclinic instability will extend until the bottom of the pycnocline, as in the mesoscale. Thus, the Burger number is set to 1 for Wind+Stokes, convection/SI and no forcing cases, as there is no mixed layer prescribed and no MLE expected to develop. In the the MLI and All Forcing cases, an initial mixed layer depth of 50m is prescribed, and the Burger number is set to 0.00288 which reflects that the linear eddies can become 17% of the size of the front, simulating how smaller MLEs interact with the strain-induced front.

Wind and wave effects are included by adding surface wind stress $\tau = 1$ and a Stokes surface velocity $u_s = 0.02$ that decays with depth. Here, both winds are waves are aligned and are in the cross-front y direction.

In the convection case, surface cooling is given by surface buoyancy flux $\overline{w'b'}_0 = 4.76 \times 10^{-6}$ and short wave solar radiation penetrates and heats from below $S_0 = -9 \times \overline{w'b'}_0 = -4.28 \times 10^{-5}$. This is essentially classic convection driven by Rayleigh Benard instability. Note that surface cooling in the presence of a front will result in negative PV. Thus, these conditions are also favorable for symmetric instability (SI) and this case will be referred to as convection/SI.

The all forcing case includes MLI, waves, wind stress and convection combined, and so all parameters are tuned on. In the no forcing case, only the Burger parameter is equal to 1, and the rest of the parameters are turned off. To ensure that frontal width did not depend on resolution, and that frontal arrest in fact results from the presence of turbulence, the no forcing case only exhibits the sharpening front and no additional turbulence. In this basic case, the front was found to sharpen to the point where small scale diffusivity became leading order, and was verified in several high and low resolution simulations (not shown).

A summary of these key parameters specified for each case is given in table 4.1.

4.3 Analysis

4.3.1 Averaging

Since the fronts in these simulations are not purely in one direction, and exhibit curvature due to the confluence of the straining eddies, it is not simple to average in the along-front direction. Hence, to perform the along-front average, we seek to average over lines that follow the fluid motion e.g. the strain field. To do so, we first identify the confluent sub-domain, which is where the front is strained by the imposed eddies. This is approximately the middle quarter of the domain, and is about 10km in both x, y directions. An example of this region is demonstrated by the 3D cube of the temperature anomaly field in the left panel of figure 4.1.

Within this confluent sub-domain, we are interested in identifying the region of frontogenetic arrest. First, we time average all available snapshots for each case after reaching an equilibrated state. Next, the pressure lines (shown in the right panel of figure 4.1) are smoothed by applying a Gaussian filter (overlaid black contours in figure 4.1). The smoothed pressure lines represent the Lagrangian coordinates for the straining front. For each field (e.g. temperature and velocities) we convert to the new coordinate system of smoothed pressure lines in the along-front direction. We examine the along-front direction and identify when the cross-front temperature gradient remains unchanged, this region is defined as the arrest region. In most runs the arrest region is about the top third of the confluent region, which is demonstrated by fairly straight lines in the smoothed along-front pressure lines in figure 4.1. Over this region, we smooth each field in the along-front (along-pressure) direction and obtain the mean fields (denoted by $\bar{\cdot}$). Figures 4.2-4.6 show the 2D cross-frontal profiles of the temperature anomaly field $\overline{\theta} - \theta_0$, the along-front velocity $\overline{u}$, cross-front velocity $\overline{v}$ and vertical velocity $\overline{w}$.

The perturbation flux terms are defined as the deviation from the mean by using the same method as in Bodner and Fox-Kemper (2020), where, as an example for the vertical flux, $\overline{w'b'} = \overline{wb} - \overline{w}\ \overline{b}$. Note that $\bar{\cdot}$ is not specific to the averaging operator, and can be used across the different type of simulations. This is also consistent from a Reynolds averaging perspective over the pressure lines averaging method.

The turbulent kinetic energy (TKE) and its budget are useful to consider the main drivers of turbulence in a system,

$$\underbrace{\frac{DE}{Dt}}_{\text{change in TKE}} = \underbrace{-\overline{\mathbf{u}'w'} \cdot \frac{\partial \overline{\mathbf{u}}}{\partial z}}_{\text{shear production}} + \underbrace{\overline{w'b'}}_{\text{buoyancy production}} - \underbrace{\frac{\partial}{\partial z}\left(\overline{w'E} + \frac{1}{\rho}\overline{w'p'}\right)}_{\text{transport of TKE}} - \underbrace{\epsilon}_{Dissipation} . \tag{4.1}$$

Where $E = \frac{1}{2}(u^2 + v^2 + w^2)$ is the TKE; $\rho\overline{\mathbf{u}'w'}$ are the components of the Reynolds stress vector and $\frac{\partial \overline{\mathbf{u}}}{\partial z}$ the mean shear, indicating the production of TKE due to shear in the mean current; $\overline{w'b'}$ is the turbulent buoyancy flux indicating production or destruction of TKE through buoyancy forces; $\overline{w'E}$ is the turbulent energy flux and $\overline{w'p'}$ is the pressure work flux i.e. transport of TKE due to turbulent fluctuations of the vertical velocity w' and pressure p'; ϵ is the dissipation rate

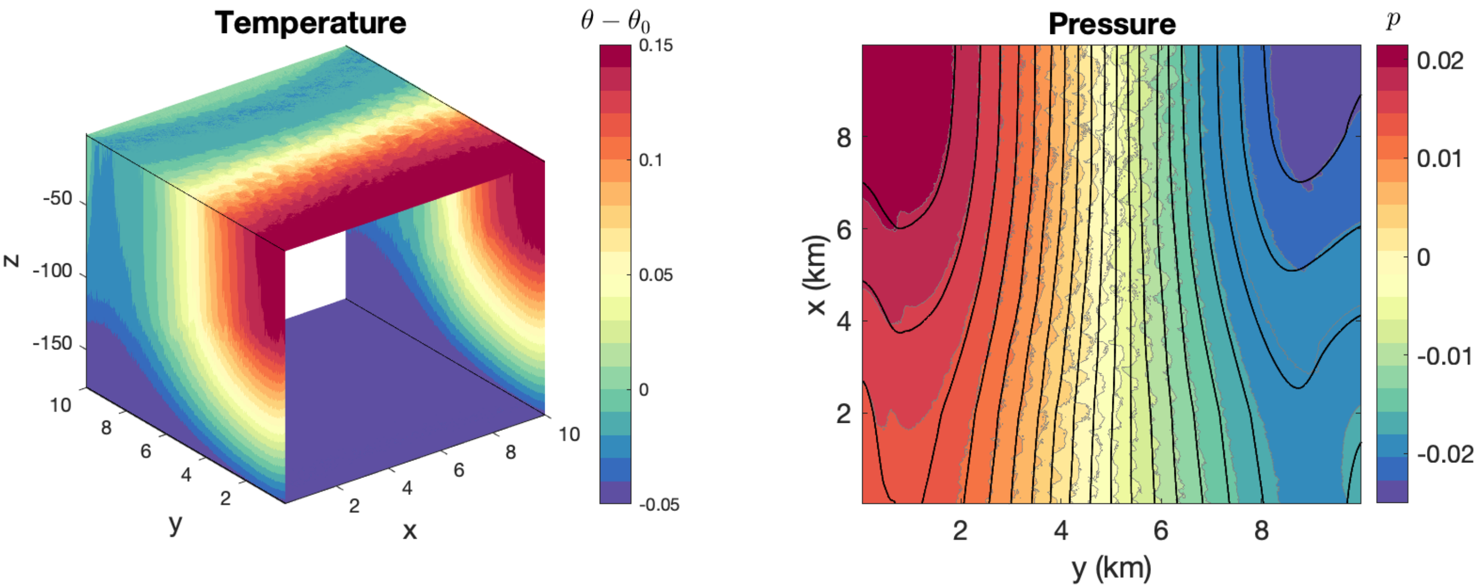

Figure 4.1: An example of the confluent sub-domain of the strain-induced front for the convection/SI case (left), and a plane view of the pressure field (contours), overlaid by the smoothed pressure lines (black) over which the along-front smoothing is calculated to obtain the mean variables displayed in figures 4.2-4.6 (right).

due to viscosity indicating destruction of TKE due to viscosity, evaluated by $\epsilon = \nu \left(\frac{\partial u}{\partial z}\right)^2$ (Sullivan et al., 1994; Grant and Belcher, 2009). The cross–frontal TKE field and vertical profiles of the TKE production and dissipation terms are shown in figures 4.7-4.11.

4.3.2 Determining frontal width

There is no clear definition in the literature for how to calculate frontal width, or how it commutes with the turbulence that sets it. Most studies approximate the buoyancy or temperature gradients across the front (e.g. Crowe and Taylor, 2020), others estimate it by a region of maximum vertical vorticity (e.g. McWilliams, 2017), or rather the extent of the overturning circulation (e.g. Suzuki et al., 2016). Similar to how the mixed layer depth is defined, there are likely several algorithms and each may prove appropriate under different circumstances.

As fronts are typically characterized by a temperature gradient at the surface, here we utilized this feature and set a quantifiable criteria for frontal width. The top 5m surface average is calculated for the temperature gradient, and the maximum gradient is evaluated and considered to be the sharpest point of the front. We estimate three possible frontal widths based on their distance from the front maximum, which corresponds to the width of 1%, 10%, 50% of the maximum temperature gradient. These estimates of frontal width are represented by black bars on the temperature anomaly profiles in figures 4.2-4.6, and their respective frontal width L_f is listed in the figures and in table 4.2. Note that the importance of being consistent with the exact definition of frontal width is demonstrated by how L_f varies widely between 1% and 50% of the surface temperature gradient maximum.

Case	$L_{\nabla\theta}^{1\%}$	$L_{\nabla\theta}^{10\%}$	$L_{\nabla\theta}^{50\%}$
Convection	137	1074	5313
Small MLI	352	1797	5234
Stokes and Wind	371	1250	3398
No Forcing	898	2832	6582
All Forcing	98	430	3652

Table 4.2: Estimated frontal widths (in meters) for each case, based on the distance from the front maximum determined by 1%, 10%, 50% of the maximum temperature gradient.

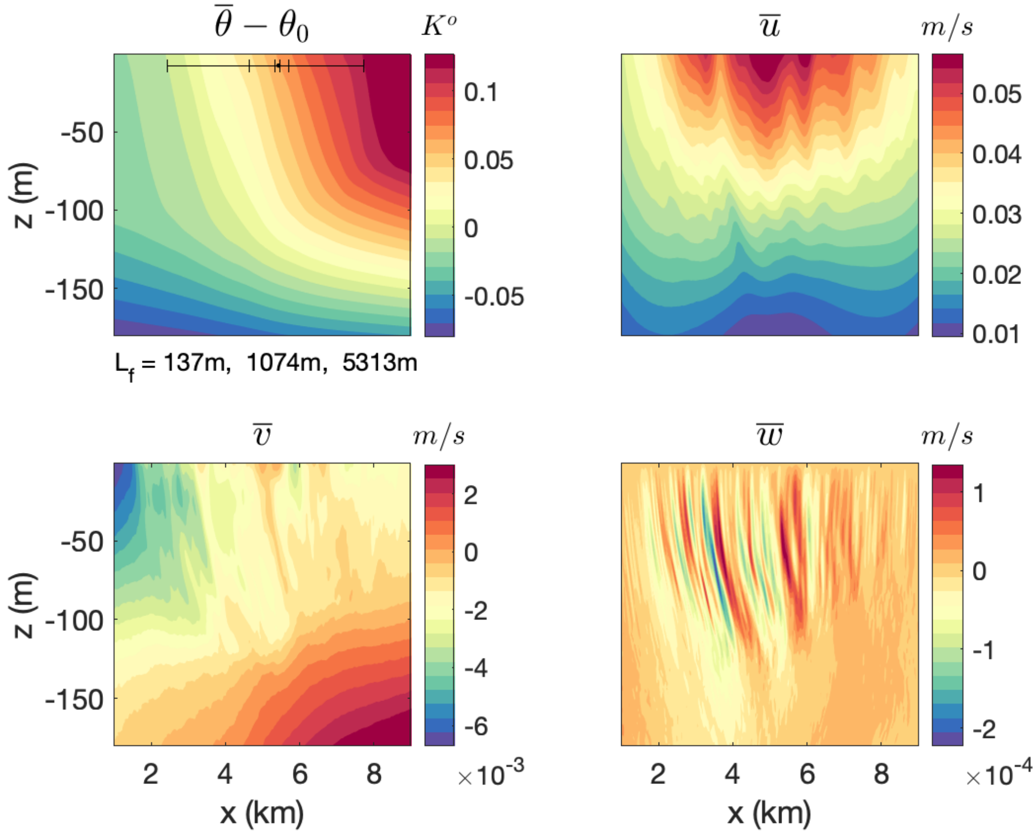

Figure 4.2: Cross-frontal mean fields for the convection/SI case: temperature anomaly $\overline{\theta} - \theta_0$ (top left), along-front velocity $\overline{u}$ (top right), cross-front velocity $\overline{v}$ (bottom left) and vertical velocity $\overline{w}$ (bottom right). Black bars and the L_f values below the mean temperature panel correspond to $L_{\nabla\theta}^{1\%}$, $L_{\nabla\theta}^{10\%}$ and $L_{\nabla\theta}^{50\%}$ from table 4.2.

4.3.3 Other relevant parameters

Several other dimensional and dimensionless parameters give insight to flow and turbulent properties of each case.

First, there are three different layers to diagnose:

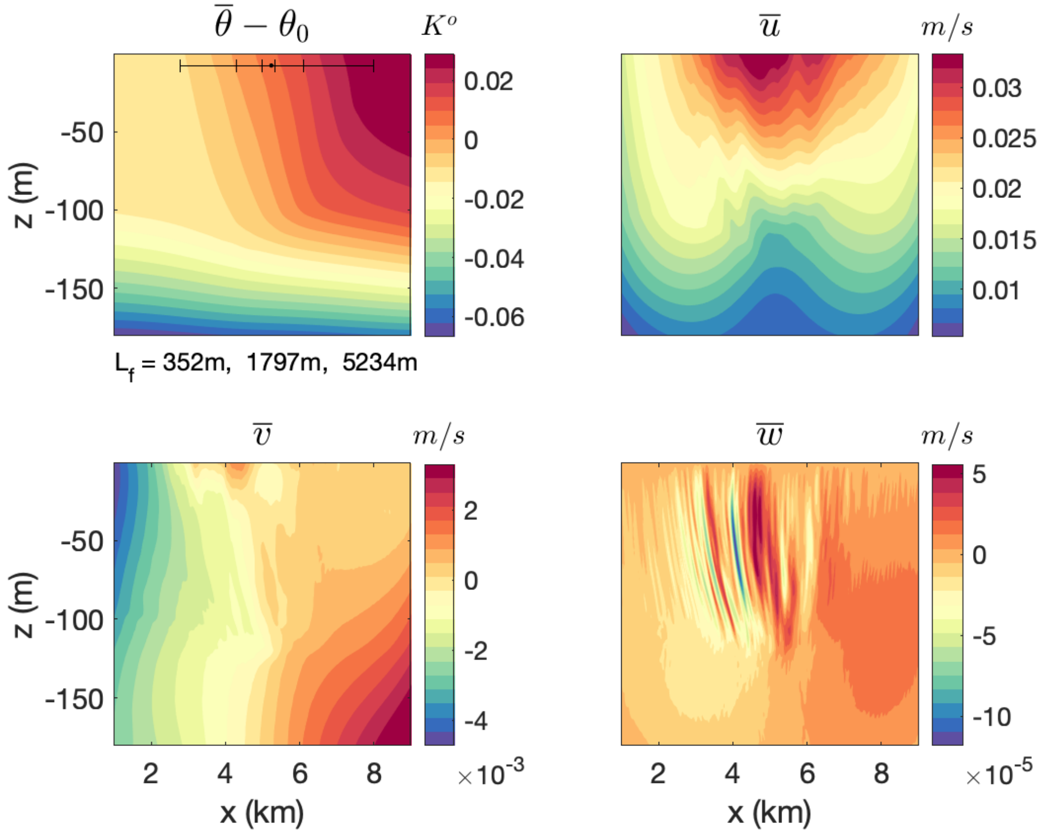

Figure 4.3: Same as in figure 4.2 for the MLI case.

1. Mixed layer depth H_θ: defined as the depth of maximum vertical temperature gradient as suggested by (Li et al., 2019), averaged over the maximum frontal region corresponding to the frontal width of $L^{1\%}_{\nabla\theta}$.

2. Mixed layer depth based on PV (H_q) which is similar to H_θ in most cases, except for the convection/SI case, where it expected to be deeper because PV is homogenized by SI. Here we follow Hamlington et al. (2014) and define the depth at which PV exceeds the critical value of $q_c = 8 \times 10^{-11} s^{-3}$.

3. Mixing layer (or boundary layer) depth h: depth at which the majority action of turbulence has occurred. Specifically, we define this as the average depth of active turbulent fluxes over the frontal region, i.e. depth of 90% of total TKE.

The along-front mean velocity characteristic scale U, is calculated by the surface averaged (top 5m) along-front velocity, averaged once more over the arrested frontal region. The Rossby number can then be estimated by $Ro \equiv \frac{U}{fL_f}$, using the sharpest frontal width $L_f = L^{1\%}_{\nabla\theta}$ for each case. The turbulent Richardson number $Ri \equiv N^2h^2/U^2$ is estimated from the shear within the boundary layer

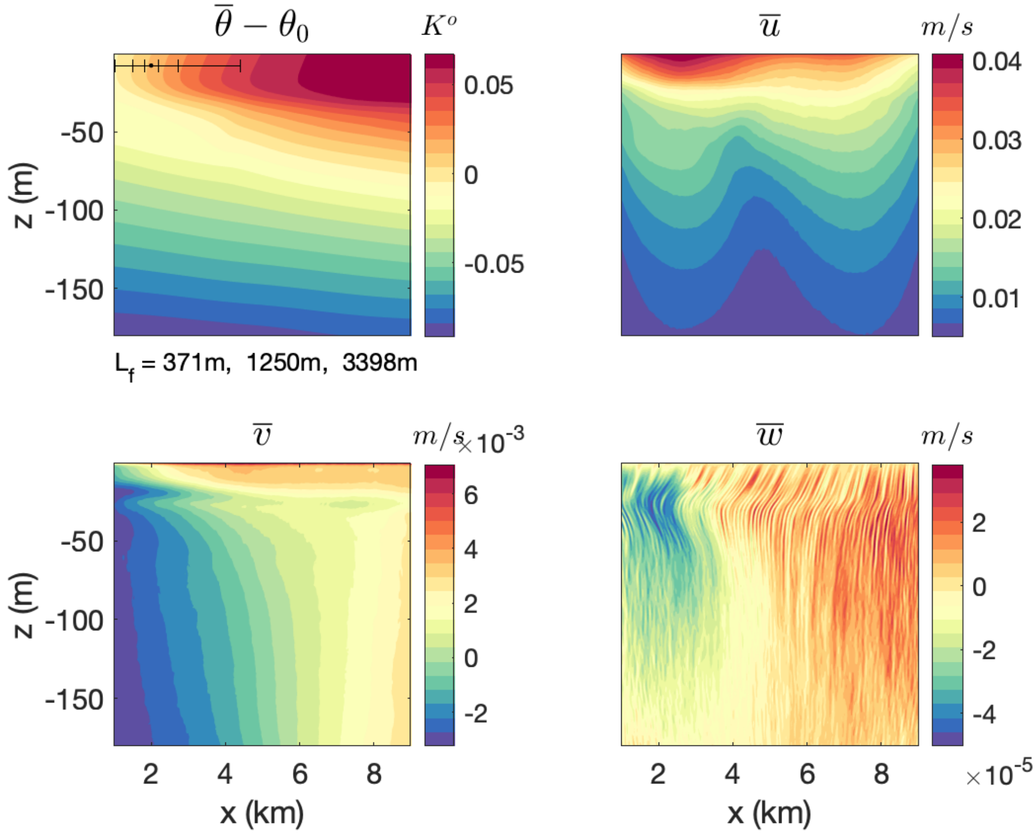

Figure 4.4: Same as in figure 4.2 for the mixed layer instability for the Stokes+wind case.

(not the mixed layer), i.e. $\partial \mathbf{u}/\partial z \sim U/h$. This is primarily because we are focused on understanding the turbulent effects on frontal arrest, which come in through the boundary layer depth.

In standard fluid dynamics, several dimensionless parameters are used to measure the scale of turbulent forces relative to inertial or planetary forces. The most common is the Reynolds number, which represents the ratio of inertial forces to viscous forces $Re = UL/\nu$, for a turbulent viscosity ν, the Ekman number represents the ratio of viscous forces to rotation $Ek = Ro/Re = \nu/h^2 f$, and the Prandtl number represents the ratio of viscous forces to diffusive forces $Pr = \nu/\kappa$ for a turbulent diffusivity κ (Vallis, 2017).

If we assume eddy viscosity and diffusivity turbulence closures such as,

$$\overline{\mathbf{u}'w'} = -\nu\frac{\partial \mathbf{u}}{\partial z} \ , \quad \overline{u'v'} = -\nu\frac{\partial u}{\partial x} \ , \quad \overline{w'b'} = -\kappa\frac{\partial b}{\partial z}, \tag{4.2}$$

we can define the Ekman, Reynolds and Prandtl numbers as,

$$Ek \equiv \frac{\overline{\mathbf{u}'w'}}{hfU} \ , \ Re \equiv \frac{U^2}{\overline{u'v'}} \ , \ Pr \equiv \frac{hN^2\overline{\mathbf{u}'w'}}{U\overline{w'b'}}. \tag{4.3}$$

Where the flux terms $\overline{\mathbf{u}'w'}, \overline{u'v'}, \overline{w'b'}$ are taken as a single values, estimated by a double average over the frontal region and top 5m.

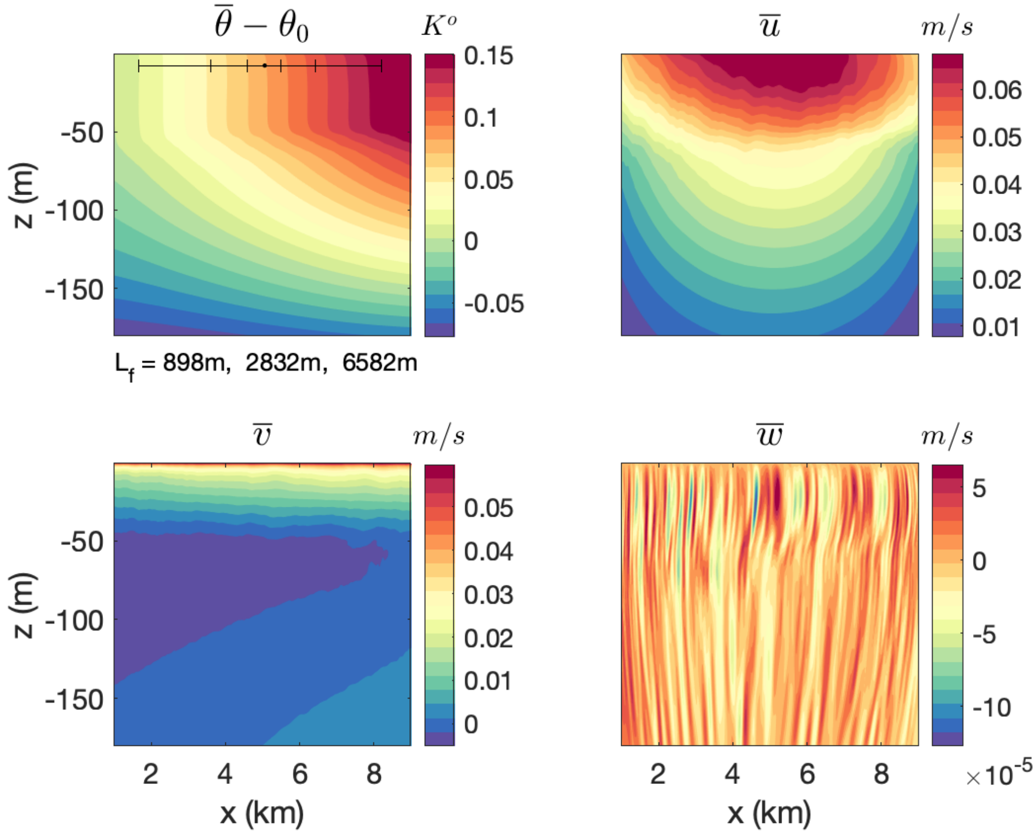

Figure 4.5: Same as in figure 4.2 for the all forcing case.

A summary of the values of these parameters for each case is given in table 4.3, and the results are discussed in the following section.

4.4 Summary of Results

As demonstrated in table 4.3, the Rossby number in all cases is $O(1)$, as expected for the submesoscale. The Ekman number is very small in all cases, but this is likely related to how $\overline{u'w'}$ are calculated: in a standard Ekman layer, the Ekman depth scales with the wind stress– i.e. is directly related to $\overline{u'w'}$– and thus Ek is expected to be close to 1. However, here we want to remain consistent among all cases for which we defined the boundary layer in terms of the TKE, and not the Ekman layer depth. Furthermore, the Ekman number (as well as the Reynolds and Prandtl numbers) may be sensitive to the domain over which we are averaging the flux terms, but as will be shown in the following chapter, it is most important to remain consistent.

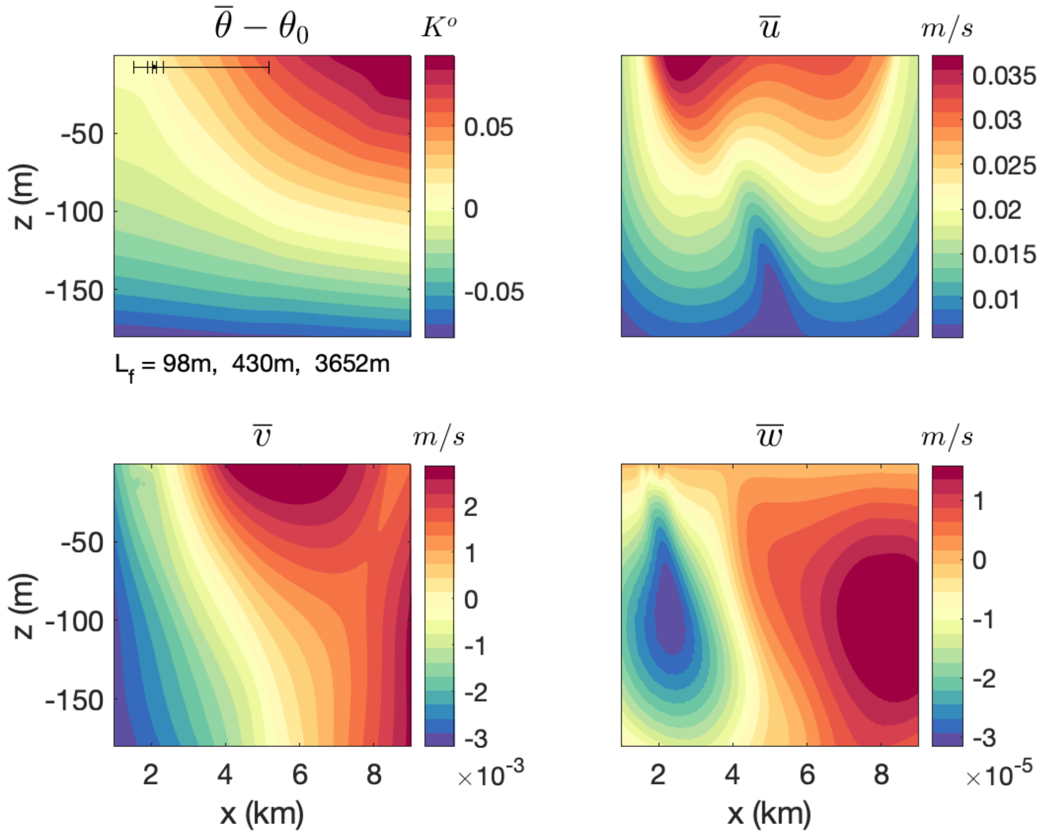

Figure 4.6: Same as in figure 4.2 for the no forcing case.

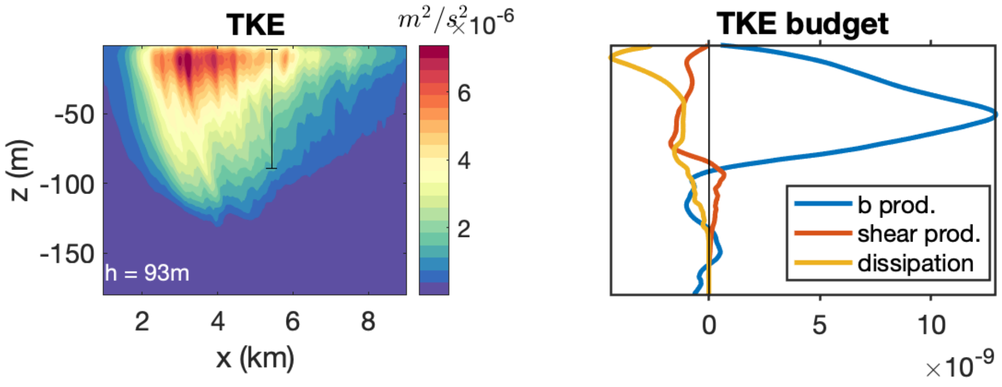

Figure 4.7: Cross-frontal mean total TKE for the convection/SI case (left), and its TKE production and dissipation terms (right) averaged over the frontal region. The vertical gray line and the corresponding value of h below illustrate the boundary layer depth estimated by the depth over which 90% of the TKE has occurred. In the right panel, b prod. and shear prod. refer to the buoyancy and shear production terms from the TKE budget, respectively.

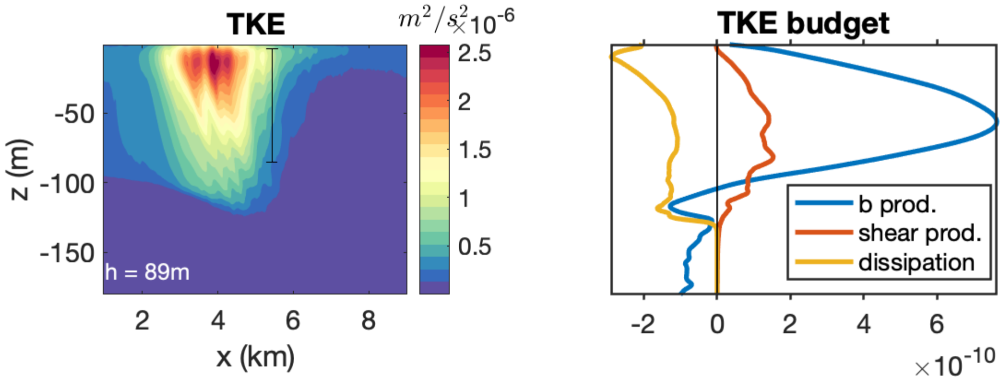

Figure 4.8: Same as in figure 4.7 for the MLI case.

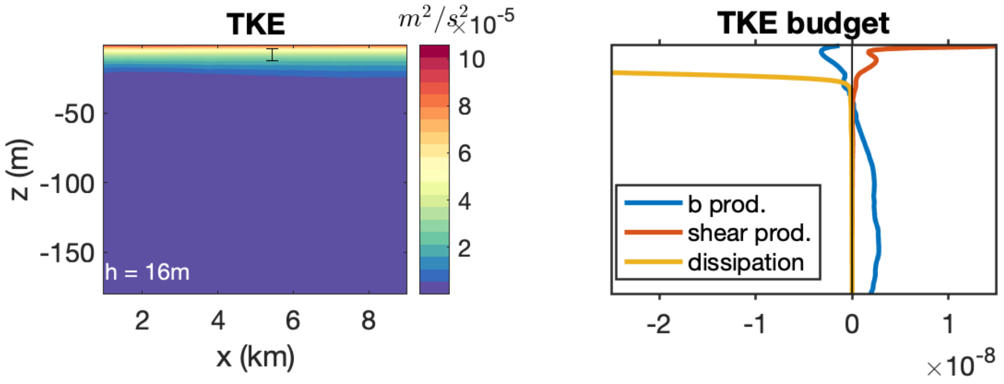

Figure 4.9: Same as in figure 4.7 for the Stokes and wind case.

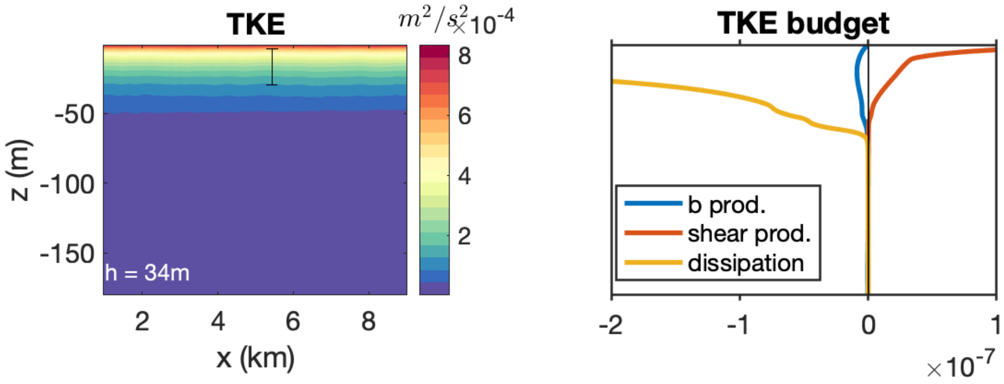

Figure 4.10: Same as in figure 4.7 for the all forcing case.

4.4.1 Convection/Symmetric Instability Case

Aside from the no forcing case, the convection/SI case results in the sharpest frontal width, with $L^{1\%}_{\nabla\theta} = 137$m. However, the front has a large spread, and becomes quite wide if $L^{50\%}_{\nabla\theta} = 5313$m is used instead (top left panel in figure 4.2). The along-front velocity $\overline{u}$ is strongest at the surface,

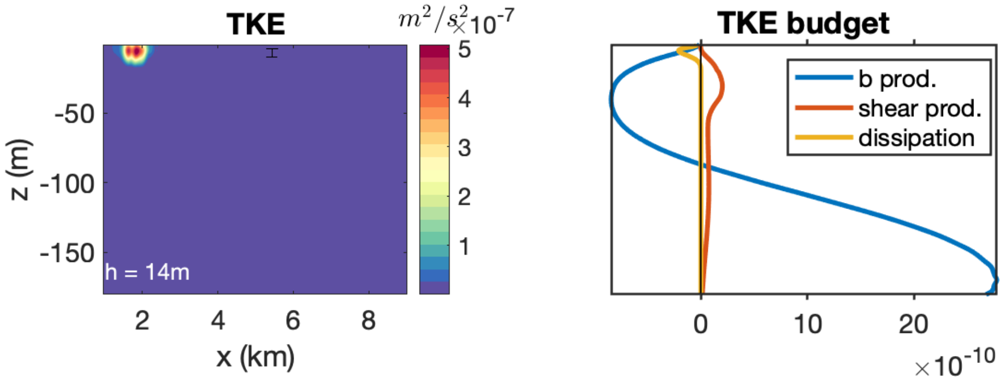

Figure 4.11: Same as in figure 4.7 for the no forcing case.

Case	h	H_θ	H_q	U	Ek	Ro	Ri	Re	Pr
Convection/SI	92.96	115.79	121.33	0.05	0.02	5.40	2.98	12.81	1.17
Small MLI	89.06	103.41	106.44	0.03	0.01	3.14	7.27	15.10	11.29
Stokes and Wind	16.40	14.45	18.375	0.03	0.08	1.44	0.17	3.43	0.70
No Mixed Layer	14.06	–	–	0.03	0.01	4.89	0.16	23.54	0.26
All Forcing	33.59	49.21	51.56	0.07	0.17	1.05	0.23	17.01	1.98

Table 4.3: Estimate of simulation parameters over arrest region: boundary layer depth h, mixed layer depths defined by temperature and PV criteria $H_{\theta,q}$, along-front characteristic velocity scale U, turbulent Ekman number $Ek \equiv \frac{\overline{u'w'}}{hfU}$, Rossby number $Ro \equiv \frac{U}{fL_f}$, turbulent Richardson number $Ri \equiv N^2h^2/U^2$, turbulent Reynolds number $Re \equiv \frac{U^2}{\overline{u'v'}}$ and turbulent Prandtl number $Pr \equiv \frac{hN^2\overline{u'w'}}{U\overline{w'b'}}$.

with a maximum value of 0.05 (top right panel in figure 4.2). The cross-frontal velocity $\overline{v}$ is mostly positive at the bottom right of the panel, and negative at the top, corresponding to the top and bottom of the mixed layer, and hinting of an overturning circulation associated with frontogenesis (bottom left panel in figure 4.2). There are also strong vertical velocities near the front maximum which may be enhanced by the overturning circulation and vertical heat fluxes (bottom right panel in figure 4.2). Note that the vertical velocity field is quite noisy, which might be partially due to fluctuations in the along-front direction as a result of the along-front smoothing operator.

We find that in the convection/SI case there is a tilted mixed layer bottom, because of the asymmetry due to frontogenesis, which is further enhanced by vertical turbulenct fluxes. In this case we re-scale the vertical coordinate as z/H, where H is the mixed layer depth. In boundary layer turbulence Monin-Obukhov theory, each column is independent of its neighboring coordinates. By re-scaling z, we make the cross-frontal region consistent across y (the cross-frontal axis) and examine turbulent properties across this region.

As expected, the mixed layer depth using the PV criteria is deeper than that using the temperature criteria (table 4.3), primarily because PV is homogenized during the process of SI (which mixes along isopycnals). The Rossby number and Richardson numbers are $O(1)$ which are expected for submesoscales and symetric instability (e.g. Thomas et al., 2013). The Prandtl number is larger than 1, indicating that convective turbulence is at similar magnitude to shear at the surface, as is also expected in this convective case.

The total TKE is fairly spread out, but strongest near the front maximum (left panel of figure 4.7), giving a boundary layer depth of $h = 93$m. The TKE budget (right panel of figure 4.7) confirms that buoyancy production is the main source of TKE. There is non-zero shear production that may be instantaneous or associated with frontogenesis. Note that we do not expect to form a closed budget, as these profiles are not averaged over the full domain and sponge layers are no included in the budgets.

4.4.2 (Small) Mixed Layer Eddies Case

The features in the cross-frontal profiles of temperature and velocities in the MLI case (figure 4.3) are very similar to those in the convection/SI case. However, in this case, the front is wider and the along-front and vertical velocities are weaker. The cross-front velocity exhibits similar frontogenesis-like features, with negative velocity of the top left corner and positive on the bottom right, attempting to slump the front. In the MLI case, the boundary layer depth and mixed layer depths are a little shallower than in the convection/SI case. The Richardson number is still $O(1)$ but fairly large, indicating this is a different regime.

MLIs have an overall restratifying effect, and so are expected to have large and positive heat flux, $\overline{w'b'}$. This is confirmed by the strong positive buoyancy production term in the TKE budget shown in figure 4.8. The large Prandtl number probably represents the vertical momentum fluxes near the surface, which may be associated with frontogenesis or the MLEs. There is also a small contribution from the shear production, which may be attributed to the interactions between the MLE and fronts (Haney et al., 2015), alternatively, this may also be associated with frontogenesis. Furthermore, MLI are growing in magnitude, carrying away the extracted potential energy to be dissipated elsewhere in the flow. This explains why the buoyancy production terms is much larger than dissipation in this location, i.e. far from equilibrium.

4.4.3 Wind and Stokes Force Case

This case presents very effective surface mixing, as the mixed layer appears to be very well mixed, visible by the vertical density lines near the surface and uniform TKE in figures 4.4 and 4.9. The Stokes + wind case has the smallest boundary layer and mixed layer depths ~ 15m, and all velocities appear to be confined to this small layer. The cross-frontal velocity $\overline{v}$ exhibits opposite signs to those in the convection and MLI cases, yet is consistent with the shear driven by the winds and waves at the surface in the y (cross-frontal) direction. However, the vertical velocity signs are consistent with what is expected for the frontogenetic overturning circulation. Interestingly, the location of the front maximum appears to have drifted to the left, which may be a result of frontogenesis interacting with the winds and waves.

The TKE budget is consistent with the standard shear driven mixing budget, where all the production in the mixing layer can be attributed to shear. Buoyancy appears to be dissipating energy below the mixed layer, which may be attributed to internal waves, and can be interpreted as vertical stratification being removed by dissipation, i.e. entrainment. Note that the magnitude of the shear production terms and total TKE is at least one magnitude larger than in all other cases.

4.4.4 All Forcing Case

The all forcing case is very similar to the Stokes+wind case but on a larger magnitude. The mean fields in figure 4.5 exhibit a well mixed layer, although it extends deeper, and the frontal width in this case is widest, where even the narrowest estimate gives a frontal width of $L_{\nabla\theta}^{1\%} = 898$m. Additionally, the vertical velocity in this case is very noisy, possibly due to the intense mixing by all forcings combined. The TKE budget in figure 4.10 exhibits the strong shear production and mixing, but on a larger magnitude than in the pure Stokes and wind case. Even though MLI and surface cooling are forcing this case as well, and produce TKE through the buoyancy production term, the total buoyancy production is negative because winds and waves are dominating.

4.4.5 No Forcing Case

The no-forcing no-mixed layer case arrives at the sharpest frontal width, with $L_{\nabla\theta}^{1\%} = 98$m, but with a very wide spread giving an estimate of $L_{\nabla\theta}^{50\%} = 6582$. Furthermore, there are characteristics of frontogenesis both in the velocity profiles and the TKE budget (shown in figures 4.6 and 4.11). However, the TKE is orders of magnitude smaller than in all other cases, since there is no turbulence included in the simulations.

4.5 Arrested Filament Frontogenesis

Sullivan and McWilliams (2018, 2019) (SM hereafter) conducted similar experiments for a range of LES, simulating a filament with varying surface forcing conditions. Specifically, they examined the process of frontal formation, arrest and decay of a turbulent-induced (TTW) cold filament in the presence of wind stress, convection and waves.

Here we compare the strain-induced results discussed above with the seven cases analyzed in SM: C denotes simulations with surface cooling; N,E denote simulations driven by down-filament and cross-filament winds respectively; and lower case n, e denotes the same for the direction of surface waves. An example of a typical simulation is shown in figure 4.12 for the E+e case, which displays the vorticity and all velocity fields. Note that although the filament exhibits fluctuations in the along-front direction (visible in the vertical velocity in figure 4.12, panel c), averaging in the along-front direction in these simulations simply requires averaging in y. An example of the cross-filament temperature field, after an along-front averaging, is given in the bottom right panel of figure 4.13 for

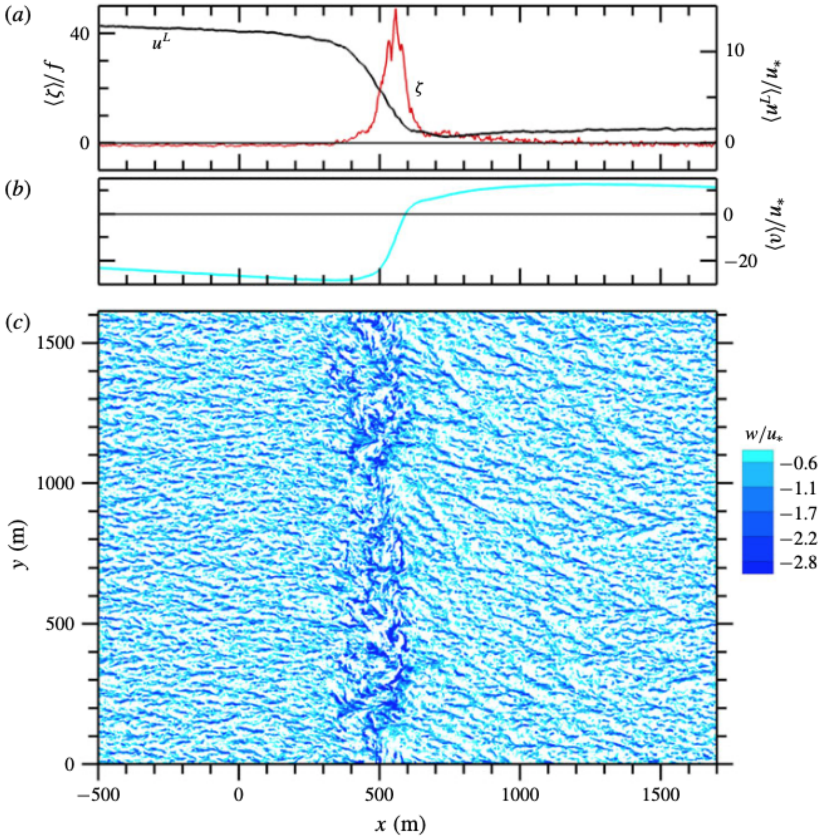

Figure 4.12: The cross-filament variation of the average vertical vorticity normalized by the Coriolis parameter $\langle \zeta \rangle / f$ (red) and average cross-filament Lagrangian current $\langle u^L \rangle / u_*$ (black) shown in panel (a), the average along-filament current $\langle v \rangle / u_*$ normalized by the friction velocity scale $u_* = 0.01 m/s$ (cyan) in (b). The vorticity and currents are near the water surface $z \sim -5m$. Instantaneous downwelling velocity $w/u_* < 0$ in a horizontal plane at $z = -10.5$ m, (c). Results are for simulation $E + e$ from SM. Figure and caption are adapted from Sullivan and McWilliams (2019).

the pure convection case (C). Figures 4.13 and 4.14 display the upper 5m average of the temperature anomaly in the cross-filament direction for all cases during the time of peak frontogenesis, identified by maximum vertical vorticity in Sullivan and McWilliams (2018).

We use the same method as in the strain-induced LES to determine frontal width, by estimating the distance between 1%, 10%, 50% of the maximum temperature gradient and the front maximum. However, since this is a filament, which can also be described in a sense as two symmetric fronts (e.g. figure 1.4), this results in two frontal widths, on both sides of the front maximum. All estimates are listed in table 4.4, and the corresponding sharper estimates (which tend to be on the left side) are those displayed in the figures.

The boundary layer here is estimated using the maximum gradient method, which searches for the maximum temperature gradient along each vertical column, and averaged over the sharpest

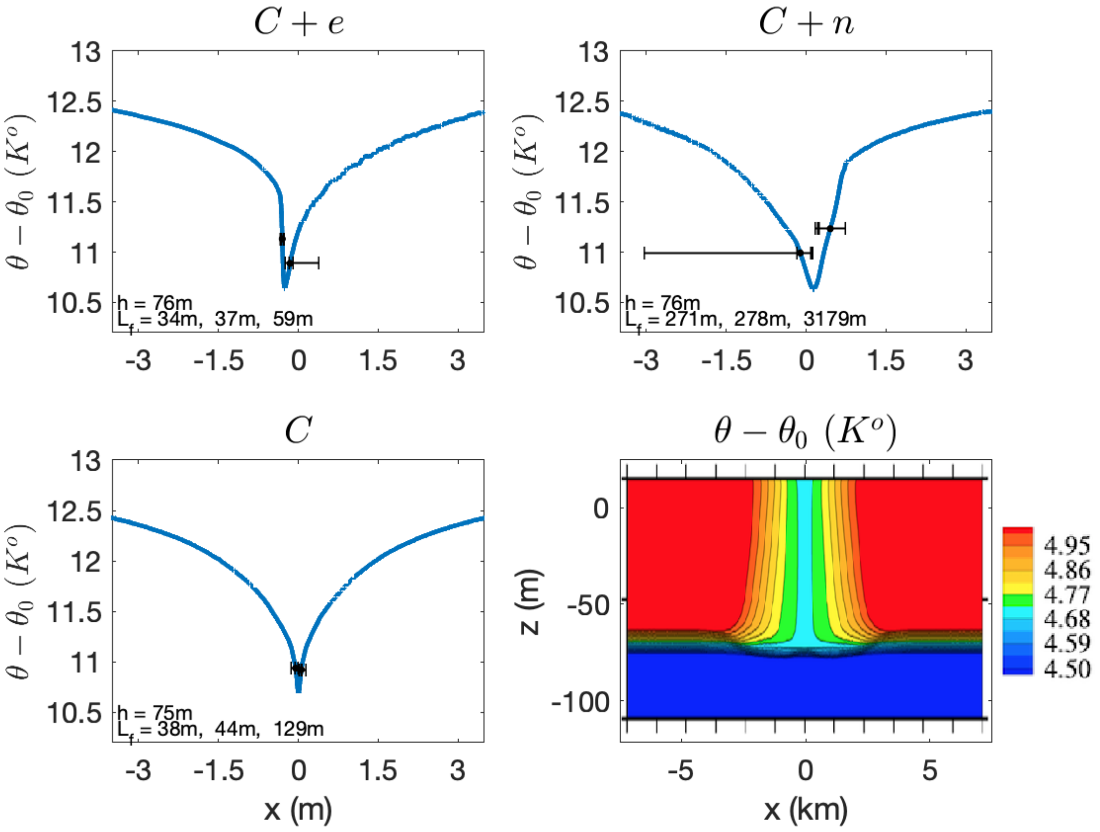

Figure 4.13: Upper 5m average of the temperature anomaly in the cross-filament direction for the SM cases associated with convection: C+e (top left), C+n (top right), C (bottom left) and a typical cross-filament profile of the temperature anomaly in the pure convection case (bottom right). The Black bars in the surface temperature plots and L_f, h listed below correspond to sharper values of $L_{\nabla\theta}^{1\%}$, $L_{\nabla\theta}^{10\%}$ and $L_{\nabla\theta}^{50\%}$, and the boundary layer depth, as listed in table 4.4.

frontal region. For each case the boundary layer depth is listed in the figures, and in table 4.4. This is essentially similar to the method used to calculate the mixed layer depth in the strain-induced LES above, which was found to be in the same order of the boundary layer depth in most cases.

Many interesting interactions between boundary layer turbulence and filament frontogenesis are documented by SM. Most importantly for our purposes, and as may be expected, filament TTW frontogenesis results in narrower frontal widths than in the strain-induced cases above. Winds and waves affect the symmetry of the frontal width, as well as the spread among the different estimates, e.g. $L_{\nabla\theta}^{1\%}$ vs $L_{\nabla\theta}^{50\%}$. SM find that filament arrest is induced by horizontal shear instability that generates horizontal momentum flux. This is consistent with some of the arrested strain-induced frontogenesis LES (specifically when winds and waves are present), for which the Richardson number is found to be below 0.25, indicative of horizontal shear instability.

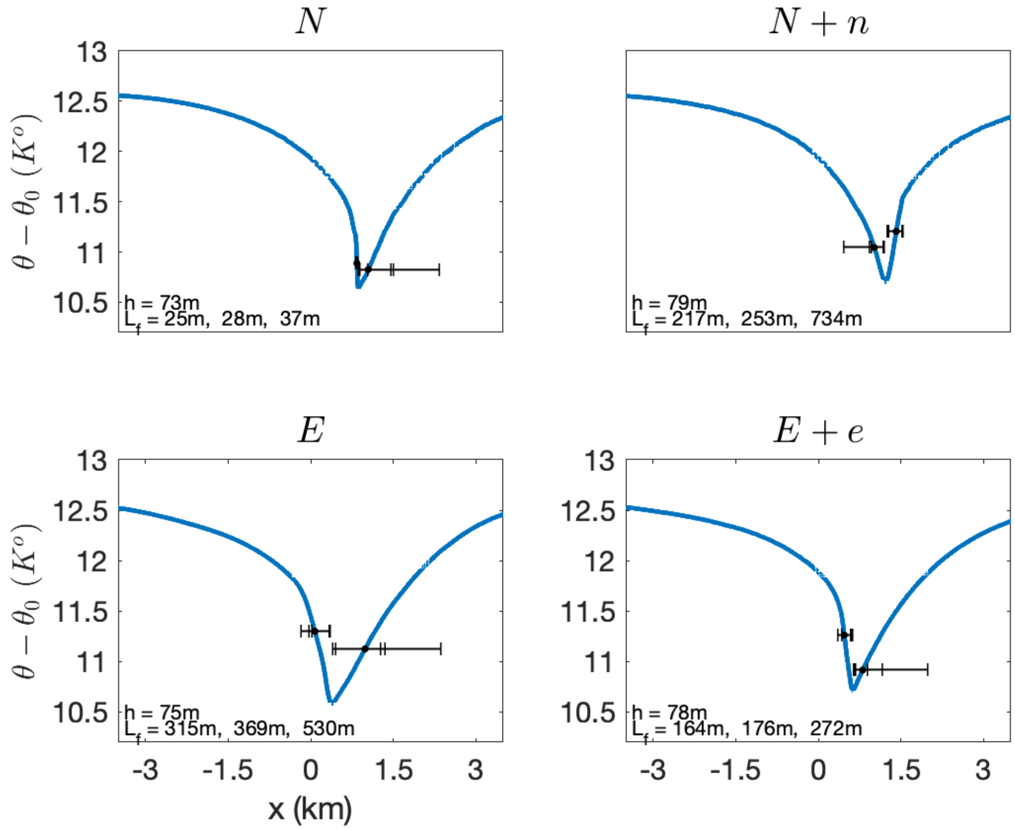

Figure 4.14: Similar to figure 4.13 for the SM wind cases: N (top left), N+n (top right), E (bottom left), E+e (bottom right).

4.6 Summary and Discussion

Theoretical work on frontogenesis has been useful in understanding why there are so many fronts and filaments in the ocean and atmosphere, but it has been less successful in predicting the scale at which these fronts will appear in realistic environments. Observations have shown that many ocean fronts occupy the submesoscale range of scales–roughly 100 m to 10 km–yet models of fronts almost always arrive at widths determined by the grid scale or sub-grid parameterizations rather than resolved phenomena. Thus, the discretized form of the singularities of frontogenesis theory (Hoskins and Bretherton, 1972) appear in models as well. Such singularities are an unphysical outcome, and do not resemble observations without unrealistically large diffusivity and viscosity (e.g. Nakamura, 1994; Blumen and Piper, 1999).

To better understand the mechanisms that enable frontogenetic arrest, a suite of LES spanning the submesoscale and into the boundary layer turbulence scale are carried out and analyzed. These simulations produce a strain-induced front in the presence of realistic surface forcing to isolate

Case	$L_{\nabla\theta}^{1\%,l}$	$L_{\nabla\theta}^{1\%,r}$	$L_{\nabla\theta}^{10\%,l}$	$L_{\nabla\theta}^{10\%,r}$	$L_{\nabla\theta}^{50\%,l}$	$L_{\nabla\theta}^{50\%,r}$	h
C	38.08	45.41	43.94	48.33	128.90	131.83	74.68
$C+e$	33.69	83.49	36.62	147.94	48.59	641.60	75.51
$C+n$	270.99	499.51	278.32	518.55	3178.7	568.35	75.55
N	24.90	445.31	27.83	609.37	36.62	1463.4	73.11
$N+n$	216.79	235.83	253.41	246.09	733.88	279.78	78.89
E	314.94	802.73	369.14	899.41	530.27	1951.2	75.38
$E+e$	165.06	219.72	175.78	492.18	272.46	1359.4	78.21

Table 4.4: As in table 4.2 for the SM cases. The first three columns represents the estimated frontal widths (in meters) on the left and right sides (noted by l, r superscripts), based on the distance from the front maximum determined by 1%, 10%, 50% of the maximum temperature gradient; The last column is the boundary layer depth.

control parameters and study their ability to arrest the front. It is found that a variety of boundary layer processes–winds and waves, convection, and mixed layer instabilities–may compete with frontogenesis.

To generate statistics, the simulations are averaged in time and over smoothed pressure lines that follow fluid motion in the along-front direction. An arrested frontal width is identified for each case and its width is approximated by distance from the maximum temperature gradient, which is defined as the front maximum. Three widths are identified as the distance between the $1\%, 10\%, 50\%$ temperature gradient from its maximum. The boundary layer depth was defined as the depth at which 90% of the TKE has occurred. The no forcing case exhibits the sharpest frontal width, which emphasizes that in the absence of turbulent forcing, frontogenesis will proceed until artificial grid scale effects arrest the front.

The energy sources for each run are very different, and the TKE budget production and dissipation terms are analyzed for each case. In the MLI and convection/SI cases, buoyancy fluxes are important which also corresponds to $Ri > 1$ (but still order 1). In other cases, shear is more important than buoyancy which results in $Ri < 0.25$. The Stokes+wind case has strong shear production, so much so that it is the dominant source of TKE in the all forcing case as well.

Finally, we compare with cold filament turbulent-induced frontogenesis simulations by Sullivan and McWilliams (2018, 2019) in the presence of winds, waves and convection. Frontal width was computed for all cases, where it is found to arrive at much sharper scales than those in the strain-induced simulations. In the following chapter these results will be utilized to test a new scaling for a turbulent-dependent frontal width.

Chapter 5

Modifying the Mixed Layer Eddies Parameterization: Frontal Width Determined by Boundary Layer Turbulence

This chapter is in preparation for submission as: Abigail S. Bodner, Baylor Fox-Kemper, Leah Johnson, Luke P. Van Roekel, James C. McWilliams, Peter P. Sullivan, & Paul S. Hall. "Modifying the Mixed Layer Eddies Parameterization to Include Frontogensis and Frontal Arrest by Boundary Layer Turbulence."

5.1 Introduction

Many aspects of submesoscales and boundary layer turbulence were discussed in previous chapters, and all have relevant impacts on local and global scales. However, the most direct impact of these processes on the climate system is through the mixed layer, and how the mixing-restratification balance at the surface helps determine its depth.

In General Circulation Models (GCMs), the restratification process associated with submesoscales is represented by the mixed layer eddies (MLE) parameterization, which captures the effects of baroclinic mixed layer eddies that form along submesoscale fronts in a weakly stratified background state i.e. the mixed layer (Nurser and Zhang, 2000; Boccaletti et al., 2007; Fox-Kemper et al., 2008).

The MLE parameterization is given in the form of an eddy-induced overturning streamfunction, which represents the slumping of the front and release of available potential energy (always positive, i.e. restratifying). The streamfunction produces fluxes and an eddy induced velocity ($\mathbf{u}^{MLE}$) which are solved by the GCM,

$$\overline{\mathbf{u}'b'} = \mathbf{\Psi}_{MLE} \times \nabla \bar{b}, \quad \mathbf{u}^{MLE} = \nabla \times \mathbf{\Psi}_{MLE}. \tag{5.1}$$

Fox-Kemper et al. (2008) derive the theory for the MLE parameterization and arrive at the following formula for the MLE streamfunction $\mathbf{\Psi}_{MLE}$,

$$\mathbf{\Psi}_{MLE} = C_e \frac{H^2 \nabla_H \overline{b^z} \times \mathbf{z}}{|f|} \mu(z) \tag{5.2}$$

Where H is the mixed layer depth, f the Coriolis parameter, $\nabla_H \bar{b}^z$ is the depth averaged horizontal buoyancy gradient over the mixed layer, $0.06 \leq C_e \leq 0.08$, and the vertical structure function is approximated by:

$$\mu(z) = \max\left(0, \left[1 - \left(\frac{2z}{H} + 1\right)^2\right] \left[1 + \frac{5}{21}\left(\frac{2z}{H} + 1\right)^2\right]\right) \tag{5.3}$$

Which causes the parameterization to vanish below the mixed layer, i.e. when $z < -H$.

Implementing the parameterization in coarse resolution climate models introduces a grid scale Δs and a frontal width L_f parameter. These arise from statistically estimating the number of unresolved fronts in a single grid cell by applying the submesoscale spectral slope of k^{-2} (Fox-Kemper et al., 2011). Thus, the MLE streamfunction that is solved by GCMs is given by,

$$\mathbf{\Psi} = C_e \frac{\Delta s}{L_f} \frac{H^2 \nabla_H \bar{b}^z \times \mathbf{z}}{\sqrt{f^2 + \tau^{-2}}} \mu(z) \tag{5.4}$$

The substitution of $f \to \sqrt{f^2 + \tau^{-2}}$ has often been used to renormalize across the equator, when $\tau \sim h/u_*$ is available instead, where h and u_* are the boundary layer depth and friction velocity (also defined in table 5.1).

The parameter for frontal width has traditionally been a constant in some models (e.g. Modular Ocean Model, MOM) taken as some value in the range $L_f = 500m - 2km$, whereas in other models (e.g. Parallel Ocean Program, POP) it has been taken as:

$$L_f = \max\left(\frac{NH}{|f|}, \frac{\nabla_H \bar{b}^z H}{f^2}, L_{f,\min}\right) \tag{5.5}$$

where $L_{f,\min}$ is an artificial limiter to ensure stability, NH/f is the mixed layer deformation radius, which were based on estimates of frontal width suggested by observations and geostrophic frontal adjustment theory (e.g. Tandon and Garrett, 1994; Hosegood et al., 2006). Furthermore, stratification is not a robust measurement in most GCMs, and accurately defining N from boundary layer mixing schemes can be difficult (e.g. Li et al., 2019). This is a primary reason for the second formulation in (5.5), which anticipates the deformation radius after geostrophic adjustment has occurred (i.e., assumes $Ri = N^2 f^2 / |\nabla_H \bar{b}^z|^2 \sim 1$).

However, over the past decade, several studies have shown these assumptions to be overly restrictive on the one hand, as argued by Calvert et al. (2020) that due to a natural cancellation of the NH/f formulation, the cutoff $L_{f,\min}$ is not needed. On other hand, this scaling has been shown to be too simplistic, especially in the presence of surface forcing, such as winds and convection (e.g. Mahadevan et al., 2010; Callies and Ferrari, 2018).

In chapter 2 and Bodner et al. (2020) the effects of turbulence on frontal formation were explored in a theoretical framework in the quasi-geostrophic limit. Vertical turbulent fluxes were found to enhance frontogensis whereas horizontal fluxes are able to oppose it. In the submesoscale limit, a Turbulent Thermal Wind (TTW) balance has been found to be a useful framework for understanding the onset of frontogenesis in the presence of boundary layer turbulence. In this framework, vertical turbulent fluxes incite frontogensis whereas shear instability is responsible for the arrest process (McWilliams et al., 2015; Sullivan and McWilliams, 2018, 2019). These studies have set the scene for a more physically based estimate of frontal width, one that incorporates the complex interactions between fronts and boundary layer turbulence that help set this scale. In this study we develop and test a new scaling motivated by these principals.

Section 5.2 presents the new frontal width scaling that relates L_f with surface forcing parameters. Based on TTW theory, this scaling highlights key aspects of frontogenesis and frontogenetic arrest. Section 5.3 tests the new scaling using the estimates from the Large Eddy Simulations (LES) described in chapter 4 and data from the General Ocean Turbulence Model (GOTM). Results and impacts of the new parameterization implemented in the Community Earth System Model (CESM) are discussed in section 5.4. Summary and discussion are given in 5.5.

5.2 A new scaling for frontal width

Following McWilliams et al. (2015), we define the horizontal shear vector as

$$s(z) = \frac{\partial \mathbf{u}_H}{\partial z} \tag{5.6}$$

In the TTW balance, the horizontal buoyancy gradient $\nabla_H b(z)$, balances the shear term together with the viscous term $\frac{\partial^2(\nu\ \mathbf{s})}{\partial z^2}$ generated by surface wind stress τ^s:

$$\nabla_H b = -f\hat{\mathbf{z}} \times \mathbf{s} + \frac{\partial^2(\nu\ \mathbf{s})}{\partial z^2}. \tag{5.7}$$

The buoyancy gradient variance equation for $|\nabla_H b|^2$ can be extended from the TTW balance equations, where all cross terms cancel out due to vector identities,

$$|\nabla_H b|^2 = |f\hat{\mathbf{z}} \times \mathbf{s}|^2 + \left|\frac{\partial^2(\nu\ \mathbf{s})}{\partial z^2}\right|^2. \tag{5.8}$$

We next use scale analysis to explore this equation and the horizontal scale that sets this three-way balance.

The Buckingham Pi theorem helps establish the potential relationship among a set of dimensional parameters. The number of dimensional parameters can be reduced by converting to dimensionless parameters and making appropriate empirical assumptions. A total of 10 dimensional parameters

Vertical momentum flux	$\overline{u'w'}$	Mean horizontal velocity	U
Vertical buoyancy flux	$\overline{w'b'}$	Turbulent friction velocity	$u_* = \sqrt{\tau/\rho}$
Coriolis parameter	f	Turbulent convective velocity	$w_* = (B_0 h)^{1/3}$
Mixing layer depth	h	Brunt-Väisälä frequency	N
Mixed layer depth	H	Frontal width	L_f

Table 5.1: Dimensional parameters. Note that we do not need any of the thermal expansion parameters β or g, because they are represented by w_* and N. We are also assuming that Stokes drift is not a different scaling from u_* (i.e., fixed turbulent Langmuir number for fully-developed waves). The molecular viscosity ν_m and diffusivity κ_m can be suppressed assuming $Re = Uh/\nu_r \gg 1$ can neglect ν_m and $Pe = w_* h/\kappa_m \gg 1$ (e.g. Bodner and Fox-Kemper, 2020).

Rossby number	$Ro \equiv \frac{U}{fL_f}$	Richardson number	$Ri \equiv N^2h^2/U^2$
Turbulent Ekman number	$Ek \equiv \frac{\overline{u'w'}}{hfU}$	Turbulent Prandtl number	$Pr \equiv \frac{hN^2\overline{u'w'}}{U\overline{w'b'}}$
Horizontal velocity ratio	U/u_*	Turbulent velocity ratio	u_*/w_*
Mixing vs mixed layer ratio	h/H	Aspect ratio	h/L_f

Table 5.2: Dimensionless parameters, as in chapter 4

with fundamental dimensions of length and time (table 5.1) gives a total of 10-2=8 dimensionless parameters (table 5.2).

Thus, we seek a function, $\mathcal{F}$ in the form of,

$$0 = \mathcal{F}(Ro, Ri, Ek, Pr, U/u_*, u_*/w_*, h/H, h/L_f), \tag{5.9}$$

which is equivalent to finding L_f as a function of all other parameters.

In the MLE-TTW framework, we insist that all theories for submesoscales and boundary layer turbulence be consistent.

In the boundary layer, the turbulent convective velocity is defined as,

$$w_* = (B_0 h)^{1/3} \tag{5.10}$$

where $B_0 = g\beta Q_*$ is the surface buoyancy flux ($B_0 > 0$ for destabilizing conditions), g is gravity acceleration, β the thermal expansion coefficient and Q_* is the kinematic surface heat flux. And the turbulent friction (i.e., shear) velocity is defined as,

$$\mathbf{u}^* = \sqrt{\frac{|\tau_0|}{\rho_0}}, \tag{5.11}$$

where τ_0 is the wind stress and ρ_0 is a reference density. A general horizontal shear will scale as ,

$$\frac{\partial \overline{\mathbf{u}}}{\partial z} \sim \frac{U}{h} \tag{5.12}$$

Where h is the boundary layer depth, purposely left unspecified for now. It follows that the shear production scales as,

$$\overline{\mathbf{u}'w'} \cdot \frac{\partial \overline{\mathbf{u}}}{\partial z} \sim \begin{cases} u^{*2}\frac{U}{h} & \text{if } w_* = 0, \\ w^{*2}\frac{U}{h} & \text{if } u_* = 0. \end{cases} \tag{5.13}$$

In cases forced with both convection and stress, boundary layer mixing schemes such as the K-Profile Parameterization (KPP; Large et al. (1994)) and the energetics based planetary boundary layer scheme (ePBL; Reichl and Hallberg (2018)) tend to use $\overline{\mathbf{u}'w'} = (m_* {u_*}^3 + n_* {w_*}^3)^{2/3}$. In Reichl and Hallberg (2018), $m_*,\ n_*$ have specific formulas given by boundary layer turbulence. For simplicity, here we use their approximate average values, $m_*,\ n_* \approx 0.5, 0.066$, however this analysis can easily be extended to include their space and time dependent values (as calculated in the GCM).

Thus, for an eddy viscosity closure,

$$\overline{\mathbf{u}'w'} = -\nu \frac{\partial \overline{\mathbf{u}}}{\partial z}, \tag{5.14}$$

and following the definition in chapter 4, the turbulent Ekman number can be written as,

$$Ek \equiv \frac{\overline{u'w'}}{hfU} \sim \frac{(m_* {u_*}^3 + n_* {w_*}^3)^{2/3}}{hfU}. \tag{5.15}$$

We define the buoyancy scaling by vertical stratification, which can be related to the Richardson number as,

$$b \sim N^2 h = Ri \cdot \frac{U^2}{h}. \tag{5.16}$$

By setting $\mathbf{s} \sim \frac{U}{h}$, $b \sim Ri \cdot \frac{U^2}{h}$ and $\nu \frac{\partial \overline{\mathbf{u}}}{\partial z} \sim (m_* {u_*}^3 + n_* {w_*}^3)^{2/3}$, the TTW buoyancy variance equation (5.8) can now be written as,

$$\begin{aligned} |\nabla_H b|^2 &= |f\hat{\mathbf{z}} \times \mathbf{s}|^2 + \left|\frac{\partial^2(\nu\ \mathbf{s})}{\partial z^2}\right|^2 \\ \rightarrow \quad Ri^2 \cdot \frac{U^2}{f^2 L_f^2} &= 1 + \frac{(m_* {u_*}^3 + n_* {w_*}^3)^{4/3}}{U^2 h^2 f^2} \end{aligned} \tag{5.17}$$

Notice that U^2/f^2L^2 is the Rossby number squared, and the last term on the right hand side is the Ekman number squared. So equation (5.17) can also be written as,

$$Ri^2 Ro^2 = 1 + Ek^2 \tag{5.18}$$

For this three-way balance to hold, the following conditions need to be met,

1. $Ek^2 = O(1)$
2. $Ri^2 Ro^2 / Ek^2 = O(1)$
3. $Ri^2 Ro^2 = O(1)$

This reflects the fact that in the submesoscale, both boundary layer turbulence theory and geostrophic theory balance simultaneously, which is also the essence of TTW theory. In the submesoscale, the Rossby and Richardson numbers are $O(1)$. However, the first condition requires that they also vary together. This can be written as:

$$Ro \cdot Ri = c_1 \tag{5.19}$$

Where c_1 is a constant and is $O(1)$. Note that in the original MLE parameterization, L_f is the deformation radius which obeys $Bu = Ro^2 * Ri = 1$, which is different than this result.

From the second condition, h emerges as proportional to the Ekman depth, i.e. $h \propto \frac{(m_* {u_*}^3 + n_* {w_*}^3)^{2/3}}{fU}$, or $h = c_2 \frac{(m_* {u_*}^3 + n_* {w_*}^3)^{2/3}}{fU}$, where $c_2 = O(1)$.

Expanding the third condition gives:

$$\frac{RiRo}{Ek} = \frac{1}{c_3} \rightarrow Ri \cdot \frac{U}{fL} = \frac{1}{c_3} \cdot \frac{(m_* {u_*}^3 + n_* {w_*}^3)^{2/3}}{Uhf} \rightarrow L = c_3 \cdot Ri \cdot \frac{U^2}{(m_* {u_*}^3 + n_* {w_*}^3)^{2/3}} \cdot h \quad (5.20)$$

Where c_3 is a constant and is $O(1)$.

Thus, for this three-way balance to hold, the following scaling for L_f emerges:

$$\boxed{L_f = C_L \cdot \frac{(m_* {u_*}^3 + n_* {w_*}^3)^{2/3}}{f^2} \cdot \frac{1}{h}} \quad (5.21)$$

Where, $C_L = c_2^2 \cdot c_3 \cdot Ri \equiv O(Ri)$, which will be set to $Ri = 0.25$, representing the arresting mechanism of horizontal shear instability (discussed in more detail in section 5.3).

In the Buckingham Pi framework this can be written as:

$$0 = \mathcal{F}(Ro, Ri, Ek, u_*/w_*, h/L). \quad (5.22)$$

Thus, the Prandtl number and mixed layer depth parameters emerge as auxiliary to this thought process, and the frontal width is entirely independent of them. This is different than the previous form of frontal width which included the dependence on H and N.

Furthermore, as we will be making some assumptions about Ro, Ek, Ri and their relationships, it may be more intuitive to understand the scaling for frontal width as,

$$L_f = \mathcal{F}(u_*, w_*, f, h), \quad (5.23)$$

where all of these terms are readily available in most GCMs.

Including the new scaling for L_f in the streamfunction expression (5.4) yields,

$$\boxed{\mathbf{\Psi} = C_e \frac{\Delta s}{L_f} \frac{H^2 \nabla \bar{b}^z \times \mathbf{z}}{\sqrt{f^2 + \tau^{-2}}} \mu(z) \quad \Rightarrow \quad C_r \frac{\Delta s |f| h H^2 \nabla \bar{b}^z \times \mathbf{z}}{(m_* {u_*}^3 + n_* {w_*}^3)^{2/3}} \mu(z)}, \quad (5.24)$$

where $C_r = C_e / C_L$.

Note that in this new formula, τ is no longer required in the denominator because the f term cancels out. This is an important improvement not only because it eliminates an artificial parameter, but also because the new parameterization naturally vanishes at the equator, where the submesoscales are resolved (e.g. Dong et al., 2020). Furthermore, L_f no longer includes N^2, which is not a robust measurement amongst most models.

5.3 Proof of concept

5.3.1 Testing in Large Eddy Simulations

We utilize results from the two types of LES discussed in chapter 4, e.g. turbulence-induced and strain-induced frontogenesis, to test the new L_f under various surface forcing conditions (u_*, w_*), the boundary layer depth (h) and the Coriolis parameter (f). For all runs we use the average values for $m_*, n_* = 0.5, 0.066$ from Reichl and Hallberg (2018).

In the turbulent-induced filament frontogenesis cases from Sullivan and McWilliams (2018, 2019) (SM hereafter), the parameters used for surface forcing are $u_* = 0.01\ m/s$ and $w_* = 0.0137 m/s$, the Coriolis parameter is $f = 7.81 \times 10^{-5}\ s^{-1}$. and for each case we use the boundary layer depth found in chapter 4. To account for the effects of waves, we include the adjustment of $\mathcal{E} u_*$, where $\mathcal{E}$ is the enhancement factor based on Van Roekel et al. (2012), which best predicts vertical diffusivity and is most appropriate for our TTW based theory (Li and Fox-Kemper, 2017),

$$\mathcal{E} = \sqrt{1 + (3.1La)^{-2} + (5.4La)^{-4}}. \tag{5.25}$$

Where the coefficients used here are consistent with the case for aligned winds and waves, and the Langmuir number in SM is given as $La = 0.32$. Note that the enhancement factor is only applied to u_*, as Li and Fox-Kemper (2017) found it was less significant for w_*.

Of the strain-induced LES runs, we include only the convection/SI, Stokes+wind and all forcing cases (which also include small MLE). This is because the pure mixed layer instability case and the no forcing case are not forced with u_*, w_*, necessary to compute the new frontal width scaling. In the Stokes+wind case, $u^* = \sqrt{\tau_0/\rho_0} = 0.001\ m/s$ and we apply the enhancement factor $\mathcal{E} u_*$ using the Langmuir number $La = \sqrt{u_*/u_s} = 0.223$ where $u_s = 0.2$ m/s. In the convection/SI and all forcing cases, we have penetrating short wave solar radiation in addition to surface cooling. Thus, we use the formula from equation (8) in Mironov et al. (2002), which combines them into a convective velocity scale w_R,

$$w_R = [-(h - \delta) B_R]^{1/3}, \tag{5.26}$$

where δ is the depth at which the vertical temperature gradient is zero (i.e. maximum), and h is the boundary layer depth.

Horizontal shear instability is found to be associated with frontogenetic arrest, where $Ri < 0.25$ in most strain-induced cases in chapter 4 and as discussed in Sullivan and McWilliams (2018, 2019) and Bodner et al. (2020). Hence, we set the Richardson number in the frontal width scaling to match the frontogenetic arrest physics: $Ri = 0.25$. Furthermore, as shown in table 5.3 the constants $c_1,\ c_2, c_3$ are confirmed to be of order 1 in the strain-induced LES. Thus, we choose to set the constant $C_L = Ri = 0.25$.

Figure 5.1 is a log-log plot of the measured $L^{1\%}_{\nabla\theta}$ frontal width found in chapter 4 compared with the L_f prediction based on the new scaling (5.21), using the appropriate u_*, w_*, h, f for each case, and constants set to $m_*, = 0.5,\ n_* = 0.066,\ C_L = 0.25$. This demonstrates that the new L_f scaling predicts values on the same order of the measured frontal width in all cases. This also implies that

	c_1	c_2	c_3
Convection/SI	1.12	6.65	0.13
Stokes and Wind	0.64	0.82	1.88
All Forcing	2.76	3.38	0.10

Table 5.3: Estimate of parameterization constants given from strain-induced runs

even in the strain-induced frontal cases TTW balance holds to some degree. It is important to note that this is in no way a proper validation of the scaling. To improve on this would require a series of simulations (which are extremely computationally expensive), varying one parameter at a time over several orders of magnitude. Here we demonstrate plausibility over a range of available simulations.

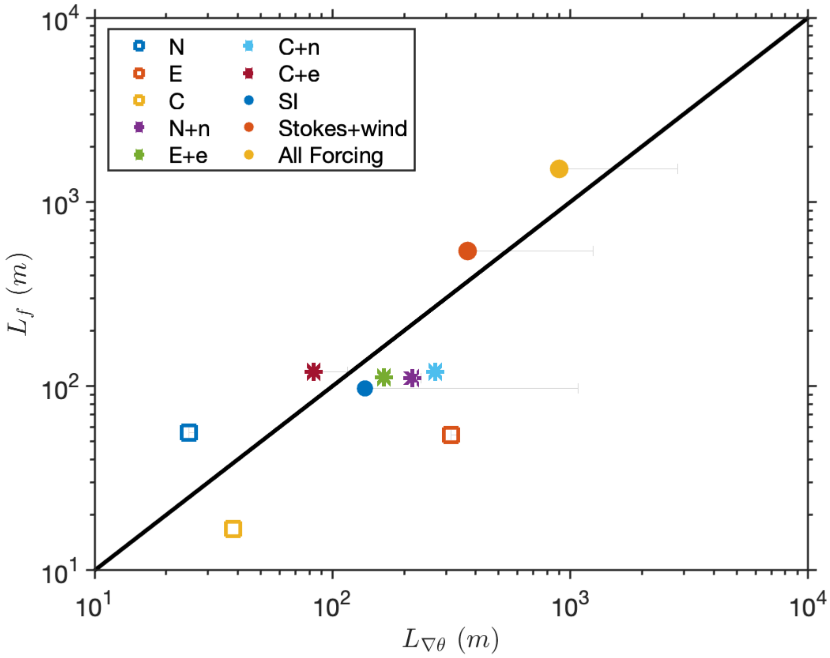

Figure 5.1: Log-log plot of the measured $L_{\nabla\theta}^{1\%}$ frontal width found in chapter 4 compared with the L_f prediction based on the new scaling (5.21), using the appropriate u_*, w_*, h, f for each case, and constants set to $m_*, = 0.5,\ n_* = 0.066,\ C_L = 0.25$. Gray error bars represent the measured frontal width given by $L_{\nabla\theta}^{10\%}$.

5.3.2 Estimates from the General Ocean Turbulence Model

The General Ocean Turbulence Model (GOTM) is typically used as a stand-alone model for studying dynamics of boundary layers in natural waters. Using mooring data available from the Monsoon Intra-seasonal Oscillations in the the Bay of Bengal project (MISO-BOB), the GOTM model is forced with 16 months of observed surface fluxes, giving u_* and w_*. GOTM estimates the boundary layer depth using the CVmix turbulence scheme which is based on the KPP parameterization, similar to

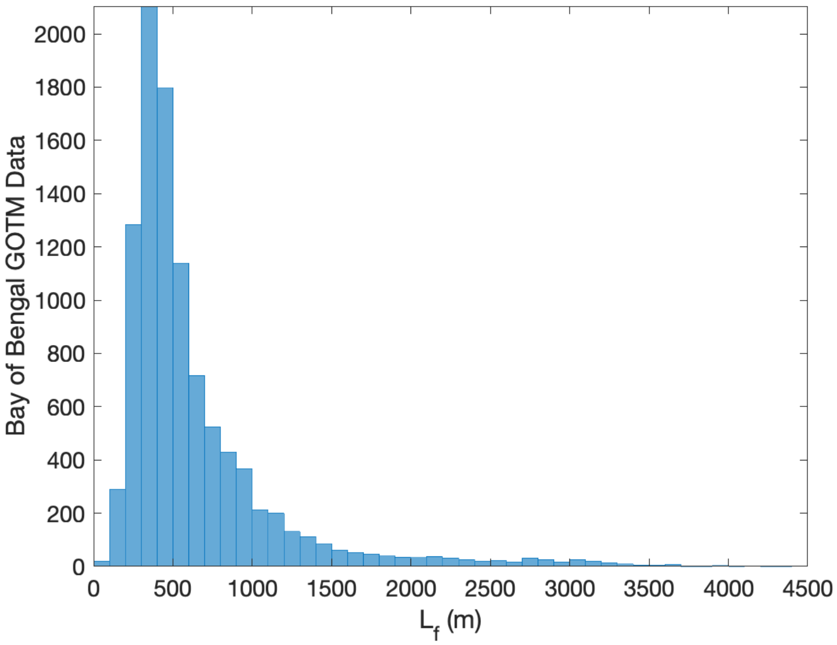

Figure 5.2: L_f (m) estimated from GOTM in the Bay of Bengal using u_*, w_* and CVmix to determine h.

the way it would be computed in a GCM (e.g. Large et al., 1994; Van Roekel et al., 2018; Li et al., 2019).

Figure 5.2 displays the range of L_f from (5.21) given by the GOTM data input. Although there is likely seasonality and other variability that might impact this distribution, the results are in the range of what may be expected from a submesoscale frontal width, centered around 500m, or more generally on the order of $O(1)$km (e.g. Lucas et al., 2016).

5.4 Implementation

We next implement the new MLE parameterization formula given by equation (5.24) in CESM2.1.3-POP, where the parameters u_*, w_*, h are all readily available from KPP, and are used for (5.24). Here as well, we set the constants $m_*, = 0.5$, $n_* = 0.066$, $C_L = 0.25$, and all other parameters are already available within the existing MLE parameterization scheme. Thus, the MLE parameterization is modified via the L_f parameters at no additional computational cost to the model.

The new parameterization was tested in two types of simulations: a global fully coupled simulation and a CORE-v2 forced ocean simulation, which covers forcing data from 1948-2009 (Large and Yeager, 2009). The fully coupled model was run for 100 years for both the new and control versions of the MLE parameterizations. The forced model was run for five cycles at a total of 310 years. The mixed layer depth climatology was obtained by averaging over the last 20 years of the coupled simulation and last cycle in the forced simulations.

Figures 5.3 and 5.4 show the mixed layer depth during summer and winter in both hemispheres respectively, from observations given by the de Boyer Montégut et al. (2004) dataset updated to include Argo data up to 2012, compared with the control and new parameterization for both the coupled and forced simulations.

Most importantly, the results appear to be qualitatively similar in all simulations, and resemble observations. This is primarily to show the sensitivity of the mixed layer depth to the new parameterization, that changes are non zero, and the parts in the world that exhibit these changes are climatically important. The differences in mixed layer depth between the control and new parameterization are highlighted by the zonal average at the top right panel of figures 5.3 and 5.4, and in figures 5.5 and 5.6 for the coupled and forced simulations, respectively. These reveal that in the coupled simulations, the new parameterization leads to deeper mixed layer depth in the southern ocean, and a shallower mixed layer depth in the equator and Indian Ocean. In the forced simulations, the southern ocean is less apparent but here again there is a significant reduction in the equator, where reducing the bias has been difficult to achieve with boundary layer mixing schemes (e.g. Li et al., 2019).

5.5 Summary and Discussion

Submesoscales and boundary layer turbulence are instrumental in modulating the transfer of heat, momentum, carbon and other properties, between the atmosphere and ocean interior. Accurate representation of these processes in models is crucial, yet they tend to be on scales smaller than the grid used, even at the highest possible resolution. The current Mixed Layer Eddies (MLE) parameterization represents the restratification process of adjusting submesoscale fronts, but it has been shown to be too simplistic and unfitting in circumstances where the frontal width effects are impactful.

Here we present a new scaling law that relates frontal width with boundary layer turbulence by building on the Turbulent Thermal Wind (TTW) balance. The new frontal width scaling utilizes variables from boundary layer turbulence schemes u_*, w_*, h which are readily available in most climate models. Furthermore, it eliminates the need for an artificial parameter τ which was designed to prevent singularities near the equator in the previous version, and it avoids the dependence on N^2 which is not always easily diagnosed in GCMs.

The new scaling also depends on the local Rossby, Ekman and turbulent Richardson numbers. Several physical assumptions were made to reduce the number of dependent variables, of which the Rossby and Ekman numbers are assumed to be 1, as expected for the submesoscale. The Richardson number is set to 0.25, representing the arrest by horizontal shear instability.

Using the suite of the Large Eddy Simulations (LES) presented in chapter 4, we test this new scaling over a variety of turbulent processes resulting from winds, waves, and convection that lead to arrested submesoscale fronts and filaments. The predicted frontal width from the new scaling is found be in the same order of the measured frontal width for all cases. Additionally, boundary layer data from the General Ocean Turbulence Model (GOTM) in the Bay of Bengal was used to estimate the possible range for the new frontal width scaling, which was found to be consistent with the submesoscale range of $O(1)$km.

The new scaling for frontal width is implemented in the MLE parameterization and tested in forced and coupled CESM2.1.3-POP simulations, where climate sensitivity was primarily estimated through the impact on the mixed layer depth. Since the new parameterization depends on surface forcing, there is merit in both types of simulations: the coupled simulations has active feedback with the atmosphere, which come back through u_* and w_* by changing mixed layer depth and sea surface temperature. The forced simulations are useful for model-observation comparison, as they are forced by observational measurements. However, the CORE-v2 dataset used here is inferior to the newer JRA55-do dataset which has recently been shown to reduce bias in mixed layer depth (Tsujino et al., 2020). Thus, future work will also include testing the new MLE parameterization in a JRA55-do forced simulation for a more robust comparison with observations.

The MLE streamfunction is stronger for sharper fronts, i.e for smaller L_f. The frontal width range found by the GOTM data in the Bay of Bengal demonstrates that the new scaling is able to arrive at smaller L_f than predicted by the previous version. This will enhance the restratification effect, which is especially important in regions where there is still a bias towards deeper mixed layer depths (e.g. equator). Indeed, this is perhaps the most significant result of the new parameterization found in both the forced and coupled simulations.

The LES analysis has demonstrated how important wave effects are, and that an enhancement factor is necessary to account for the higher diffusivity and mixing due to Langmuir turbulence. This enhancement factor is also available in turbulent mixing schemes in CESM and future work will include incorporating the effects of Langmuir turbulence in the MLE parameterization. It can be expected that the contribution of Langmuir turbulence will be most significant in the southern ocean, where wave swells tend to be large (Young, 1994; Belcher et al., 2012). However, we do not expect this to affect much the equator where waves are relatively calm.

It is important to emphasize that this study is primarily to prove plausibility, and a proper parameter analysis needs to be performed in order to validate the parameterization with simulations that are specifically designed for it. As shown in chapter 4, fronts can also be arrested by other type of turbulence not captured in the TTW framework (e.g. smaller MLEs without surface forcing). Furthermore, the stress imposed by wind effects can either lead to sharpening or spreading of the front depending on the wind direction, which is not accounted for in this framework. Recent work by Crowe and Taylor (2020) developed a scaling for an equilibrated buoyancy gradient that relates fronts and surface forcing with TTW theory in the low Rossby limit. A more comprehensive parameter search is needed to validate and compare our results with other scalings for frontal widths under different regimes (e.g. Mahadevan et al., 2010; Wenegrat et al., 2018; Crowe and Taylor, 2020).

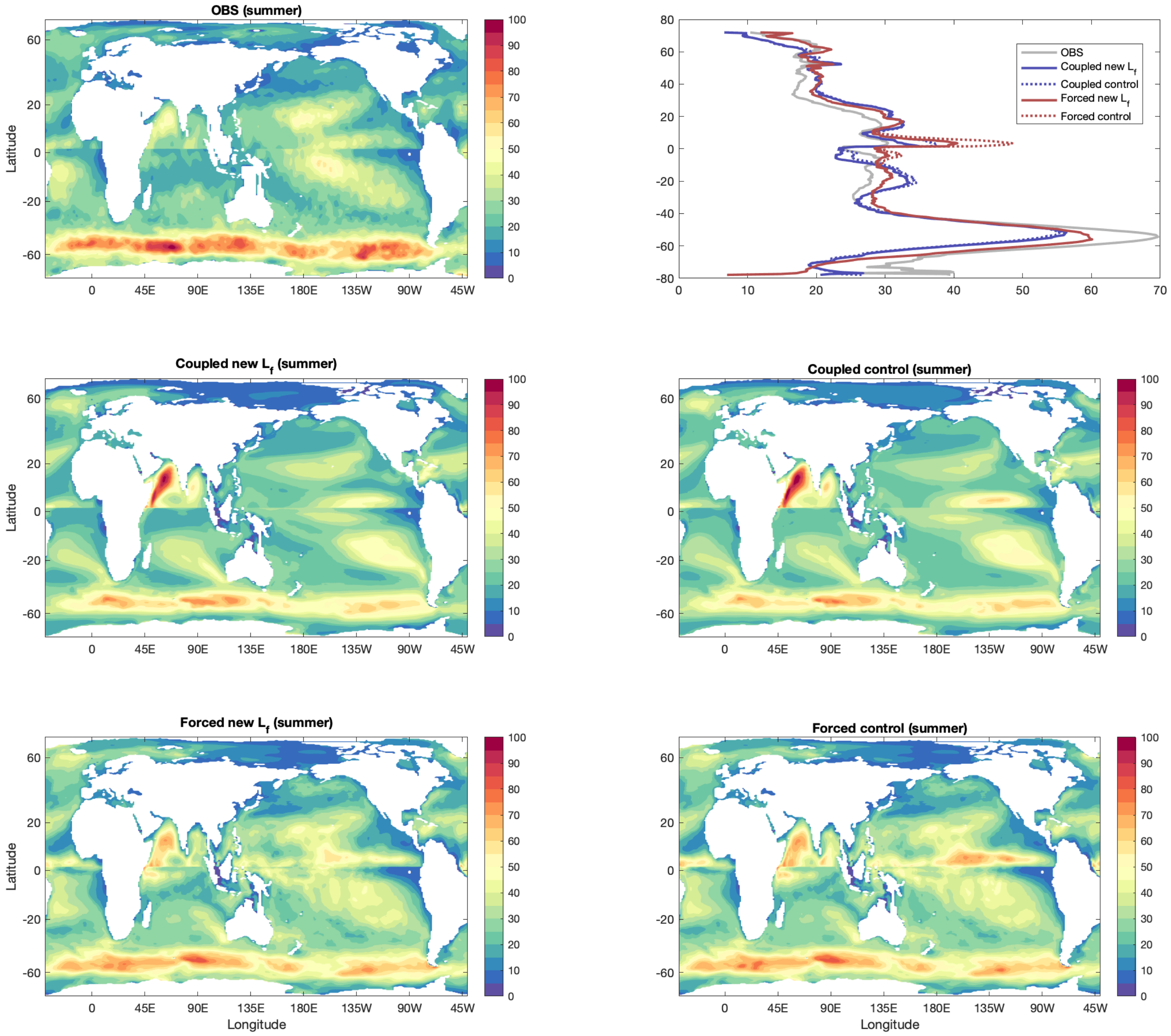

Figure 5.3: Global maps of mean mixed layer depth during summer in the Northern Hemisphere (July-September) and Southern Hemisphere (January-March) from: observations given by the de Boyer Montégut et al. (2004) dataset updated to include Argo data up to 2012 (top left), zonal average of all simulations (top right), new Lf vs control in the coupled simulations (middle panels) and forced simulations (bottom panels) .

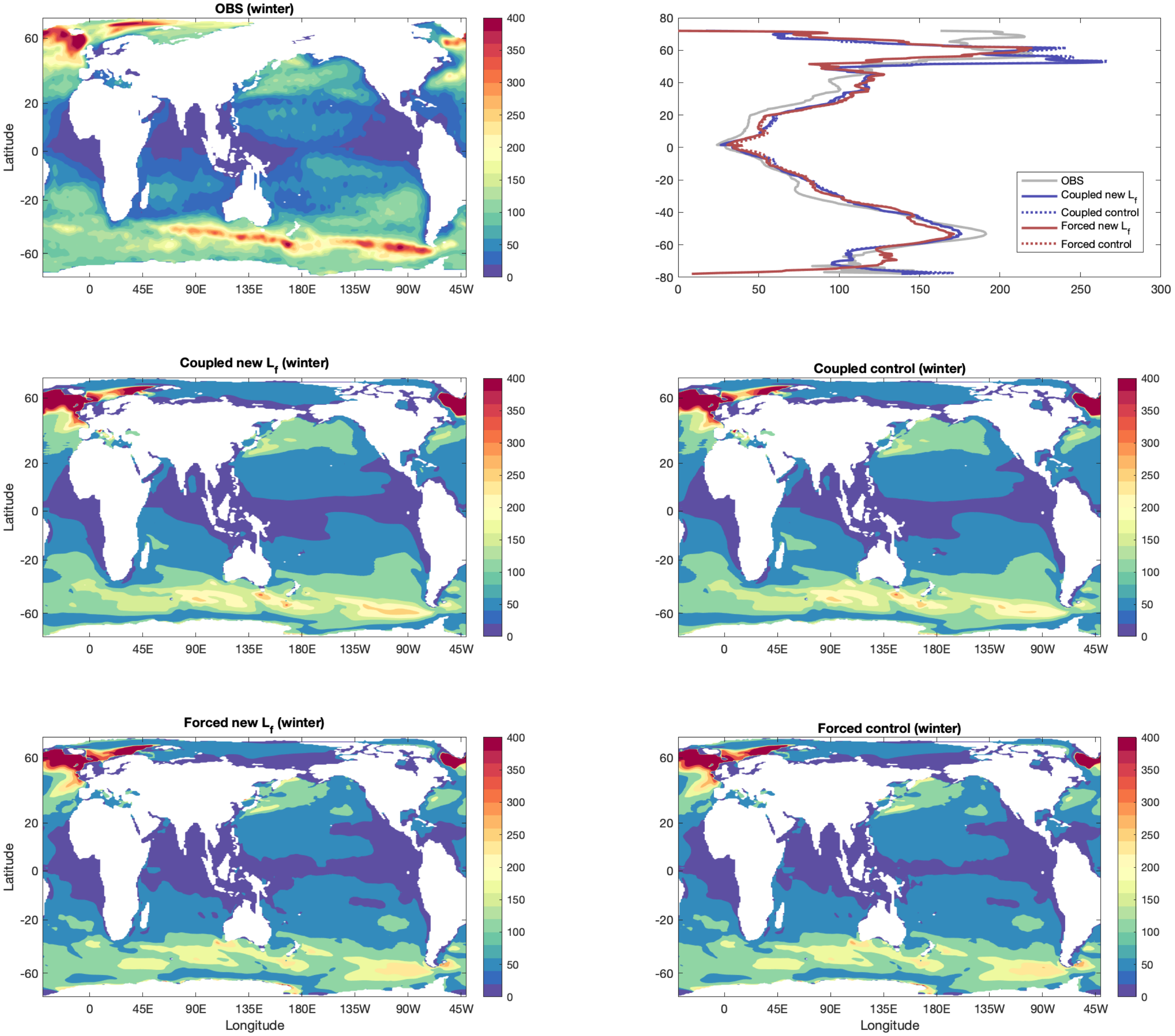

Figure 5.4: Same as figure 5.3 during winter in the Northern Hemisphere (January-March) and Southern Hemisphere (July-September).

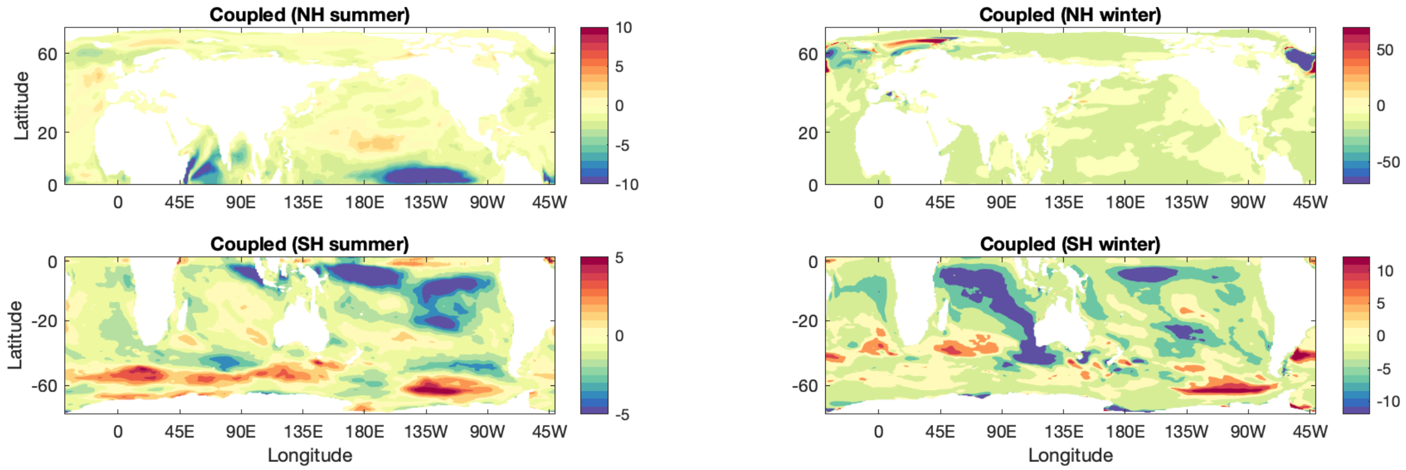

Coupled (NH summer)

Coupled (NH winter)

Coupled (SH summer)

Coupled (SH winter)

Figure 5.5: Differences between new L_f and control in the coupled simulations during summer and winter in both hemispheres, as in figure 5.3. Note the different colorbars to emphasize regional variability.

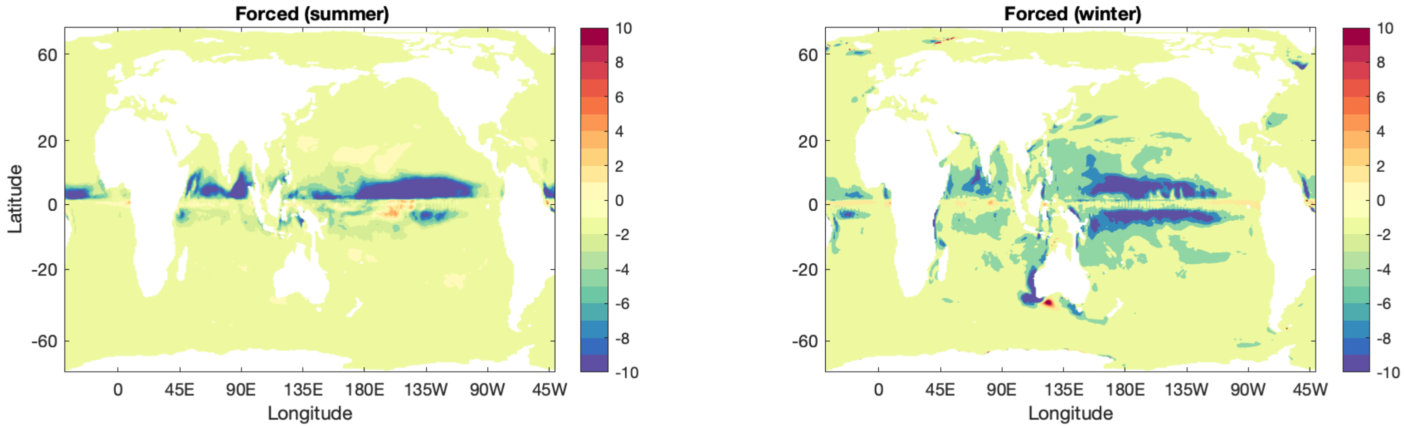

Forced (summer)

Forced (winter)

Figure 5.6: Same as in figure 5.5 for the forced simulations.

Chapter 6

Conclusions

The dynamic interplay between ocean submesoscales and boundary layer turbulence is investigated in this thesis using several theoretical and computational methods. The process of frontal formation, known as frontogenesis, and how it arrests before reaching singularity, is found to be strongly linked to the presence and properties of boundary layer turbulence. This thesis demonstrates that these effects are key to better understanding the dynamics of each regime separately, and how they vary together under the same framework. Furthermore, one of the major accomplishments of this work is quantifying these interactions to represent their effect in global circulation models (GCMs). The following section 6.1 summarizes the most significant results and conclusions from this thesis. Plans and suggestions left for future work are given in section 6.2.

6.1 Summary and Implications

- This thesis distinguishes what aspects and theories of potential vorticity (PV) are valid in the submesoscale, where stratification and rotation still govern flow dynamics to some extent, compared with a 3D turbulent regime, where isotropic turbulent properties govern the flow and any rotation or stratification are considered instantaneous. PV and PV fluxes are found to be instrumental in the theoretical framework presented in chapter 2, through which an analytic result is found when including turbulent fluxes in the semi-geostrophic equations posed by Hoskins and Bretherton (1972). Furthermore, surface quasi-geostrophy (SQG) has been argued to be a useful framework to decipher submesoscale fluid motion below the surface (e.g. Lapeyre and Klein, 2006; LaCasce and Mahadevan, 2006). This was found to be consistent with the theoretical framework in chapter 2, where surface PV fluxes, even if only given at one location where the front is strongest, are sufficient in most cases to describe the entire flow field associated with frontogenesis. However, chapter 3 revealed the limitations of PV in highly turbulent regimes, where large variance in rotation and stratification are exacerbated by subgrid closures in models such as Large Eddy Simulations (LES), where 3D turbulence is only partially resolved. This ultraviolet catastrophe penetrates PV dynamics and contaminates PV fluxes as well, unless carefully treated by proper filtering. This discovery further highlights that not only are submesoscales and boundary layer (3D) turbulence distinct in scale, but also exhibit distinct dynamical properties.

- In both weak and strong turbulent regimes, the effects on frontogenesis and frontogenetic arrest are found to be significant. Chapter 2 focuses on the early frontogenesis stage, where in the presence of a strain field, the effects of turbulence are still considered small compared to the leading order dynamics. In this framework turbulence plays an important role in determining how sharp the front can get and at what rate. It is found that all turbulent processes are able to arrest the front at early stages, however horizontal turbulent fluxes, which may represent processes such as horizontal shear, can completely diffuse the front, whereas vertical fluxes, which may represent convection for example, tend to contribute to frontal sharpening. This is somewhat confirmed by the LES analyzed in chapter 4, which represent a more realistic turbulent regime during late frontogenesis, when the front and turbulence have equilibrated and settled on an arrested scale. All cases analyzed demonstrate an arrested front resulting from a variety of turbulent processes such as winds, waves, convection and mixed layer instabilities. The scaling law in chapter 5 is based on turbulence-induced frontogenesis by turbulent thermal wind balance (TTW), and is found to predict a frontal width that is on the same order as estimated directly from the simulated arrested fronts. This demonstrates that vertical fluxes can also play a role in the formation of the front, even in strain-induced simulations.

- As mentioned above, a common thread throughout this thesis is that vertical turbulent fluxes, such as those expected near the ocean surface, are found to be significant in all forms of analysis. This further confirms that TTW theory is a useful framework to understand submesoscale fronts and their interaction with vertical turbulent fluxes in the ocean surface boundary layer. Furthermore, horizontal fluxes, and presumably horizontal shear, is one of the primary arrest mechanisms in both strain and turbulent-induced frontogenesis. These aspects of frontal formation and arrest help determine the effective frontal width. The scaling for frontal width described in chapter 5 builds on these findings and provides a formula based on TTW and a Richardson number reflective of horizontal shear. The new scaling links turbulent properties computed by vertical mixing schemes with the mixed layer eddies (MLE) parameterization in GCMs, which is found to have successful preliminary results in sensitivity and bias reduction of the mixed layer depth in key regions of climatic importance. The full impact on the climate system and future work to improve this parameterization is discussed further in the following sections.

6.2 Future Work

6.2.1 Dominant frontal arrest mechanism

Although this thesis concluded that the most relevant arrest mechanism is horizontal shear instability, it also showed evidence that other turbulent processes can arrest the front (e.g. small MLE), and some observations also indicate frontogenetic arrest without specific mechanism (e.g. Ledwell et al., 1993; Kersalé et al., 2016). The analysis in chapter 4 highlighted that among the possibilities are horizontal shear instability, convection and symmetric instability, mixed layer eddies on a smaller scale, wind shear and wave effects. Dong et al. (2020, 2021) estimate the scale of symmetric and mixed layer instabilities globally, yet on a local scale it is presently unclear if one dominates over the other and if one is more likely to occur if both conditions are favorable.

The Richardson number parameter in the new frontal width scaling is representative of the arrest mechanism. If the front is arrested before reaching horizontal shear instability, the Richardson number could be on order 1 or larger, which may result in frontal widths much larger than currently predicted. Furthermore, if symmetric instability is an important arrest mechanism, it is expected that the MLE parameterization commute with the symmetric instability parameterization and mixing properties given by Bachman et al. (2017b).

Finally, the new scaling for frontal width was tested using LES of arrested filament frontogensis, which was treated as a two-sided front for the purposes of this thesis. However, the dynamics of filaments have been shown to be different in several aspects, especially in the presence of winds and waves (e.g. Suzuki et al., 2016; Sullivan and McWilliams, 2018, 2019). The current MLE parameterization represents the restratifying process of a slumping front, yet MLE may also form along submesoscale filaments if there is sufficient available potential energy stored in the vertical isopycnals. How significant this is, how likely this occurs in nature and whether the MLE parameterization need to be modified to include these effects is left for future work.

6.2.2 Further improvements on the Mixed Layer Eddies Parameterization

Most of this section is based on personal communication with Alistair Adcroft (GFDL) and Baylor Fox-Kemper regarding implementing the new version of the MLE parameterization in MOM6.

Future versions of CESM will primarily include the Modular Ocean Model (MOM6) developed by GFDL. This model includes the ePBL mixing scheme which allows the use of the precise values of m_*, n_* in the frontal width scaling, as well as the standard u_*, w_*, h as in the current KPP-based version. Including these parameterizations will be an improvement on the current version, which only uses the average values from Reichl and Hallberg (2018).

In MOM6 the mixed layer depth H is currently calculated as a resetting running mean of the boundary layer h, with a time-scale longer than a day. This captures the rapid deepening and shoals more slowly so the restratification can continue working at depth.

To avoid instantaneous restratification or hypersensitivity to boundary layer turbulence on shorter timescales, it may be desirable to form the ratio expression $r_* = h/(m_* u_*^3 + n_* w_*^3)^{2/3}$ and run it through a filter $\langle r_* \rangle$. h and $(m_* u_*^3 + n_* w_*^3)^{2/3}$ should (in theory) vary together, so combining them into a ratio expression could also help with any arising singularities. h is time evolving, thus this type of filtering helps avoid sensitivity to instantaneous changes in surface forcing, yet will not affect the MLE streamfunction as Fox-Kemper and Ferrari (2009) demonstrated the MLE outlive changes in vertical mixing that occur on a diurnal cycle . Furthermore, defining minimum values for u_*, w_* to ensure the model remains stable in the weak turbulence regime can be done by using values appropriate for molecular turbulence (of water) e.g. $[u_*^3]_{min} \sim 1e-9$ as a lower limit, which is the absolute smallest fronts can get. A possible time average filter is of the timescale for evolution of the turbulent kinetic energy (TKE) and heat flux budgets, which can be estimated from the ratio of the eddy diffusivity or viscosity to the TKE: $t_f \approx \kappa/TKE$ or $t_f \approx \nu/TKE$ (Wyngaard, 2010). In ePBL, the TKE is explicitly predicted as are the instantaneous κ and ν. Finally, the effects of waves should be included through the enhancement factor for u_* and is also available from the ePBL scheme (Reichl and Li, 2019). This will complete the link between frontal width and all types of surface forcing (e.g. winds, waves, convection) in the scaling law derived in chapter 5. Estimating the full impact on the climate system is left for future work, as will be explained in the following section.

6.2.3 Effects on Climate

Quantifying the sensitivity of any process to perturbations in local and global climate, and how this change may return to affect the general climate is complex and depends nonlinearly on other components of the climate system. Chapter 5 focuses on the effects of the new MLE parameterization on the mixed layer depth, which gives the most direct impact on climate sensitivity (e.g. Tsujino et al., 2020; Hall and Fox-Kemper, 2021). However, there are several other metrics of significant broader climatic impacts that should be evaluated. These include air-sea fluxes and gas exchanges such as CFCs for the impact on the biogeochemical cycle, surface and subsurface tracers such as temperature and salinity, "ideal age" for the effect on ventilation pathways of different water masses below the mixed layer, and on the global scale through the meridional overturning circulation, deep water formation and average global temperatures.

Finally, these metrics and the results presented in chapter 5 should be extended to a more comprehensive study, where model bias and sensitivity are compared with observations in a multi-model multi-resolution experiment that may include: coupled and JRA55-do forced simulations from CESM-MOM6, CESM-POP, GFDL-MOM6. Efforts to implement new versions of the MLE parameterization in these models is ongoing.

6.2.4 Atmospheric boundary layers and frontogenesis

Much of the dynamical processes studied in this thesis are translatable to the atmosphere under a certain parameter range (e.g. Hoskins and Bretherton, 1972; Vallis, 2017; Fox-Kemper et al., 2020).

Thus, it is expected to ask whether the conclusions found in this thesis can be relevant for atmospheric fronts and atmospheric boundary layer turbulence. It is argued in chapter 3 that there is a larger physical range that separates boundary layer turbulence from atmospheric mesoscales (which correspond to oceanic submesoscales), especially since much of the atmospheric flow can be approximated using quasi-geostrophic theory. However, these may become more significant during strong storms, or when air flows is governed by boundary conditions such as topography or anomalously warm or cold waters (e.g. Schneider et al., 2003). If such interactions do arise, the effects of humidity should be incorporated in the current framework, as well as understanding whether these interactions are significant, quantifiable, and if they are resolved in climate models due to their larger scale.

Appendix A

Code and Data

Samples of the code and data used to generate results presented in this thesis can be found in the Brown Digital Repository, under the following link: https://doi.org/10.26300/sf8w-0045

Appendix B

First Order Solution Numerical Scheme

B.1 Parameters

- Dimensionless time (t) range is $[0, 19.8]$ where the zeroth order vanishes according to ST13.
- Dimensionless cross-frontal (x) range is $[-2.5, 2.5]$.
- Dimensionless vertical (z) range is $[0, 1]$.
- $\gamma = 0.1$.
- Rossby number $Ro = 0.4$.
- The Froude number is calculated by $Fr = \frac{Ro}{Bu}$ where $Bu = 0.1$ following ST13.

B.2 First Order Solution

- The zeroth order solution is calculated with equations (2.22) and (2.23a)-(2.23c), which serve as inputs for the consecutive steps.
- The PV is calculated by integrating the PV evolution equation (2.33) using Forward Euler method for the first three time steps after which the 3rd order Adam-Bashforth explicit method is used. The zeroth order solution is used to calculate the advection and and flux terms at every time step.
- In the SQG simulation the PV is taken to be zero.
- The five point stencil method is used to invert, at every time step, the second order partial differential equation for ϕ^1 (2.29), using inputs from the zeroth order solution and the PV.

- A similar method is used for ψ (2.25), using inputs from the zeroth order solution and ϕ^1.

B.3 Boundary conditions

For the simulations presented in this paper we do not include fluxes induced by wind shear and thermodynamic forcing.

The boundary conditions for ψ^1 are given by the integrating the cross-front momentum equation (2.5a). We use Forward Euler method for the first three time steps after which the 3rd order Adam-Bashforth explicit method is used. The streamfunction is evaluated at every time step by (2.4). The zeroth order solution is used as input for the zeroth order advection and the total flux terms. The first order advection terms are evaluated at every time step with the explicit method.

The boundary conditions for ϕ^1 is given by the integrating the thermodynamic equation (2.5d) by the same method as for ψ^1, where the geostrophic potential is evaluated at every time step by (2.6).

In the IQG simulation the boundary conditions for ϕ^1 are taken to be trivial $\frac{\partial \phi^1}{\partial z} = 0$. In both the IQG and SQG systems we maintain the boundary conditions for ψ^1 since this is the equation for the ageostrophic streamfunction and is independent at each time of the quasi-geostrophic PV inversion. At past times, the Lagrangian history of the boundary conditions does affect ψ_1, ϕ_1, but these historical effects do not directly accumulate in the first-order ageostrophic overturning circulation, which in the perturbation asymptotics, is diagnostically calculated from the zeroth-order fields through (2.25). The nature of this decomposition is highlighted by the characteristics of the boundary conditions in the SQG system, and equation (2.29) for the IQG system, independent of the first order Lagrangian derivative. The turbulent flux forcing term $\mathcal{F}(\phi^0)$ in equation (2.25) is divided into surface and interior domains for the SQG and QG case respectively.

In the point source case, the boundary conditions are calculated by (2.39) where x_{ft}, x_{fb} are the points of maximum along-front velocity on the boundary.

Appendix C

Analytic Solution for the Delta Function Approximation

To obtain an analytic framework, we chose the locations for which the zeroth order solution goes singular,as the points of maximum frontogenesis. In this approximation, the point sources of PV $(\hat{q}_{fs}, \hat{q}_{fb})$ can be found by evaluating the PV from equation (2.33) at these locations.

With the assumption of point sources of PV, ϕ^1 can be found using the Green's function for the PDE (2.29), then equation (2.25) determines the first order geostrophic streamfunction ψ^1.

If the PDE is elliptic then we can perform a change of variables so that it becomes $\sim \nabla^2$ in some other coordinate system. We are looking for a change of variables $(\xi(x,z),\ \eta(x,z))$ such that $J \equiv \xi_x \eta_z - \xi_z \eta_x \neq 0$ for any $x,\ z$ in the domain. For an equation of the sort:

$$\mathcal{L}[\phi^1] = A\phi^1_{xx} + 2B\phi^1_{xz} + C\phi^1_{zz} = D \tag{C.1}$$

Where:

$$\begin{cases} A = Ro^2 \frac{\partial^2 \phi^0}{\partial z^2} \\ B = -Ro^2 \frac{\partial^2 \phi^0}{\partial x \partial z} \\ C = \left(1 + Ro^2 \frac{\partial^2 \phi^0}{\partial x^2}\right) \\ D = \hat{q}_{ft}\delta(x - x_{ft})\delta(z - z_{ft}) + \hat{q}_{fb}\delta(x - x_{fb})\delta(z - z_{fb}) \end{cases}$$

Assuming A, B, C are real analytic functions in the domain, and that $A(x,y) \neq 0$ (i.e. $\frac{\partial b^0}{\partial z} \neq 0$), a transformation $\Pi(\xi,\eta) = \phi^1(x(\xi,\eta), y(\xi,\eta))$ can be found such that:

$$\mathcal{A}\Pi_{\xi\xi} + 2\mathcal{B}\Pi_{\xi\eta} + \mathcal{C}\Pi_{\eta\eta} = \mathcal{D} \tag{C.2}$$

And:

$$\begin{cases} \mathcal{A} = A\xi_x^2 + 2B\xi_x\xi_z + C\xi_z^2 \\ \mathcal{B} = A\xi_x\eta_x + B(\xi_x\eta_z + \xi_z\eta_x) + C\xi_z\eta_z \\ \mathcal{C} = A\eta_x^2 + 2B\eta_x\eta_z + C\eta_z^2 \end{cases}$$

Since our operator is elliptic we are looking for $\xi,\ \eta$ that satisfy $\mathcal{A} = \mathcal{C}$ and $\mathcal{B} = 0$:

$$A\xi_x^2 + 2B\xi_x\xi_z + C\xi_z^2 = A\eta_x^2 + 2B\eta_x\eta_z + C\eta_z^2 \tag{C.3a}$$

$$A\xi_x\eta_x + B(\xi_x\eta_z + \xi_z\eta_x) + C\xi_z\eta_z = 0 \tag{C.3b}$$

Which can be found by defining the variable $\lambda = \xi + i\eta$, reducing to one equation:

$$A\lambda_x + \left(B \pm i\sqrt{AC - B^2}\right)\lambda_z = 0 \tag{C.4}$$

λ is constant on the characteristics (defined on the complex plane):

$$\frac{dz}{dx} = \frac{B \pm i\sqrt{AC - B^2}}{A} \tag{C.5}$$

Inserting the non-dimensional definitions for $A,\ B.\ C$ gives:

$$\frac{dz}{dx} = \frac{-\frac{\partial b^0}{\partial x}}{\frac{\partial b^0}{\partial z}} \pm i\frac{\sqrt{\left(Ro^2\frac{\partial b^0}{\partial z}\right)\cdot\left(1 + Ro^2\frac{\partial v^0}{\partial x}\right) - \left(Ro^2\frac{\partial b^0}{\partial x}\right)^2}}{\left(Ro^2\frac{\partial b^0}{\partial z}\right)} \tag{C.6}$$

Integrating the equation with respect to x:

$$\left[z + \int\left(\frac{\partial b^0}{\partial x}\Big/\frac{\partial b^0}{\partial z}\right)\ dx\right] \pm i\left[\int\frac{\sqrt{\left(Ro^2\frac{\partial b^0}{\partial z}\right)\cdot\left(1 + Ro^2\frac{\partial v^0}{\partial x}\right) - \left(Ro^2\frac{\partial b^0}{\partial x}\right)^2}}{\left(Ro^2\frac{\partial b^0}{\partial z}\right)}\ dx\right] = const \tag{C.7}$$

This is the characteristic solution for which λ is constant and $\xi = Re[\lambda],\ \eta = Im[\lambda]$:

$$\xi = z + \int\left(\frac{\partial b^0}{\partial x}\Big/\frac{\partial b^0}{\partial z}\right)\ dx \tag{C.8a}$$

$$\eta = \pm\int\frac{\sqrt{\left(Ro^2\frac{\partial b^0}{\partial z}\right)\cdot\left(1 + Ro^2\frac{\partial v^0}{\partial x}\right) - \left(Ro^2\frac{\partial b^0}{\partial x}\right)^2}}{\left(Ro^2\frac{\partial b^0}{\partial z}\right)}\ dx \tag{C.8b}$$

The problem now reduces to solving the equation in $\eta,\ \zeta$ coordinate system, which is a Laplacian operator equal to an equivalent delta function:

$$\Pi_{\xi\xi} + \Pi_{\eta\eta} = \frac{\mathcal{D}(\zeta,\eta)}{\mathcal{A}(\zeta,\eta)} \sim \delta(\zeta,\eta) \tag{C.9}$$

Using the definition for $\xi,\ \eta$ we can find the boundary conditions on Π from the boundary conditions of ϕ^1.

Since ϕ^1 is confined to the frontal region, it can be assumed that far from the front as $(x \to \pm\infty)$ the first order velocities vanish:

$$v^1 = \frac{\partial\phi^1}{\partial x} = \frac{\partial\Pi}{\partial\xi}\cdot\frac{\partial\xi}{\partial x} = -\frac{\partial\Pi}{\partial\xi}\cdot\left(\frac{1}{Ro\frac{\partial v^0}{\partial Z}}\right) = -\frac{\partial\Pi}{\partial\xi}\cdot\left(\frac{2}{e^{\gamma T}Ro^2B_0'(X)}\right) \tag{C.10}$$

Where we use the definition of the slope in X coordinates, as in ST13. The initial buoyancy in X coordinates is $B_0(X) = \frac{1}{2}erf(X/\sqrt{2}) \to B_0'(X) = \frac{1}{\sqrt{2\pi}}e^{-X^2/2}$

$$\to \lim_{x\to\pm\infty}\frac{\partial\Pi}{\partial\xi} = \lim_{x\to\pm\infty}\left[v^1\Big/\frac{2\sqrt{2\pi}e^{X^2/2}}{e^{\gamma T}Ro^2}\right] = 0 \tag{C.11}$$

Also it can be shown that $\xi \to \pm\infty$ as $X \to \pm\infty$ and $X \to \pm\infty$ as $x \to \pm\infty$. Thus we now have the boundary conditions:

$$\lim_{\xi \to \pm\infty} \frac{\partial \Pi}{\partial \xi} = 0 \tag{C.12}$$

In a QG system, we use trivial boundary conditions $\frac{\partial b^1}{\partial z} = \frac{\partial^2 \phi^1}{\partial z^2} = 0$.

$$\frac{\partial \phi^1}{\partial z} = \frac{\partial \Pi}{\partial \eta}\frac{\partial \eta}{\partial z} \quad \to \quad \frac{\partial^2 \phi^1}{\partial z^2} = \frac{\partial}{\partial z}\left(\frac{\partial \Pi}{\partial \eta}\frac{\partial \eta}{\partial z}\right) = \frac{\partial^2 \Pi}{\partial \eta^2}\left(\frac{\partial \eta}{\partial z}\right)^2 + \frac{\partial \Pi}{\partial \eta}\frac{\partial^2 \eta}{\partial z^2} \tag{C.13}$$

In order to obey the boundary conditions, the limit $\frac{\partial^2 \Pi}{\partial \eta^2}\left(\frac{\partial \eta}{\partial z}\right)^2 << \frac{\partial \Pi}{\partial \eta}\frac{\partial^2 \eta}{\partial z^2}$ implies that:

$$0 = \left.\frac{\partial^2 \phi^1}{\partial z^2}\right|_{b.c} = \frac{\partial^2 \Pi}{\partial \eta^2}\left(\frac{\partial \eta}{\partial z}\right)^2 + \frac{\partial \Pi}{\partial \eta}\frac{\partial^2 \eta}{\partial z^2} \approx \left.\frac{\partial \Pi}{\partial \eta}\frac{\partial^2 \eta}{\partial z^2}\right|_{b.c} \quad \to \quad \left.\frac{\partial \Pi}{\partial \eta}\right|_{b.c} = 0. \tag{C.14}$$

Thus, it is enough to show that $\left(\frac{\partial \eta}{\partial z}\right)^2 << \frac{\partial^2 \eta}{\partial z^2}$ and $\frac{\partial^2 \Pi}{\partial \eta^2} << \frac{\partial \Pi}{\partial \eta}$, which are given by the scaling argument:

$$[\eta] = \frac{\sqrt{[A][C]-[B]^2}}{[A]} \cdot L = \frac{\sqrt{\frac{L^2}{H^2} Ro^2}}{\frac{1}{f^2}\frac{M^2 L H}{H^2}} \cdot L = Ro^3 \cdot H \tag{C.15}$$

$$\to \quad \left[\left(\frac{\partial \eta}{\partial z}\right)^2 \Big/ \frac{\partial^2 \eta}{\partial z^2}\right] = \frac{\frac{[A][C]-[B]^2}{[A]^2} \cdot \frac{L^2}{H^2}}{\frac{\sqrt{[A][C]-[B^2]}}{[A]} \cdot \frac{L}{H^2}} = \frac{\sqrt{[A][C]-[B]^2}}{[A]} \cdot L \tag{C.16}$$

For the HB72 case $Ro \sim \mathcal{O}(0.4)$ and $H \sim \mathcal{O}(10)$ which means that $Ro^3 \cdot H \sim 10^{-3} \cdot 10^1 = 10^{-2} << 1$. Thus $\left(\frac{\partial \eta}{\partial z}\right)^2 << \frac{\partial^2 \eta}{\partial z^2}$.

Next, we want to show that $\frac{\partial^2 \Pi}{\partial \eta^2} << \frac{\partial \Pi}{\partial \eta}$:

$$\frac{\partial \phi^1}{\partial x} = \begin{cases} \frac{\partial \Pi}{\partial \eta}\frac{\partial \eta}{\partial x} \\ \frac{\partial \Pi}{\partial \xi}\frac{\partial \xi}{\partial x} \end{cases} \quad \to \quad \frac{\partial \Pi}{\partial \eta}\frac{\partial \eta}{\partial x} = \frac{\partial \Pi}{\partial \xi}\frac{\partial \xi}{\partial x} \quad \to \quad \frac{\partial \Pi}{\partial \eta} = \frac{1}{\frac{\partial \eta}{\partial x}}\frac{\partial \Pi}{\partial \xi}\frac{\partial \xi}{\partial x} \tag{C.17}$$

In addition, in the same way we got equation C.13 with η, we can do the same with ξ:

$$0 = \left.\frac{\partial^2 \phi^1}{\partial z^2}\right|_{b.c} = \frac{\partial^2 \Pi}{\partial \xi^2}\left(\frac{\partial \xi}{\partial z}\right)^2 + \frac{\partial \Pi}{\partial \xi}\frac{\partial^2 \xi}{\partial z^2} \quad \to \quad \left.\frac{\partial^2 \Pi}{\partial \xi^2}\right|_{b.c} = -\left.\frac{\partial \Pi}{\partial \xi}\frac{\frac{\partial^2 \xi}{\partial z^2}}{\left(\frac{\partial \xi}{\partial z}\right)^2}\right|_{b.c} \tag{C.18}$$

Remembering that our initial Laplacian equation for Π is equal to zero everywhere except at the point source. Specifically this means that at the boundaries (assuming the point source is not exactly at the boundary):

$$\left.\frac{\partial^2 \Pi}{\partial \eta^2} + \frac{\partial^2 \Pi}{\partial \xi^2}\right|_{b.c} = 0 \quad \to \quad \left.\frac{\partial^2 \Pi}{\partial \eta^2}\right|_{b.c} = -\left.\frac{\partial^2 \Pi}{\partial \xi^2}\right|_{b.c} = \left.\frac{\partial \Pi}{\partial \xi}\frac{\frac{\partial^2 \xi}{\partial z^2}}{\left(\frac{\partial \xi}{\partial z}\right)^2}\right|_{b.c} \tag{C.19}$$

Now comparing $\frac{\partial^2 \Pi}{\partial \eta^2},\ \frac{\partial \Pi}{\partial \eta}$ by using the expressions found for each on the boundaries and the scaling of the problem:

$$\begin{aligned} \left[\frac{\partial^2 \Pi}{\partial \eta^2} \Big/ \frac{\partial \Pi}{\partial \eta}\right] &= \left[\frac{\partial \eta}{\partial x}\frac{\partial^2 \xi}{\partial z^2}\right] \Big/ \left[\frac{\partial \xi}{\partial x}\left(\frac{\partial \xi}{\partial z}\right)^2\right] = \frac{\frac{[\eta]}{L}\frac{[\xi]}{H^2}}{\frac{[\xi]}{L}\frac{[\xi]^2}{H^2}} = \frac{[\eta]}{[\xi]^2} \\ &= \frac{\frac{\sqrt{AC-B^2}}{A}L}{\left(H + \frac{B}{A}L\right)^2} = \frac{1}{4RoH} \sim \frac{1}{1.6H} << 1 \end{aligned} \tag{C.20}$$

Thus also $\frac{\partial^2 \Pi}{\partial \eta^2} << \frac{\partial \Pi}{\partial \eta}$ which means that $\frac{\partial^2 \Pi}{\partial \eta^2}\left(\frac{\partial \eta}{\partial z}\right)^2 << \frac{\partial \Pi}{\partial \eta}\frac{\partial^2 \eta}{\partial z^2}$.
It can be shown that $\eta \to \infty$ as $z \to -\infty$ and we can define $\eta = \eta_0$ for $z = 0$.
Thus we now have the second boundary conditions:

$$\lim_{\eta \to \infty, \eta_0} \frac{\partial \Pi}{\partial \eta} = 0 \tag{C.21}$$

Now we can use Green's functions theory to solve this equation with Neumann boundary conditions on a half plane:

$$\lim_{\xi \to \pm\infty} \frac{\partial \Pi}{\partial \xi} = 0 \tag{C.22a}$$

$$\lim_{\eta \to \infty, \eta_0} \frac{\partial \Pi}{\partial \eta} = 0 \tag{C.22b}$$

A similar argument can be made for the SQG case with the point source being located on the boundary.

We can solve a linear PDE with an operator $\mathcal{L}$ using the following method:

$$\mathcal{L}\{\Pi\} = F(\eta,\ \xi) \sim \hat{q}(t)\ \delta(\eta - p,\ \xi - s) \tag{C.23}$$

We are looking for:

$$\mathcal{L}\{G(\eta, \xi;\ p, s)\} = \delta(\eta - p,\ \xi - s) \tag{C.24}$$

Multiplying by $F(p,\ s)$ and integrating by $p,\ s$:

$$\int \mathcal{L}\{G(\eta, \xi;\ p, s)\}F(p,\ s)\ dp\ ds = \int \delta(\eta - p,\ \xi - s)F(p,\ s)\ dp\ ds = F(\eta,\ \xi) \tag{C.25}$$

Since $\mathcal{L}$ is a linear operator, acting on $(\eta,\ \xi)$ we can take it out of the integral which acts on $(p,\ s)$:

$$\mathcal{L}\{\Pi\} = F(\eta,\ \xi) = \int \mathcal{L}\{G(\eta, \xi;\ p, s)\}F(p,\ s)\ dp\ ds = \mathcal{L}\left[\int G(\eta, \xi;\ p, s)F(p,\ s)\ dp\ ds\right] \tag{C.26}$$

Thus the solution for $\Pi(\eta,\ \xi)$ is given by:

$$\Pi(\eta,\ \xi) = \int G(\eta, \xi;\ p, s)F(p,\ s)\ dp\ ds \tag{C.27}$$

Since $F(\eta,\ \xi) \sim \hat{q}(t)\ \delta(\eta - p,\ \xi - s)$, the Green's function is proportional to the function $\to \Pi \sim G$.

We are looking for a solution matching two point sources on a half plane with homogeneous Neumann boundary conditions. This means we need to use the method of images in order to find the appropriate solution. In order to satisfy the boundary condition $\frac{\partial \Pi}{\partial \eta}\Big|_{\eta=\eta_0}$ =0, we need to add two image point sources of the same magnitude, sign and distance from the boundary as the point sources located at the front.

The Green's function matching Neumann boundary conditions is:

$$G(\xi,\eta;\xi',\eta') = -\frac{1}{4\pi}\frac{1}{\sqrt{(\xi-\xi')^2+(\eta-\eta')^2}} \tag{C.28}$$

In our problem each point source is multiplied by a factor of $\frac{\mathcal{D}(\xi_f,\eta_f,t)}{\mathcal{A}(\xi_f,\eta_f,t)}$, so the total Green's function which is also the solution for Π is:

$$\begin{aligned}\Pi(\xi,\eta) = &-\frac{1}{4\pi}\frac{\hat{q_{ft}}}{\mathcal{A}_{ft}}\frac{1}{\sqrt{(\xi-\xi_{ft})^2+(\eta-\eta_{ft})^2}} - \frac{1}{4\pi}\frac{\hat{q_{ft}}}{\mathcal{A}_{ft}}\frac{1}{\sqrt{(\xi-\xi_{ft})^2+(\eta+\eta_{ft})^2}}\\ &-\frac{1}{4\pi}\frac{\hat{q_{fb}}}{\mathcal{A}_{fb}}\frac{1}{\sqrt{(\xi-\xi_{fb})^2+(\eta-\eta_{fb})^2}} - \frac{1}{4\pi}\frac{\hat{q_{fb}}}{\mathcal{A}_{fb}}\frac{1}{\sqrt{(\xi-\xi_{fb})^2+(\eta+\eta_{fb})^2}}\end{aligned} \tag{C.29}$$

This is the solution for the first order geostrophic potential ϕ^1 in $\xi,\ \eta$ space.

Bibliography

Aluie, H., Hecht, M., Vallis, G.K., 2018. Mapping the energy cascade in the North Atlantic Ocean: The coarse-graining approach. Journal of Physical Oceanography 48, 225–244.

Bachman, S.D., Fox-Kemper, B., Bryan, F.O., 2015. A tracer-based inversion method for diagnosing eddy-induced diffusivity and advection. Ocean Modelling 86, 1–14.

Bachman, S.D., Fox-Kemper, B., Pearson, B., 2017a. A scale-aware subgrid model for quasi-geostrophic turbulence. Journal of Geophysical Research–Oceans 122, 1529–1554.

Bachman, S.D., Fox-Kemper, B., Taylor, J.R., Thomas, L.N., 2017b. Parameterization of frontal symmetric instabilities. i: Theory for resolved fronts. Ocean Modelling 109, 72–95.

Bakas, N.A., Farrell, B.F., 2009. Gravity waves in a horizontal shear flow. part ii: Interaction between gravity waves and potential vorticity perturbations. Journal of Physical Oceanography 39, 497–511.

Barcilon, V., 1998. On the barotropic ocean with bottom friction. Journal of marine research 56, 731–771.

Barkan, R., Molemaker, J.M., Srinivasan, K., McWilliams, J.C., D'Asaro, E.A., 2019. The role of horizontal divergence in submesoscale frontogenesis. Journal of Physical Oceanography .

Batchelor, G.K., 1959. Small-scale variation of convected quantities like temperature in turbulent fluid part 1. general discussion and the case of small conductivity. Journal of Fluid Mechanics 5, 113–133.

Belcher, S.E., Grant, A.L., Hanley, K.E., Fox-Kemper, B., Van Roekel, L., Sullivan, P.P., Large, W.G., Brown, A., Hines, A., Calvert, D., et al., 2012. A global perspective on langmuir turbulence in the ocean surface boundary layer. Geophysical Research Letters 39.

Bender, C.M., Orszag, S.A., 2013. Advanced mathematical methods for scientists and engineers I: Asymptotic methods and perturbation theory. Springer Science & Business Media.

Benthuysen, J., Thomas, L.N., 2012. Friction and diapycnal mixing at a slope: Boundary control of potential vorticity. Journal of Physical Oceanography 42, 1509–1523.

Blumen, W., 1972. Geostrophic adjustment. Reviews of Geophysics 10, 485–528.

Blumen, W., 1978. Uniform potential vorticity flow: Part i. theory of wave interactions and two-dimensional turbulence. Journal of the Atmospheric Sciences 35, 774–783.

Blumen, W., Piper, M., 1999. The frontal width problem. Journal of the atmospheric sciences 56, 3167–3172.

Boccaletti, G., Ferrari, R., Fox-Kemper, B., 2007. Mixed layer instabilities and restratification. Journal of Physical Oceanography 37, 2228–2250.

Bodner, A.S., Fox-Kemper, B., 2020. A breakdown in potential vorticity estimation delineates the submesoscale-to-turbulence boundary in large eddy simulations. Journal of Advances in Modeling Earth Systems 12, e2020MS002049.

Bodner, A.S., Fox-Kemper, B., Van Roekel, L.P., McWilliams, J.C., Sullivan, P.P., 2020. A perturbation approach to understanding the effects of turbulence on frontogenesis. Journal of Fluid Mechanics 883.

Bond, N.A., Fleagle, R.G., 1985. Structure of a cold front over the ocean. Quarterly Journal of the Royal Meteorological Society 111, 739–759.

Boutle, I.A., Belcher, S.E., Plant, R.S., 2015. Friction in mid-latitude cyclones: an ekman-pv mechanism. Atmospheric Science Letters 16, 103–109.

de Boyer Montégut, C., Madec, G., Fischer, A.S., Lazar, A., Iudicone, D., 2004. Mixed layer depth over the global ocean: An examination of profile data and a profile-based climatology. Journal of Geophysical Research: Oceans 109.

Brannigan, L., Marshall, D.P., Naveira-Garabato, A., Nurser, A.G., 2015. The seasonal cycle of submesoscale flows. Ocean Modelling 92, 69–84.

Bretherton, F.P., 1966. Critical layer instability in baroclinic flows. Quarterly Journal of the Royal Meteorological Society 92, 325–334.

Buckingham, C.E., Naveira Garabato, A.C., Thompson, A.F., Brannigan, L., Lazar, A., Marshall, D.P., George Nurser, A., Damerell, G., Heywood, K.J., Belcher, S.E., 2016. Seasonality of submesoscale flows in the ocean surface boundary layer. Geophysical Research Letters 43, 2118–2126.

Buzzicotti, M., Linkmann, M., Aluie, H., Biferale, L., Brasseur, J., Meneveau, C., 2018. Effect of filter type on the statistics of energy transfer between resolved and subfilter scales from a-priori analysis of direct numerical simulations of isotropic turbulence. Journal of Turbulence 19, 167–197.

Callies, J., Ferrari, R., 2013. Interpreting energy and tracer spectra of upper-ocean turbulence in the submesoscale range (1–200 km). Journal of Physical Oceanography 43, 2456–2474.

Callies, J., Ferrari, R., 2018. Baroclinic instability in the presence of convection. Journal of Physical Oceanography 48, 45–60.

Callies, J., Ferrari, R., Klymak, J.M., Gula, J., 2015. Seasonality in submesoscale turbulence. Nature communications 6, 1–8.

Callies, J., Flierl, G., Ferrari, R., Fox-Kemper, B., 2016. The role of mixed-layer instabilities in submesoscale turbulence. Journal of Fluid Mechanics 788, 5–41.

Calvert, D., Nurser, G., Bell, M.J., Fox-Kemper, B., 2020. The impact of a parameterisation of submesoscale mixed layer eddies on mixed layer depths in the nemo ocean model. Ocean Modelling 154, 101678.

Cao, H., Fox-Kemper, B., Jing, Z., 2021. Submesoscale eddies in the upper ocean of the kuroshio extension from high-resolution simulation: Energy budget. Journal of Physical Oceanography 51, 2181–2201.

Capet, X., Campos, E., Paiva, A., 2008a. Submesoscale activity over the argentinian shelf. Geophysical Research Letters 35.

Capet, X., Klein, P., Hua, B.L., Lapeyre, G., Mcwilliams, J.C., 2008b. Surface kinetic energy transfer in surface quasi-geostrophic flows. Journal of Fluid Mechanics 604, 165–174.

Capet, X., McWilliams, J.C., Molemaker, M.J., Shchepetkin, A., 2008c. Mesoscale to submesoscale transition in the California Current System. Part I: Flow structure, eddy flux, and observational tests. Journal of physical oceanography 38, 29–43.

Capet, X., Roullet, G., Klein, P., Maze, G., 2016. Intensification of upper-ocean submesoscale turbulence through charney baroclinic instability. Journal of Physical Oceanography 46, 3365–3384.

Cavaleri, L., Fox-Kemper, B., Hemer, M., 2012. Wind waves in the coupled climate system. Bulletin of the American Meteorological Society 93, 1651–1661.

Charney, J.G., 1971. Geostrophic turbulence. Journal of the Atmospheric Sciences 28, 1087–1095.

Chavanne, C.P., Klein, P., 2010. Can oceanic submesoscale processes be observed with satellite altimetry? Geophysical Research Letters 37.

Chavanne, C.P., Klein, P., 2016. Quasigeostrophic diagnosis of mixed layer dynamics embedded in a mesoscale turbulent field. Journal of Physical Oceanography 46, 275–287.

Chereskin, T.K., Rocha, C.B., Gille, S.T., Menemenlis, D., Passaro, M., 2019. Characterizing the transition from balanced to unbalanced motions in the southern California Current. Journal of Geophysical Research: Oceans 124, 2088–2109.

Clark, R.A., Ferziger, J.H., Reynolds, W.C., 1979. Evaluation of subgrid-scale models using an accurately simulated turbulent flow. Journal of fluid mechanics 91, 1–16.

Cooper, I.M., Thorpe, A.J., Bishop, C.H., 1992. The role of diffusive effects on potential vorticity in fronts. Quarterly Journal of the Royal Meteorological Society 118, 629–647.

Corrsin, S., 1951. On the spectrum of isotropic temperature fluctuations in an isotropic turbulence. Journal of Applied Physics 22, 469–473.

Crowe, M., Taylor, J.R., 2020. The effects of surface wind stress and buoyancy flux on the evolution of a front in a turbulent thermal wind balance. Fluids 5, 87.

Crowe, M.N., Taylor, J.R., 2018. The evolution of a front in turbulent thermal wind balance. part 1. theory. Journal of Fluid Mechanics 850, 179–211.

Dauhajre, D.P., McWilliams, J.C., 2018. Diurnal evolution of submesoscale front and filament circulations. Journal of Physical Oceanography 48, 2343–2361.

Davies, H., Rossa, A., 1998. Pv frontogenesis and upper-tropospheric fronts. Monthly weather review 126, 1528–1539.

Deardorff, J.W., 1980. Stratocumulus-capped mixed layers derived from a three-dimensional model. Boundary-Layer Meteorology 18, 495–527.

Deardorff, J.W., et al., 1970. A numerical study of three-dimensional turbulent channel flow at large reynolds numbers. J. Fluid Mech 41, 453–480.

Dijkstra, H.A., Molemaker, J.M., 1997. Symmetry breaking and overturning oscillations in thermohaline-driven flows. Journal of Fluid Mechanics 331, 169–198.

Dillon, T.M., 1982. Vertical overturns: A comparison of Thorpe and Ozmidov length scales. Journal of Geophysical Research: Oceans 87, 9601–9613.

Dong, J., Fox-Kemper, B., Zhang, H., Dong, C., 2020. The scale of submesoscale baroclinic instability globally. Journal of Physical Oceanography 50, 2649–2667.

Dong, J., Fox-Kemper, B., Zhang, H., Dong, C., 2021. The scale and activity of symmetric instability estimated from a global submesoscale-permitting ocean model. Journal of Physical Oceanography 51, 1655–1670.

Ducros, F., Nicoud, F., Poinsot, T., 1998. Wall-adapting local eddy-viscosity models for simulations in complex geometries. Numerical Methods for Fluid Dynamics VI , 293–299.

D'Asaro, E., Lee, C., Rainville, L., Harcourt, R., Thomas, L.N., 2011. Enhanced turbulence and energy dissipation at ocean fronts. science 332, 318–322.

Eady, E.T., 1949. Long waves and cyclone waves. Tellus 1, 33–52.

Fedorov, K.N., 1986. The physical nature and structure of oceanic fronts .

Ferrari, R., Rudnick, D.L., 2000. Thermohaline variability in the upper ocean. Journal of Geophysical Research: Oceans 105, 16857–16883.

Ferrari, R., Wunsch, C., 2009. Ocean circulation kinetic energy: Reservoirs, sources, and sinks. Annual Review of Fluid Mechanics 41.

Flament, P., Armi, L., Washburn, L., 1985. The evolving structure of an upwelling filament. Journal of Geophysical Research: Oceans 90, 11765–11778.

Fox-Kemper, B., 2018. Notions for the motions of the oceans. New Frontiers in Operational Oceanography , 27–74.

Fox-Kemper, B., Adcroft, A., Böning, C.W., Chassignet, E.P., Curchitser, E., Danabasoglu, G., Eden, C., England, M.H., Gerdes, R., Greatbatch, R.J., et al., 2019. Challenges and prospects in ocean circulation models. Frontiers in Marine Science 6, 65.

Fox-Kemper, B., Danabasoglu, G., Ferrari, R., Griffies, S.M., Hallberg, R.W., Holland, M.M., Maltrud, M.E., Peacock, S., Samuels, B.L., 2011. Parameterization of mixed layer eddies. III: Implementation and impact in global ocean climate simulations. Ocean Modelling 39, 61–78.

Fox-Kemper, B., Ferrari, R., 2009. An eddifying Parsons model. Journal of Physical Oceanography 39, 3216–3227.

Fox-Kemper, B., Ferrari, R., Hallberg, R.W., 2008. Parameterization of mixed layer eddies. part i: Theory and diagnosis. Journal of Physical Oceanography 38, 1145–1165.

Fox-Kemper, B., Johnson, L., Qiao, F., 2020. Ocean Mixing. Elsevier. chapter Ocean Near-Surface Layers. URL: http://www.geo.brown.edu/research/Fox-Kemper/pubs/pdfs/Fox-KemperJohnson21.pdf. submitted.

Fox-Kemper, B., Menemenlis, D., 2008. Can large eddy simulation techniques improve mesoscale-rich ocean models?, in: Hecht, M., Hasumi, H. (Eds.), Ocean Modeling in an Eddying Regime. AGU Geophysical Monograph Series. volume 177, pp. 319–338.

Fox-Kemper, B., Bachman, S., Pearson, B., Reckinger, S., 2014. Principles and advances in subgrid modeling for eddy-rich simulations. CLIVAR Exchanges 19, 42–46.

Frisch, U., 1995. Turbulence: the legacy of A.N. Kolmogorov. Cambridge University Press, Cambridge,.

Garrett, C., Loder, J., 1981. Dynamical aspects of shallow sea fronts. Phil. Trans. R. Soc. Lond. A 302, 563–581.

Gent, P.R., Mcwilliams, J.C., 1990. Isopycnal mixing in ocean circulation models. Journal of Physical Oceanography 20, 150–155.

Gent, P.R., McWilliams, J.C., Snyder, C., 1994. Scaling analysis of curved fronts. validity of the balance equations and semigeostrophy. Journal of the atmospheric sciences 51, 160–163.

Gildor, H., Fredj, E., Steinbuck, J., Monismith, S., 2009. Evidence for submesoscale barriers to horizontal mixing in the ocean from current measurements and aerial photographs. Journal of Physical Oceanography 39, 1975–1983.

Gill, A.E., 1982. Atmosphere-Ocean dynamics (International Geophysics Series). academic press.

Grant, A.L., Belcher, S.E., 2009. Characteristics of langmuir turbulence in the ocean mixed layer. Journal of Physical Oceanography 39, 1871–1887.

Griffies, S.M., 1998. The gent–mcwilliams skew flux. Journal of Physical Oceanography 28, 831–841.

Gula, J., Molemaker, M.J., McWilliams, J.C., 2014. Submesoscale cold filaments in the gulf stream. Journal of Physical Oceanography 44, 2617–2643.

Gula, J., Molemaker, M.J., McWilliams, J.C., 2016. Topographic generation of submesoscale centrifugal instability and energy dissipation. Nature communications 7, 12811.

Haine, T.W., Marshall, J., 1998. Gravitational, symmetric, and baroclinic instability of the ocean mixed layer. Journal of physical oceanography 28, 634–658.

Håkansson, M., 2002. A two-dimensional numerical study of effects of vertical diffusion in frontal zones. Quarterly Journal of the Royal Meteorological Society: A journal of the atmospheric sciences, applied meteorology and physical oceanography 128, 2439–2467.

Hall, G., Fox-Kemper, B., 2021. Regional mixed layer depth as a climate diagnostic and emergent constraint. Nature Climate Change Submitted.

Hamlington, P.E., Van Roekel, L.P., Fox-Kemper, B., Julien, K., Chini, G.P., 2014. Langmuir–submesoscale interactions: Descriptive analysis of multiscale frontal spindown simulations. Journal of Physical Oceanography 44, 2249–2272.

Haney, S., Fox-Kemper, B., Julien, K., Webb, A., 2015. Symmetric and geostrophic instabilities in the wave-forced ocean mixed layer. Journal of Physical Oceanography 45, 3033–3056.

Harcourt, R.R., Steffen, E.L., Garwood, R.W., D'Asaro, E.A., 2002. Fully Lagrangian floats in Labrador Sea deep convection: Comparison of numerical and experimental results. Journal of physical oceanography 32, 493–510.

Harnik, N., Heifetz, E., 2007. Relating overreflection and wave geometry to the counterpropagating rossby wave perspective: Toward a deeper mechanistic understanding of shear instability. Journal of the atmospheric sciences 64, 2238–2261.

Haynes, P.H., McIntyre, M.E., 1987. On the evolution of vorticity and potential vorticity in the presence of diabatic heating and frictional or other forces. Journal of the Atmospheric Sciences 44, 828–841.

Herring, J., Kerr, R., Rotunno, R., 1994. Ertel's potential vorticity in unstratified turbulence. Journal of the atmospheric sciences 51, 35–47.

Holte, J., Talley, L., 2009. A new algorithm for finding mixed layer depths with applications to argo data and subantarctic mode water formation. Journal of Atmospheric and Oceanic Technology 26, 1920–1939.

Holte, J., Talley, L.D., Gilson, J., Roemmich, D., 2017. An argo mixed layer climatology and database. Geophysical Research Letters 44, 5618–5626.

Hosegood, P., Gregg, M.C., Alford, M.H., 2006. Sub-mesoscale lateral density structure in the oceanic surface mixed layer. Geophysical research letters 33.

Hoskins, B.J., 1974. The role of potential vorticity in symmetric stability and instability. Quarterly Journal of the Royal Meteorological Society 100, 480–482.

Hoskins, B.J., 1975. The geostrophic momentum approximation and the semi-geostrophic equations. Journal of the Atmospheric Sciences 32, 233–242.

Hoskins, B.J., 1982. The mathematical theory of frontogenesis. Annual review of fluid mechanics 14, 131–151.

Hoskins, B.J., 1991. Towards a pv-θ view of the general circulation. Tellus A: Dynamic Meteorology and Oceanography 43, 27–36.

Hoskins, B.J., Bretherton, F.P., 1972. Atmospheric frontogenesis models: Mathematical formulation and solution. Journal of the Atmospheric Sciences 29, 11–37.

Hoskins, B.J., McIntyre, M.E., Robertson, A.W., 1985. On the use and significance of isentropic potential vorticity maps. Quarterly Journal of the Royal Meteorological Society 111, 877–946.

Hudgins, L., Friehe, C.A., Mayer, M.E., 1993. Wavelet transforms and atmopsheric turbulence. Physical Review Letters 71, 3279.

Johnson, P.L., Meneveau, C., 2018. Predicting viscous-range velocity gradient dynamics in large-eddy simulations of turbulence. Journal of Fluid Mechanics 837, 80–114.

Kersalé, M., Petrenko, A.A., Doglioli, A., Nencioli, F., Bouffard, J., Blain, S., Diaz, F., Labasque, T., Queguiner, B., Dekeyser, I., 2016. Lateral diffusivity coefficients from the dynamics of a sf6 patch in a coastal environment. Journal of Marine Systems 153, 42–54.

Keyser, D., Rotunno, R., 1990. On the formation of potential-vorticity anomalies in upper-level jet-front systems. Monthly weather review 118, 1914–1921.

Klein, P., Isern-Fontanet, J., Lapeyre, G., Roullet, G., Danioux, E., Chapron, B., Le Gentil, S., Sasaki, H., 2009. Diagnosis of vertical velocities in the upper ocean from high resolution sea surface height. Geophysical Research Letters 36.

Klein, P., Lapeyre, G., Roullet, G., Le Gentil, S., Sasaki, H., 2011. Ocean turbulence at meso and submesoscales: connection between surface and interior dynamics. Geophysical & Astrophysical Fluid Dynamics 105, 421–437.

Kolmogorov, A.N., 1941. The local structure of turbulence in incrompressible viscous fluid for very large Reynolds number. Dokl. Akad. Nauk. SSSR 30, 9–13.

Kolmogorov, A.N., 1991. The local structure of turbulence in incompressible viscous fluid for very large reynolds numbers. Proceedings of the Royal Society of London. Series A: Mathematical and Physical Sciences 434, 9–13.

Kraichnan, R.H., 1967. Inertial ranges in two-dimensional turbulence. Physics of Fluids 16, 1417–1423.

Kraus, E., Turner, J., 1967. A one-dimensional model of the seasonal thermocline ii. the general theory and its consequences. Tellus 19, 98–106.

Kunze, E., 2019. A unified model spectrum for anisotropic stratified and isotropic turbulence in the ocean and atmosphere. Journal of Physical Oceanography 49, 385–407.

Kurgansky, M.V., Pisnichenko, I.A., 2000. Modified ertel's potential vorticity as a climate variable. Journal of the atmospheric sciences 57, 822–835.

LaCasce, J.H., Mahadevan, A., 2006. Estimating subsurface horizontal and vertical velocities from sea-surface temperature. Journal of Marine Research 64, 695–721.

LaCasce, J.H., Wang, J., 2015. Estimating subsurface velocities from surface fields with idealized stratification. Journal of Physical Oceanography 45, 2424–2435.

Lapeyre, G., Klein, P., 2006. Dynamics of the upper oceanic layers in terms of surface quasigeostrophy theory. Journal of physical oceanography 36, 165–176.

Lapeyre, G., Klein, P., Hua, B.L., 2006. Oceanic restratification forced by surface frontogenesis. Journal of Physical Oceanography 36, 1577–1590.

Large, W., Yeager, S., 2009. The global climatology of an interannually varying air–sea flux data set. Climate dynamics 33, 341–364.

Large, W.G., McWilliams, J.C., Doney, S.C., 1994. Oceanic vertical mixing: A review and a model with a nonlocal boundary layer parameterization. Reviews of Geophysics 32, 363–403.

Ledwell, J.R., Watson, A.J., Law, C.S., 1993. Evidence for slow mixing across the pycnocline from an open-ocean tracer-release experiment. Nature 364, 701–703.

Leonard, A., 1975. Energy cascade in large-eddy simulations of turbulent fluid flows, in: Advances in geophysics. Elsevier. volume 18, pp. 237–248.

Lévy, M., Franks, P.J., Smith, K.S., 2018. The role of submesoscale currents in structuring marine ecosystems. Nature communications 9, 1–16.

Li, Q., Fox-Kemper, B., 2017. Assessing the effects of Langmuir turbulence on the entrainment buoyancy flux in the ocean surface boundary layer. Journal of Physical Oceanography 47, 2863–2886.

Li, Q., Reichl, B.G., Fox-Kemper, B., Adcroft, A.J., Belcher, S.E., Danabasoglu, G., Grant, A.L., Griffies, S.M., Hallberg, R., Hara, T., et al., 2019. Comparing ocean surface boundary vertical mixing schemes including langmuir turbulence. Journal of Advances in Modeling Earth Systems 11, 3545–3592.

Lucas, A.J., Nash, J.D., Pinkel, R., MacKinnon, J.A., Tandon, A., Mahadevan, A., Omand, M.M., Freilich, M., Sengupta, D., Ravichandran, M., et al., 2016. Adrift upon a salinity-stratified sea: A view of upper-ocean processes in the bay of bengal during the southwest monsoon. Oceanography 29, 134–145.

Luo, H., Bracco, A., Cardona, Y., McWilliams, J.C., 2016. Submesoscale circulation in the northern gulf of mexico: Surface processes and the impact of the freshwater river input. Ocean Modelling 101, 68–82.

Mahadevan, A., 2016. The impact of submesoscale physics on primary productivity of plankton. Annual review of marine science 8, 161–184.

Mahadevan, A., Tandon, A., Ferrari, R., 2010. Rapid changes in mixed layer stratification driven by submesoscale instabilities and winds. Journal of Geophysical Research: Oceans 115.

Marshall, J.C., Nurser, A.G., 1992. Fluid dynamics of oceanic thermocline ventilation. Journal of physical oceanography 22, 583–595.

Matheou, G., Chung, D., Teixeira, J., 2017. Large-eddy simulation of a stratocumulus cloud. Physical Review Fluids 2, 090509.

McWilliams, J.C., 2006. Fundamentals of geophysical fluid dynamics. Cambridge University Press, Cambridge.

McWilliams, J.C., 2016. Submesoscale currents in the ocean, in: Proc. R. Soc. A, The Royal Society. p. 20160117.

McWilliams, J.C., 2017. Submesoscale surface fronts and filaments: secondary circulation, buoyancy flux, and frontogenesis. Journal of Fluid Mechanics 823, 391–432.

McWilliams, J.C., 2021. Oceanic frontogenesis. Annual Review of Marine Science 13, 227–253.

McWilliams, J.C., Gula, J., Molemaker, J.M., Renault, L., Shchepetkin, A.F., 2015. Filament frontogenesis by boundary layer turbulence. Journal of Physical Oceanography 45, 1988–2005.

McWilliams, J.C., Molemaker, J.M., 2011. Baroclinic frontal arrest: a sequel to unstable frontogenesis. Journal of Physical Oceanography 41, 601–619.

McWilliams, J.C., Molemaker, M., Olafsdottir, E., 2009. Linear fluctuation growth during frontogenesis. Journal of Physical Oceanography 39, 3111–3129.

McWilliams, J.C., Sullivan, P.P., Moeng, C.H., 1997. Langmuir turbulence in the ocean. Journal of Fluid Mechanics 334, 1–30.

Mensa, J., Timmermans, M.L., Kozlov, I., Williams, W., Özgökmen, T., 2018. Surface drifter observations from the arctic ocean's beaufort sea: Evidence for submesoscale dynamics. Journal of Geophysical Research: Oceans 123, 2635–2645.

Mensa, J.A., Garraffo, Z., Griffa, A., Özgökmen, T.M., Haza, A., Veneziani, M., 2013. Seasonality of the submesoscale dynamics in the gulf stream region. Ocean Dynamics 63, 923–941.

Mironov, D., Terzhevik, A., Kirillin, G., Jonas, T., Malm, J., Farmer, D., 2002. Radiatively driven convection in ice-covered lakes: Observations, scaling, and a mixed layer model. Journal of Geophysical Research: Oceans 107, 7–1.

Moeng, C.H., 1984. A large-eddy-simulation model for the study of planetary boundary-layer turbulence. Journal of the Atmospheric Sciences 41, 2052–2062.

Molemaker, J.M., McWilliams, J.C., Capet, X., 2010. Balanced and unbalanced routes to dissipation in an equilibrated eady flow. Journal of Fluid Mechanics 654, 35–63.

Morel, Y., Gula, J., Ponte, A., 2019. Potential vorticity diagnostics based on balances between volume integral and boundary conditions. Ocean Modelling 138, 23–35.

Nagai, T., Tandon, A., Rudnick, D.L., 2006. Two-dimensional ageostrophic secondary circulation at ocean fronts due to vertical mixing and large-scale deformation. Journal of Geophysical Research: Oceans 111.

Nakamura, N., 1994. Nonlinear equilibration of two-dimensional eady waves: Simulations with viscous geostrophic momentum equations. Journal of the atmospheric sciences 51, 1023–1035.

Nakamura, N., Held, I.M., 1989. Nonlinear equilibration of two-dimensional eady waves. Journal of the Atmospheric Sciences 46, 3055–3064.

Novelli, G., Guigand, C.M., Cousin, C., Ryan, E.H., Laxague, N.J., Dai, H., Haus, B.K., Özgökmen, T.M., 2017. A biodegradable surface drifter for ocean sampling on a massive scale. Journal of Atmospheric and Oceanic Technology 34, 2509–2532.

Nurser, A., Zhang, J., 2000. Eddy-induced mixed layer shallowing and mixed layer/thermocline exchange. Journal of Geophysical Research: Oceans 105, 21851–21868.

Olita, A., Capet, A., Claret, M., Mahadevan, A., Poulain, P.M., Ribotti, A., Ruiz, S., Tintoré, J., Tovar-Sánchez, A., Pascual, A., 2017. Frontal dynamics boost primary production in the summer stratified mediterranean sea. Ocean Dynamics 67, 767–782.

Orszag, S.A., 1971. On the elimination of aliasing in finite-difference schemes by filtering high-wavenumber components. Journal of the Atmospheric sciences 28, 1074–1074.

Ou, H.W., 1984. Geostrophic adjustment: A mechanism for frontogenesis. Journal of Physical Oceanography 14, 994–1000.

Ozmidov, R., 1965. On the turbulent exchange in a stably stratified ocean. Isvestiya, Atmospheric and Oceanic Physics 1, 861–871. (English Edition).

Parsons, A.T., 1969. A two-layer model of Gulf Stream separation. Journal of Fluid Mechanics 39, 511–528.

Pedlosky, J., 2013. Geophysical fluid dynamics. Springer Science & Business Media.

Pedlosky, J., et al., 1987. Geophysical fluid dynamics. volume 710. Springer.

Pham, H.T., Sarkar, S., 2018. Ageostrophic secondary circulation at a submesoscale front and the formation of gravity currents. Journal of Physical Oceanography 48, 2507–2529.

Pollard, R.T., Regier, L.A., 1992. Vorticity and vertical circulation at an ocean front. Journal of Physical Oceanography 22, 609–625.

Pörtner, H.O., Roberts, D.C., Masson-Delmotte, V., Zhai, P., Tignor, M., Poloczanska, E., Mintenbeck, K., Nicolai, M., Okem, A., Petzold, J., et al., 2019. Ipcc special report on the ocean and cryosphere in a changing climate. IPCC Intergovernmental Panel on Climate Change: Geneva, Switzerland 1.

Price, J.F., 1981. Upper ocean response to a hurricane. Journal of Physical Oceanography 11, 153–175.

Price, J.F., Weller, R.A., Pinkel, R., 1986. Diurnal cycling: Observations and models of the upper ocean response to diurnal heating, cooling, and wind mixing. Journal of Geophysical Research: Oceans 91, 8411–8427.

Reichl, B.G., Hallberg, R., 2018. A simplified energetics based planetary boundary layer (epbl) approach for ocean climate simulations. Ocean Modelling 132, 112–129.

Reichl, B.G., Li, Q., 2019. A parameterization with a constrained potential energy conversion rate of vertical mixing due to langmuir turbulence. Journal of Physical Oceanography 49, 2935–2959.

Renault, L., McWilliams, J.C., Gula, J., 2018. Dampening of submesoscale currents by air-sea stress coupling in the californian upwelling system. Scientific reports 8, 13388.

Rhines, P.B., 1979. Geostrophic turbulence. Annual Review of Fluid Mechanics.

Rhines, P.B., 1986. Vorticity dynamics of the oceanic general circulation. Annual review of fluid mechanics 18, 433–497.

Rincon, F., 2006. Anisotropy, inhomogeneity and inertial-range scalings in turbulent convection. Journal of Fluid Mechanics 563, 43–69.

Rocha, C.B., Chereskin, T.K., Gille, S.T., Menemenlis, D., 2016. Mesoscale to submesoscale wavenumber spectra in Drake Passage. Journal of Physical Oceanography 46, 601–620.

Rotunno, R., Skamarock, W.C., Snyder, C., 1994. An analysis of frontogenesis in numerical simulations of baroclinic waves. Journal of the atmospheric sciences 51, 3373–3398.

Rudnick, D.L., Ferrari, R., 1999. Compensation of horizontal temperature and salinity gradients in the ocean mixed layer. Science 283, 526–529.

Salmon, R., 1998. Lectures on geophysical fluid dynamics. Oxford University Press.

Sasaki, H., Klein, P., Qiu, B., Sasai, Y., 2014. Impact of oceanic-scale interactions on the seasonal modulation of ocean dynamics by the atmosphere. Nature communications 5, 1–8.

Schneider, T., Held, I.M., Garner, S.T., 2003. Boundary effects in potential vorticity dynamics. Journal of the atmospheric sciences 60, 1024–1040.

Shakespeare, C.J., Taylor, J., 2014. The spontaneous generation of inertia-gravity waves during frontogenesis forced by large strain: theory. Journal of fluid mechanics 757, 817.

Shakespeare, C.J., Taylor, J.R., 2013. A generalized mathematical model of geostrophic adjustment and frontogenesis: uniform potential vorticity. Journal of Fluid Mechanics 736, 366–413.

Shapiro, M., 1976. The role of turbulent heat flux in the generation of potential vorticity in the vicinity of upper-level jet stream systems. Monthly Weather Review 104, 892–906.

Shapiro, M., 1978. Further evidence of the mesoscale and turbulent structure of upper level jet stream–frontal zone systems. Monthly Weather Review 106, 1100–1111.

Shcherbina, A.Y., Sundermeyer, M.A., Kunze, E., D'Asaro, E., Badin, G., Birch, D., Brunner-Suzuki, A.M.E., Callies, J., Kuebel Cervantes, B.T., Claret, M., et al., 2015. The latmix summer campaign: Submesoscale stirring in the upper ocean. Bulletin of the American Meteorological Society 96, 1257–1279.

Siedler, G., Griffies, S.M., Gould, J., Church, J., 2013. Ocean Circulation and Climate: A 21st Century Perspective. International geophysics series, Academic Press.

Siegelman, L., 2020. Energetic submesoscale dynamics in the ocean interior. Journal of Physical Oceanography In press.

Skyllingstad, E.D., Samelson, R., 2012. Baroclinic frontal instabilities and turbulent mixing in the surface boundary layer. part i: Unforced simulations. Journal of Physical Oceanography 42, 1701–1716.

Smagorinsky, J., 1963. General circulation experiments with the primitive equations: I. the basic experiment. Monthly weather review 91, 99–164.

Smith, K.M., Hamlington, P.E., Fox-Kemper, B., 2016. Effects of submesoscale turbulence on ocean tracers. Journal of Geophysical Research: Oceans 121, 908–933.

Staley, D.O., 1960. Evaluation of potential-vorticity changes near the tropopause and the related vertitcal motions, vertical advection of vorticity, and transfer of radioactive debris from stratosphere to troposphere. Journal of Meteorology 17, 591–620.

Stamper, M.A., Taylor, J.R., Fox-Kemper, B., 2018. The growth and saturation of submesoscale instabilities in the presence of a barotropic jet. Journal of Physical Oceanography .

Stone, P.H., 1966. On non-geostrophic baroclinic stability. Journal of the Atmospheric Sciences 23, 390–400.

Stone, P.H., 1970. On non-geostrophic baroclinic stability: Part ii. Journal of Atmospheric Sciences 27, 721–726.

Sullivan, P.P., McWilliams, J.C., 2010. Dynamics of winds and currents coupled to surface waves. Annual Review of Fluid Mechanics 42.

Sullivan, P.P., McWilliams, J.C., 2018. Frontogenesis and frontal arrest of a dense filament in the oceanic surface boundary layer. Journal of Fluid Mechanics 837, 341–380.

Sullivan, P.P., McWilliams, J.C., 2019. Langmuir turbulence and filament frontogenesis in the oceanic surface boundary layer. Journal of Fluid Mechanics 879, 512–553.

Sullivan, P.P., McWilliams, J.C., Melville, W.K., 2007. Surface gravity wave effects in the oceanic boundary layer: Large-eddy simulation with vortex force and stochastic breakers. Journal of Fluid Mechanics 593, 405–452.

Sullivan, P.P., McWilliams, J.C., Moeng, C.H., 1994. A subgrid-scale model for large-eddy simulation of planetary boundary-layer flows. Boundary-Layer Meteorology 71, 247–276.

Suzuki, N., Fox-Kemper, B., 2016. Understanding Stokes forces in the wave-averaged equations. Journal of Geophysical Research–Oceans 121, 1–18.

Suzuki, N., Fox-Kemper, B., Hamlington, P.E., Van Roekel, L.P., 2016. Surface waves affect frontogenesis. Journal of Geophysical Research 121, 3597–3624. Gulf Oil Spill special section.

Tandon, A., Garrett, C., 1994. Mixed layer restratification due to a horizontal density gradient. Journal of Physical Oceanography 24, 1419–1424.

Taylor, J.R., 2016. Turbulent mixing, restratification, and phytoplankton growth at a submesoscale eddy. Geophysical Research Letters 43, 5784–5792.

Taylor, J.R., Ferrari, R., 2009. On the equilibration of a symmetrically unstable front via a secondary shear instability. Journal of Fluid Mechanics 622, 103–113.

Taylor, J.R., Ferrari, R., 2011. Ocean fronts trigger high latitude phytoplankton blooms. Geophysical Research Letters 38.

Teixeira, M., Belcher, S., 2002. On the distortion of turbulence by a progressive surface wave. Journal of Fluid Mechanics 458, 229–267.

Tennekes, H., Lumley, J.L., 2018. A first course in turbulence. MIT press.

Thomas, L.N., 2005. Destruction of potential vorticity by winds. Journal of physical oceanography 35, 2457–2466.

Thomas, L.N., 2008. Formation of intrathermocline eddies at ocean fronts by wind-driven destruction of potential vorticity. Dynamics of Atmospheres and Oceans 45, 252–273.

Thomas, L.N., 2012. On the effects of frontogenetic strain on symmetric instability and inertia–gravity waves. Journal of Fluid Mechanics 711, 620.

Thomas, L.N., Ferrari, R., 2008. Friction, frontogenesis, and the stratification of the surface mixed layer. Journal of Physical Oceanography 38, 2501–2518.

Thomas, L.N., Lee, C.M., 2005. Intensification of ocean fronts by down-front winds. Journal of Physical Oceanography 35, 1086–1102.

Thomas, L.N., Rhines, P.B., 2002. Nonlinear stratified spin-up. Journal of Fluid Mechanics 473, 211–244.

Thomas, L.N., Tandon, A., Mahadevan, A., 2008. Submesoscale processes and dynamics. Ocean modeling in an Eddying Regime , 17–38.

Thomas, L.N., Taylor, J.R., Ferrari, R., Joyce, T.M., 2013. Symmetric instability in the gulf stream. Deep Sea Research Part II: Topical Studies in Oceanography 91, 96–110.

Thompson, L., 2000. Ekman layers and two-dimensional frontogenesis in the upper ocean. Journal of Geophysical Research: Oceans 105, 6437–6451.

Thorpe, S.A., 1977. Turbulence and mixing in a Scottish loch. Philosophical Transactions of the Royal Society of London. Series A, Mathematical and Physical Sciences 286, 125–181.

Thorpe, S.A., 2005. The turbulent ocean. Cambridge University Press.

Thorpe, S.A., 2007. An introduction to ocean turbulence. volume 10. Cambridge University Press Cambridge.

Tsujino, H., Urakawa, L.S., Griffies, S.M., Danabasoglu, G., Adcroft, A.J., Amaral, A.E., Arsouze, T., Bentsen, M., Bernardello, R., Böning, C.W., et al., 2020. Evaluation of global ocean–sea-ice model simulations based on the experimental protocols of the ocean model intercomparison project phase 2 (omip-2). Geoscientific Model Development 13, 3643–3708.

Twigg, R.D., Bannon, P.R., 1998. Frontal equilibration by frictional processes. Journal of the atmospheric sciences 55, 1084–1087.

Ullman, D.S., Cornillon, P.C., 1999. Satellite-derived sea surface temperature fronts on the continental shelf off the northeast us coast. Journal of Geophysical Research: Oceans 104, 23459–23478.

Vallis, G.K., 2017. Atmospheric and oceanic fluid dynamics. Cambridge University Press.

Van Roekel, L., Adcroft, A.J., Danabasoglu, G., Griffies, S.M., Kauffman, B., Large, W., Levy, M., Reichl, B.G., Ringler, T., Schmidt, M., 2018. The kpp boundary layer scheme for the ocean: Revisiting its formulation and benchmarking one-dimensional simulations relative to les. Journal of Advances in Modeling Earth Systems 10, 2647–2685.

Van Roekel, L.P., Hamlington, P.E., Fox-Kemper, B., 2012. Multiscale simulations of Langmuir cells and submesoscale eddies using XSEDE resources. Extreme Science and Engineering Discovery Environment Conference 2012 (XSEDE12) URL: `http://tinyurl.com/VRHFK12`. accepted.

Vanneste, J., 2013. Balance and spontaneous wave generation in geophysical flows. Annual Review of Fluid Mechanics 45.

Weller, R., Samelson, R., 1991. Upper ocean variability associated with fronts, in: Ocean Variability & Acoustic Propagation. Springer, pp. 463–478.

Wenegrat, J.O., McPhaden, M.J., 2016. Wind, waves, and fronts: Frictional effects in a generalized ekman model. Journal of Physical Oceanography 46, 371–394.

Wenegrat, J.O., Thomas, L.N., Gula, J., McWilliams, J.C., 2018. Effects of the submesoscale on the potential vorticity budget of ocean mode waters. Journal of Physical Oceanography 48, 2141–2165.

Whitt, D.B., Taylor, J.R., 2017. Energetic submesoscales maintain strong mixed layer stratification during an autumn storm. Journal of Physical Oceanography 47, 2419–2427.

Wyngaard, J.C., 2010. Turbulence in the Atmosphere. Cambridge University Press.

Xu, Q., Gu, W., Gao, J., 1998. Baroclinic eady wave and fronts. part i: Viscous semigeostrophy and the impact of boundary condition. Journal of the atmospheric sciences 55, 3598–3615.

Yamaguchi, T., Feingold, G., Kazil, J., 2017. Stratocumulus to cumulus transition by drizzle. Journal of Advances in Modeling Earth Systems 9, 2333–2349.

Young, I., 1994. Global ocean wave statistics obtained from satellite observations. Applied Ocean Research 16, 235–248.

Zhang, Y., Hu, C., Liu, Y., Weisberg, R.H., Kourafalou, V.H., 2019. Submesoscale and mesoscale eddies in the florida straits: Observations from satellite ocean color measurements. Geophysical Research Letters 46, 13262–13270.